FEDERAL UNIVERSITY OF RIO GRANDE DO NORTE
TECHNOLOGY CENTER
GRADUATE PROGRAM IN ELECTRICAL AND COMPUTER ENGINEERING

Comparison of Control Strategies for Squirrel-Cage Induction Generator-Based Wind Energy Conversion Systems

Ismael Alves de Azevedo

Advisor: Prof. Dr. Luciano Sales Barros

Master's Dissertation presented to the Graduate Program in Electrical and Computer Engineering UFRN (area: Automation and Systems) as a requirement for the acquisition of the degree of Master of Science.

PPgEEC Order Number: 632
Natal, RN, July 2021

Universidade Federal do Rio Grande do Norte - UFRN
Sistema de Bibliotecas - SISBI
Catalogação da Publicação na Fonte - Biblioteca Central Zila Mamede

Azevedo, Ismael Alves de.
Comparison of control strategies for squirrel-cage induction generator-based wind energy conversion systems / Ismael Alves de Azevedo - 2021.
119 f.: il.

Dissertação (mestrado) - Universidade Federal do Rio Grande do Norte, Centro de Tecnologia, Programa de Pós-Graduação em Engenharia Elétrica e da Computação, Natal, RN, 2021.
Orientador: Prof. Dr. Luciano Sales Barros.

1. Controle direto de torque - Dissertação. 2. Controle de escorregamento de fluxo - Dissertação. 3. Controle orientado pelo campo - Dissertação. 4. Energia eólica - Dissertação. 5. Gerador de indução em gaiola de esquilo - Dissertação. I. Barros, Luciano Sales. II. Título.

RN/UF/BCZM CDU 621.548

Comparison of Control Strategies for Squirrel-Cage Induction Generator-Based Wind Energy Conversion Systems

Ismael Alves de Azevedo

Master's Dissertation presented at 07/05/2021 to the members of the examining board:

Prof. Dr. Luciano Sales Barros (advisor) ..... DSCO/UFPB

Prof Dr. Daniel Barbosa ..... DEEC/UFBA

Prof. Dr. Andres Ortiz Salazar ..... DCA/UFRN

Abstract

The squirrel cage induction generator will be a robust and low cost alternative to variable speed wind energy conversion systems. For this type of generator, direct torque control, direct stator-field-oriented control, direct rotor-field-oriented control, stator-flux slip control and rotor-flux slip control can be used for maximum power point tracking. Stator-flux slip control and direct torque control have simple schemes with fast dynamic responses, since they do not have internal current controllers. However, stator-flux slip control presents high inrush-current and a poor dynamic response and direct torque control presents high torque ripples and poor performance at low speeds. On the other hand, rotor-flux slip control, direct stator-field-oriented control and direct rotor-field-oriented control have fast dynamic response, low inrush current and low error at maximum power point tracking, but have current controllers and offer a larger complexity in the control design. The objective of this work is to define the most suitable control strategy among direct torque control, direct stator-field-oriented control, direct rotor-field-oriented control, stator-flux slip control and rotor-flux slip control by evaluating the following performance indexes simultaneously: maximum power point tracking, total harmonic distortion, inrush current and dynamic response. Simulations are performed in order to analyze the performance of the control strategies.

In this work, tests were carried out for the five control strategies and the direct rotor-field-oriented control presented the best trade off considering maximum power point tracking, total harmonic distortion and dynamic performance, despite it does not have the best inrush current. Tests of three-phase short circuit and rejection of load were also carried out and the results suggest that the machine-side control is not affected significantly.

Keywords: Direct Torque Control, Field Oriented Control, Flux Slip Control, Squirrel Cage Induction Generator, Wind Energy.

Resumo

O gerador de indução em gaiola de esquilo será uma alternativa robusta e de baixo custo para sistemas de conversão de energia eólica com velocidade variável. Para este tipo de gerador, o controle direto de torque, o controle orientado pelo campo estatórico, o controle orientado pelo campo rotórico, o controle de escorregamento do fluxo estatórico e o controle de escorregamento do fluxo rotórico podem ser utilizados para o rastreamento de ponto de máxima potência. O controle de escorregamento do fluxo estatórico e o controle direto de torque possuem esquemas simples com respostas dinâmicas rápidas, já que não possuem controladores internos de corrente. Entretanto, o controle de escorregamento do fluxo estatórico apresenta alta corrente de partida e baixa qualidade na resposta dinâmica e o controle direto de torque apresenta grande ripple no torque e baixa performance em baixas velocidades. Por outro lado, o controle de escorregamento do fluxo rotórico, o controle orientado pelo campo estatórico e o controle orientado pelo campo rotórico possuem rápida resposta dinâmica, baixa corrente de partida e baixo erro no rastreamento de ponto de máxima potência, mas possuem controladores de corrente e oferecem uma maior complexidade no projeto de controle. O objetivo deste trabalho é definir a estratégia de controle mais adequada entre o controle direto de torque, o controle orientado pelo campo estatórico, o controle orientado pelo campo rotórico, o controle de escorregamento do fluxo estatórico e o controle de escorregamento do fluxo rotórico mediante a avaliação dos seguintes índices de desempenho simultaneamente: rastreamento de ponto de máxima potência, distorção harmônica total, corrente de partida e resposta dinâmica. São realizadas simulações a fim de analisar o desempenho das estratégias de controle.

Neste trabalho, testes foram realizados com as cinco estratégias de controle e o controle orientado pelo campo rotórico apresentou melhor rastreamento de ponto de máxima potência, distorção harmônica total e resposta dinâmica, apesar de não apresentar melhor corrente de partida. Testes de curto-circuito trifásico e rejeição de carga também são realizados e os resultados obtidos sugerem que o controle do lado da máquina não é afetado significativamente.

Palavras-chave: Controle Direto de Torque, Controle de Escorregamento de Fluxo, Controle Orientado pelo Campo, Energia Eólica, Gerador de Indução em Gaiola de Esquilo

Contents

List of Figures

List of Tables

List of Symbols and Abbreviations

C	Capacitance (F)
C_p	Power coefficient of the turbine
$FPOS(\theta_t)$	Function that gives different values according to the angle θ_t
F_m	Damping coefficient of the machine $(\mathrm{N} \cdot \mathrm{m} \cdot \mathrm{s})$
F_t	Damping coefficient of the turbine $(\mathrm{N} \cdot \mathrm{m} \cdot \mathrm{s})$
J_m	Inertia of the machine $(\mathrm{Kg} \cdot \mathrm{m}^2)$
J_t	Inertia of the turbine $(\mathrm{K}g \cdot \mathrm{m}^2)$
K_{torsion}	Constant of torsion
K_s	Loss factor due to the tower shadowing
K_v	Gear constant
L_r	Self inductance of the rotor winding (H)
L_s	Self inductance of the stator winding (H)
M_r	Linkage inductance between two rotor windings (H)
M_s	Linkage inductance between two stator windings (H)
M_{sr}	Linkage inductance between a winding of the stator and a winding of the rotor (H)
P	Number of pairs of poles
P_f	Power provided by VSC 2 (W)
P_g	Active power delivered to the grid (W)
P_s	Power provided by VSC 1 (W)
Q_g	Reactive power delivered to the grid (var)
R	Length of the blade (m)

T_{torsion}	Torsion torque $(\mathrm{N}\cdot\mathrm{m})$
T_e	Electromagnetic torque$(\mathrm{N}\cdot\mathrm{m})$
T_h	Torque of the high velocity side $(\mathrm{N}\cdot\mathrm{m})$
T_l	Torque of the low velocity side $(\mathrm{N}\cdot\mathrm{m})$
T_m	Mechanical torque captured by the blades $(\mathrm{N}\cdot\mathrm{m})$
T_r	Resulting torque $(\mathrm{N}\cdot\mathrm{m})$
T_s	Torque due to the tower shadowing $(\mathrm{N}\cdot\mathrm{m})$
T_t	Total torque of the turbine $(\mathrm{N}\cdot\mathrm{m})$
V_G	Absolute of grid voltage vector (V)
V_{Gq}	Grid voltage vector in q component (V)
V_{cc}	Voltage in the capacitor (V)
α	Angle of tower shadowing $()$
β	Pitch angle $(^{\mathrm{o}})$
δ_a	Angular position of the stator flux vector (rad)
δ_b	Angular position of the rotor flux vector (rad)
δ_i	Angular position of the stator current vector (rad)
λ	Tip-speed ratio
ω_G	Grid angular frequency (rad/s)
ω_a	Frequency of stator flux vector (rad/s)
ω_g	Frequency of a generic referential (rad/s)
ω_h	Frequency of the high velocity side $(\mathrm{rad}/\mathrm{s})$
ω_l	Frequency of the low velocity side $(\mathrm{rad}/\mathrm{s})$
ω_m	Mechanical frequency $(\mathrm{rad}/\mathrm{s})$
ω_r	Rotor speed (rad/s)
ω_t	Turbine speed $(\mathrm{rad}/\mathrm{s})$
$\omega_{ar} = \omega_a - \omega_r$	Slipe frequency of the stator flux vector (rad/s)
ϕ_r	Rotor flux vector (Wb)

ϕ_s Stator flux vector (Wb)

ϕ_{r123} Flux of the rotor winding (Wb)

ϕ_{s123} Flux of the stator winding (Wb)

ρ Air density $(\mathrm{kg/m^3})$

$\sigma = 1 - (l_m^2)/(l_s l_r)$ Dispersion coefficient

θ_G Grid angular position (rad)

θ_r Electric angular position of the rotor (rad)

θ_t Turbine angular position (rad)

i_r Rotor current vector (A)

i_s Current provided by VSC 1 (A)

i_s Stator current vector (A)

$i_{f,dq}$ Current vector in dq (A)

i_{f123} Grid currents (A)

i_{r123} Rotor current (A)

i_{s123} Stator current (A)

l_f Filter inductance (H)

$l_m = (3/2)M_{sr}$ Linkage cyclic inductance (H)

$l_r = L_r - M_r$ Cyclic rotor inductance (H)

$l_s = L_s - M_s$ Cyclic stator inductance (H)

r_f Filter resistance (Ω)

r_h Radius of the high velocity side (m)

r_l Radius of the low velocity side (m)

$r_r = R_r$ Rotor resistance (Ω)

$r_s = R_s$ Stator resistance (Ω)

v_s Stator voltage vector (V)

v_w Wind speed $(\mathrm{m/s})$

v_{G123} Grid voltages (V)

$v_{f,dq}$	Voltage vectors in dq components applied by the converter (V)
v_{f123}	Voltage applied by the converter (V)
v_{r123}	Rotor voltage (V)
v_{s123}	Stator voltage (V)
2L-VSC:	Two-level voltage source converter
CAGR:	Global compound annual growth rate
DFIG:	Double fed induction generator
DRFOC:	Direct rotor-field oriented control
DSFOC:	Direct stator-field oriented control
DTC:	Direct torque control
FL:	Fuzzy-logic
FOC:	Field-oriented control
HCS:	Hill climb searching
IFOC:	Indirect field-oriented control
MPPT:	Maximum power point tracking
NN:	Neural network
PLL:	Phase-locker loop
PMSG:	Permanent magnet synchronous generator
PWM:	Pulse width modulation
RFOC:	Rotor-field oriented control
RFSC:	Rotor-flux slip control
RMS:	Root mean square
SCIG:	Squirrel cage induction generator
SFOC:	Stator-field oriented control
SFSC:	Stator-flux slip control
SVM:	Space vector modulation
SVPWM:	Space Vector pulse width modulation

THD:	Total harmonic distortion
TSR:	Tip-speed ratio
VSC:	Voltage source converter
WECS:	Wind energy conversion systems
WRIG:	Wound rotor induction generator
WRSG:	Wound rotor synchronous generator

Chapter 1

Introduction

Over the last thirty years, renewable energy sources have been attracting great attention due to the cost increase, limited reserves, and adverse environmental impact of fossil fuels. With the goal of clean and renewable energy, besides the push of the first oil price shock of the 1970's, the industry drove the efforts to produce a reliable wind energy conversion systems (WECS). For this reason wind energy is leading the role in achieving low-carbon emission economy and it is a mainstream source of clean energy as described by *GWEC* (2019).

Since the 1980s the technology has become sufficiently efficient and reliable. With this gain of traction, a variety of wind power technologies have been developed, which have improved the conversion efficiency and reduced the costs for wind energy production. The size of wind turbines has increased from a few kilowatts to several megawatts each, so that more energy may be accessed through the blades. In addition to on-land installations, larger wind turbines have been built offshore locations to produce more energy and reduce their ecological impacts such as collisions with birds and bats, alteration of species behavior and transformation of the landscape as presented by Firestone (2019).

It began the century as a niche energy source in Europe and the US, but, nowadays, it became a strong source of clean energy. With this respect, the average revenue per unit of electricity generated that would be required to recover the costs of building and operating a generating plant during its life time has decreased over the decades, assuring cost-competitiveness for this energy around the world.

Besides this, today it has great impact for many involved people: for researchers of future wind power and electrical engineers who need to develop feasible, modern and cost-effective wind energy projects; for professionals who deal with wind energy and really need to understand the complexity of positive and negative effects that it can have on the power system and for wind turbine manufacturers companies.

The global transformation of the energy system towards renewable energy is on its way, and wind power is a major force in this development, having become a major pillar of power supply throughout the world, representing a significant step towards the transition to a energy sustainable future, as well as generation of employments and social-economic development.

During the last decade of the last century, worldwide wind capacity has doubled approximately every three years. Until the start XXI, the cost of electricity from wind power has fallen to about one-sixth since the early 1980s. Almost forty years later, the invest-

ment in wind energy globally totalled USD 142.7 billion in 2019 according to *GWEC* (2019)

In the onshore wind market, there were 54.2 GW new installations, while the offshore wind market passed the milestone of 6 GW, making up of 10% of the global new installation in 2019, a total of 19 per cent growth compared to the year before, bringing total installed capacity to 651 GW as presented by *GWEC* (2019). The global compound annual growth rate (CAGR) is presented in the Figure 1.1 presented by *GWEC* (2019).

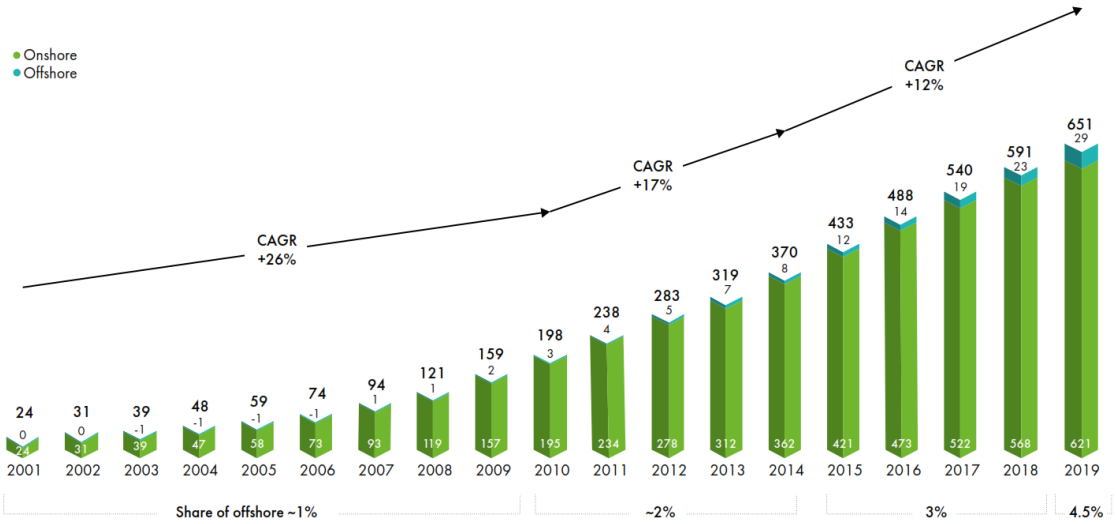

Figure 1.1: Historic development of total installations from *GWEC* (2019).

In term of cumulative installations the greatest markets are: China, the US, Germany, India and Spain, which together accounted for 72 per cent of the world's total wind power installation. As the world's largest wind market, China grid-connected 23.8 GW of onshore wind in 2019, increasing its total onshore installations to 230 GW. Their projects until 2018 are based on feed-in-tariff as described by *GWEC* (2019), which involves long-term agreements and prices tied to the cost of production. The long-term contracts and guaranteed prices shelter producers from some of the risks inherent in renewable energy production, encouraging investment and development that otherwise might not take place. For projects grid-connected after 2020, they will be driven by subsidy-free as described by *Investopedia* (2020).

The US has the second largest global market. In 2019, the 9.1 GW of new onshore installations brought its total onshore to above the 100 GW threshold as presented by *GWEC* (2019). The onshore wind installation project is based on production tax credit, which is a federal incentive that provides financial support for the development of renewable energy facilities. Total installations onshore of 2019 is presented in the Figure 1.2 and total installations offshore of 2019 is presented in the figure 1.3 presented by *GWEC* (2019).

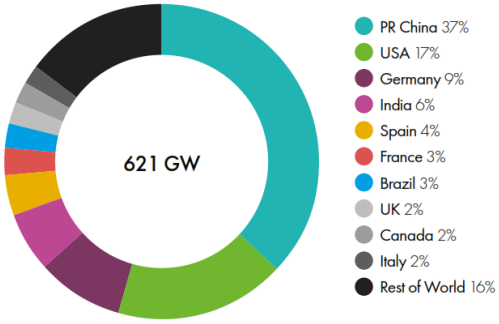

Figure 1.2: Total installations onshore (%) from *GWEC* (2019).

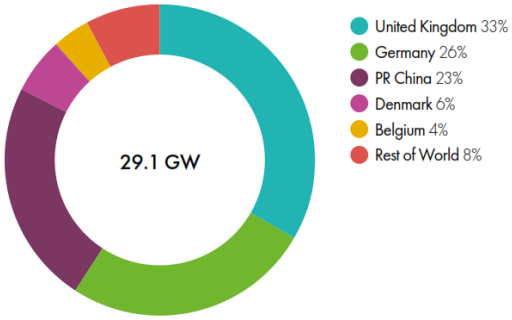

Figure 1.3: Total installations offshore (%) from *GWEC* (2019).

1.1 Wind Energy in Brazil

Brazil has one of the most renewable electric matrix, with one of the greatest hydropower potentials in the world. Today, only around 1/3 of Brazilian hydropower potential is fully exploited as described by *Deloitte* (2020). The greatest undeveloped hydropower generation potential is in northern Brazil, but new projects can face some setbacks due to socio-environmental concerns as presented by *Deloitte* (2020). The actual electric generation power offering in 2019 is presented in the Figure 1.4 as presented by *MME* (2019).

The transmission system is interconnected nationally, except for a small part which represents 0.7 per cent of consumption, which means that regions with low capabilities for wind energy can be benifit from the wind energy producer regions *MME* (2019). Moreover, the Wind Atlas of *MME* (2001) shows that Brazil has 143.5GW of estimated wind potential, from which 75GW is from the northeast, which has the one of the most stable and strong winds during the year.

The year 2019 was an important year for Brazil, since this marked 10 years of the first auction in the country. Brazil's highly efficient and competitive auction model drove wind energy's installed capacity to grow from around 600 MW to 15.4 GW over the last decade. As a result, wind energy is expected to reach 24.2 GW in 2024 as described by *GWEC* (2019).

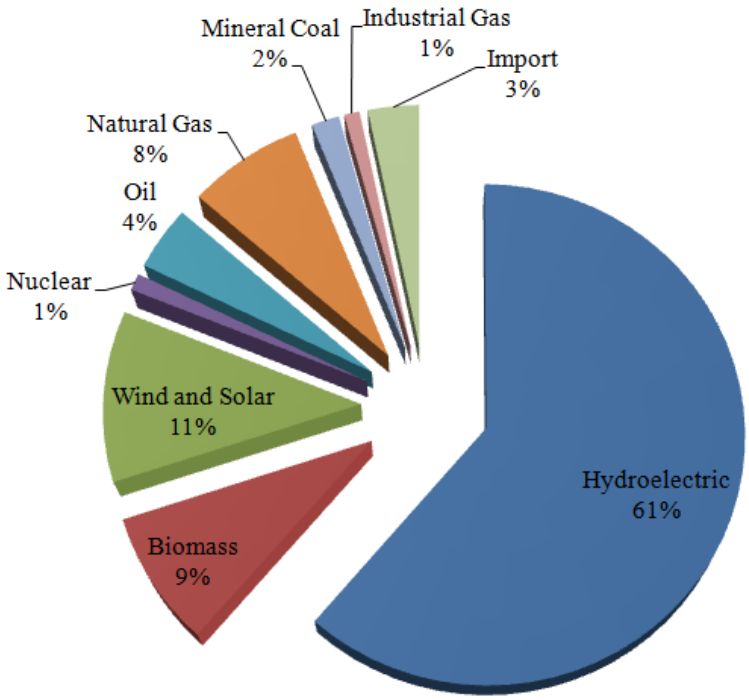

Figure 1.4: Electric Generation Power Offering in 2019 from *GWEC* (2019).

1.2 Motivation

The converison of knetic energy of the wind into electrical energy started with the Type I configuration, which uses a fixed-speed wind turbine with the squirrel cage induction generator (SCIG) directly connected to the grid. However, this scheme employs a capacitor bank for reactive power compensation and a soft-starter for a smoother grid connection, moreover it does not support any speed control and delivers abrupt power changes. The Type II is a limited variable-speed wind turbine with a wound rotor induction generator (WRIG) whose rotor electrical variables can be controlled, but it is more expensive and it is not as robust as the SCIG. This generator uses a variable rotor resistance to control the slip and power output. It also uses a soft-starter and a capacitor bank. The Type III is the double fed induction generator (DFIG) concept, which is a limited variable-speed wind turbine with a WRIG and a partial-scale frequency converter on the rotor circuit providing control of active and reactive power delivered to the grid. This type has the stator circuit directly connected to the grid, requiring additional protection under grid faults. The Type IV uses a full variable-speed wind turbine since the generator is connected to the grid through a full-scale frequency converter. This topology provides control of powers with a smoother connection to the grid, despite the losses in the power conversion as described by Bhutto et al. (2019).

In addition to this, the DFIG and the permanent magnet synchronous generator (PMSG) are the most popular generators of variable speed wind energy conversion system in the market currently. But, although the DFIG can deliver wind energy to the grid in a wide speed range, it requires frequent maintenance that may lead to machine failures and elec-

trical losses as described by Bhutto et al. (2019). The PMSG offers advantages of high efficiency and robust structure. However, the cost of this generator is higher in comparison to other generators due to the expensive permanent magnet materials as described by Bhutto et al. (2019).

A third generator is the squirrel cage induction generator which has poor speed control at slow speeds, high inrush current and poor starting torque, but it has being a low cost alternative to variable speed wind energy conversion systems and it has a simple structure with robustness as described by Merabet B. et al. (2012). It worth mentioning that, in order to expand the speed operation range of the SCIG and the power quality delivered to the grid, a SCIG can be connected to a variable speed WECS and with the grid through a full-scale back-to-back converter as a Type IV configuration as described by Bhutto et al. (2019). Therefore, the SCIG-based WECS with the Type IV configuration is the used configuration in this work.

With the respect of control strategies of this machine, the main control methods are: direct torque control (DTC), stator-field oriented control (SFOC), rotor-field oriented control (RFOC), stator-flux slip control (SFSC) and rotor-flux slip control (RFSC). They can be found in motoring operations, but for generation purpose direct torque control and field oriented control are the most common as described by Begh & Herzog (2018).

DTC and SFSC present the most simple control schemes with no internal current control, SFSC having the easiest control design, but DTC presents high current and torque ripple and SFSC presents high inrush current and a slow dynamic. The three remaining machine-side controls present internal current control, which can perform a better dynamic response and decrease the inrush current, but they have more complex designs as described by Manias (2017). All of these control strategies can be investigated for a better understanding of their capabilities and limitations through analysis of the main performance indexes: maximum power point tracking, total harmonic distortion, inrush current and dynamic response. Then, it will be possible to evaluate the best contol strategy for the application of SCIG-based in type IV configuration, combining the advantages of this generator with the full speed control and the control of powers.

1.3 Objectives

The general objective of the work is to analyse the performance of the main control strategies for squirrel cage induction generator based wind energy conversion systems: DTC, direct SFOC (DSFOC), direct RFOC (DRFOC), SFSC and RFSC. After that, it intents to choose the best control strategy taking into consideration the trade off for the main following performance indexes: maximum power point tracking, total harmonic distortion, inrush current and dynamic response.

Specific objectives:

- Implement and analyse conventional control strategies for SCIG;
- Simulate and evaluate the pros and cons of conventional control strategies for SCIG in WECS;

- Make an analysis of maximum power point tracking (MPPT), total harmonic distortion (THD), inrush current and dynamic response of the control strategies;
- Choose the best control strategy.
- Test the machine-side control under three-phase faults and rejection of load circumstances.

1.4 Organization

This work is organized is this order: chapter 01 presents and contextualizes of wind energy in Brazil and the World, and presents the proposal of the work; the chapter 02 presents the basics principles of WECS; the chapter 03 presents the state of art of control strategies for SCIG; the chapter 04 presents a mathematical description of the turbine, the machine and the control strategies; the chapter 05 presents implementation and results and the chapter 06 presents the conclusion.

Chapter 2

Basic Principles of WECS

This chapter is a review of the basic principles of WECS, involving: the turbine, the generators, the topologies, the power converters and the MPPT control strategies and their applications in SCIG.

2.1 Components of WECS

The main components of WECS are: a wind turbine, which captures the energy of the wind and transforms it into mechanical energy; a gear box, that is connected between the turbine and the rotor of the generator, it operates with the objective of transforming the low speed and high torque input of the turbine into a high speed and low torque necessary for the generator; a generator, that transforms the mechanical movement into electrical energy; power converters, which deliver active and reactive powers to the grid; and a transformer, which is used for a electrical separation of the grid and voltage level set up according to the grid level as described by Tawfiq et al. (2019). The main components of the wind energy is shown below as presented by Rafaat et al. (2018).

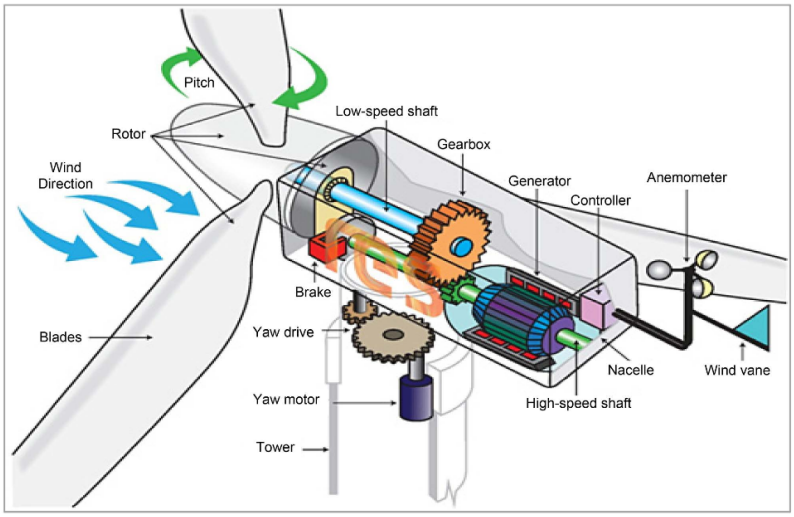

Figure 2.1: Main components of the Wind Energy from Rafaat et al. (2018).

2.1.1 Wind Turbines

There are three main points in the power curve: cut-in wind speed, rated wind speed, and cut-out wind speed. The first is the minimum speed needed in order to start the operation and power delivering, the rated wind speed is the speed at which the system produces nominal power with a controlled operation, and cut-out wind speed is upper limit of the operation of the wind turbine, preventing damage from excessive wind speeds. For higher speed wind the aerodynamic power control of blades: passive stall, active stall or pitch control, is required to keep the power at the rated value as described by Wu et al. (2011). The mechanical power versus wind speed curve is presented in the Figure 2.2 as depicted by Wu et al. (2011).

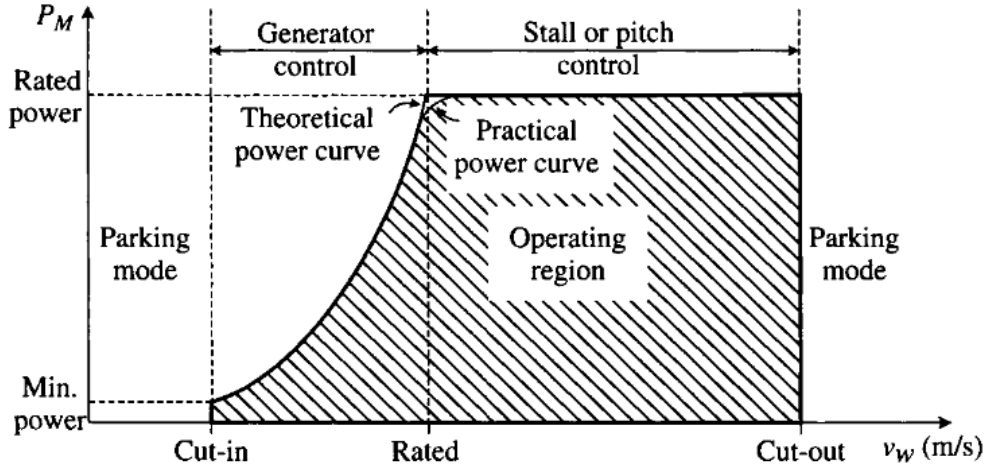

Figure 2.2: Mechanical power versus wind speed curve from Wu et al. (2011).

The wind turbines can be classified according to the turbine generator configuration, airflow path relatively to the turbine rotor, turbine capacity and location of installation. They are also divided in two categories: horizontal-axis and vertical-axis. The first is widely used today in many countries for medium-to-large scale power projects, and most commercial installations around the globe are solely based on these turbines. On the other hand, they are not recognized as a viable option to harness the energy of the wind in urban areas, where the wind is less intense, much more chaotic and turbulent as described by Kumar et al. (2018).

The second type has a vertical-axis of rotation perpendicular to the ground and it can produce electricity from wind of any direction with low cut-in wind speed. These turbines are significantly quieter than the traditional horizontal-axis, lightweight, and can be easily integrated into buildings. These turbines are based on the aerodynamic drag forces, except Darrieus types. The research efforts on these turbines are focused on increasing the aerodynamic efficiency by reducing the drag effect and increasing the lift forces for pumping of water and for low power generation in urban regions as presented by Kumar et al. (2018).

Some designs of drag-based and lift-based vertical-axis wind turbines is presented in the Figure 2.7 as depicted by Liu et al. (2019).

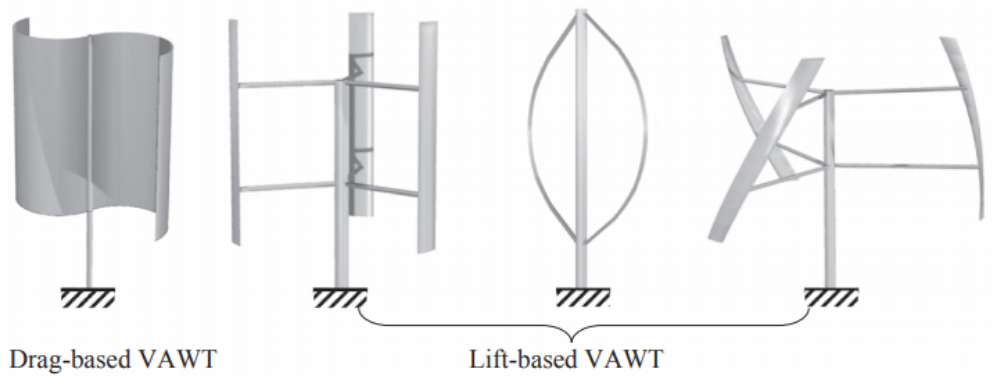

Figure 2.3: Vertical-axis wind turbines from Liu et al. (2019).

Wind turbines can also be classified in upwind, which requires yaw control and the rotor blades have to be positioned far enough away from the turbine tower, and downwind, in which the rotor blades can be designed more flexible and the yaw control system could be eliminated if nacelle is designed appropriately to follow the incoming wind direction passivelyas described by Wang et al. (2018).

Other type of classification is fixed-speed and variable-speed. The first was the standard in 1990s, the wind turbine's rotor speed is fixed and determined by the frequency of the supply grid, the gear ratio and the generator design. It is designed to operates in maximum efficiency at just one particular wind speed and it was usually used with a SCIG, a soft-starter and a capacitor bank for reducing the power compensation. It is simple, robust and reliable, but it is uncontrollable and has significant mechanical stress and limited power quality control, since all wind fluctuations are transmitted to voltage fluctuations. The second type is designed to achieve maximum aerodynamic efficiency over a wide range of wind speeds, varying the rotational speed of the turbine according to the wind, resulting in a maximum power coefficient. This last type increases energy captured, improves power quality and reduces mechanical stress on the wind turbine, but, since it needs power converter controls, this system has losses in power electronics and greater costs as described by Matevosyan et al. (2005).

The number of the blades is fundamental for the project of a wind turbine of horizontal axes and may be defined by the relation of tip-speed ratio (TSR) λ and the power coefficient C_p. This last one increases with the number of the blades, since more blades means more torque, but several aspects have to be considered, such as the purpose of usage, the wind speed of the region and the cost of construction in order to achieve an optimal number. Usually the trade-off gets a number of 3, since it generates more power at a slower rotation speeds and it is more cost-effective than other options as described by Burton et al. (2001). Trade-off of the number of blades is presented in the Table 2.1.

Table 2.1: Trade-off in the number of blades.

N^{o} Blades ↓	N^{o} Blades ↑
Power ↓	Power ↑
Tip-speed ↑	Tip-speed ↓
Weight ↓	Weight ↑
Noise ↑	Noise ↓
Cost ↓	Cost ↑

2.1.2 Generators of WECS

Small stand-alone wind generator systems, with DC shunt-wound machine, were used extensively until the early 1980. It is easy for speed control, especially when the output power could be used in DC form. The need for a machine commutator and brush gear resulted in low reliability and high maintenance costs. Modern brushless DC machines use permanent magnet excitation with an electronic commutation eliminating the need for a machine commutator, resulting in a more reliable machine, but it is still restricted to a few hundred watts at most as described by Shepherd & Zhang (2017).

Most electricity supply systems are of three-phase AC form with fixed frequency and voltage, and use sinusoidal voltages and currents. The multi-megawatt machine used are usually synchronous generators and induction generators. Synchronous generators are much more expensive and mechanically more complicated than an induction generator of a similar size. The magnetic field in the synchronous generator can be created by using permanent magnets, PMSG, or with a conventional field winding, wound rotor synchronous generator (WRSG), and they have often been used in the wind turbines. In the class of induction generators, they have robustness and mechanical simplicity and, as it is produced in large series it also has a low price, but it consumes reactive power to operates, that may be supplied by the grid or by a power electronic system. They are often designed as SCIG or WRIG as presented by Shepherd & Zhang (2017) and Bhutto et al. (2019).

WRSG does not need any reactive power compensation system and it has the stator windings directly connected to the grid and, and therefore, the rotational speed is strictly fixed by the frequency of the supply grid. The rotor winding is excited with DC using slip rings and brushes or with a brushless exciter with a rotating rectifier. The rotor winding, through which DC flows, generates the excitation field, which rotates with synchronous speed. The speed of the synchronous generator is determined by the frequency of the rotating field and by the number of pole pairs of the rotor as described by Bhutto et al. (2019).

The application of PMSGs in wind turbines was because of their property of self-excitation, which allows an operation at a high power factor and a high efficiency, but the materials used for producing permanent magnets are expensive, difficult to work during manufacturing, and they can lose its magnetic qualities at high temperatures, and, therefore, the rotor temperature must be supervised and a cooling system is required. Moreover, there is the requirement of the use of a full-scale power converter in order to adjust the voltage and frequency of generation to the voltage and the frequency of transmission respectively as presented by Bhutto et al. (2019).

The SCIG has mechanical simplicity, high efficiency and low maintenance requirements. Its speed changes by only a few per cent because of the generator slip caused by changes in wind speed. Therefore, this generator was usually used for constant-speed wind turbines. The major problem is that, because of the magnetizing current supplied from the grid to the stator winding, the full load power factor is relatively low and the reactive power supplied by the grid causes additional transmission losses and, in certain situations, can make the grid unstable. But a low power factor is compensated by connecting capacitors in parallel to the generator or by a bidirectional full-load back-to-back power converter. In comparison, the electrical characteristics of the WRIG's rotor can be controlled from the outside, and thereby a rotor voltage can be impressed. The windings of the wound rotor can be externally connected through slip rings and brushes or by means of power electronic equipment. It is more expensive and it is not as robust as the SCIG as described by Bhutto et al. (2019).

2.1.3 Topologies of WECS

There are four main configurations of WECS, among which the the Type I uses a fixed-speed wind turbine with the SCIG directly connected to the grid, which is the cheapest, reliable and robust generator. However, it uses a capacitor bank for reactive power compensation and a soft-starter for a smoother grid connection as presented by Bhutto et al. (2019), moreover it does not present speed control capability and delivers abrupt power changes.

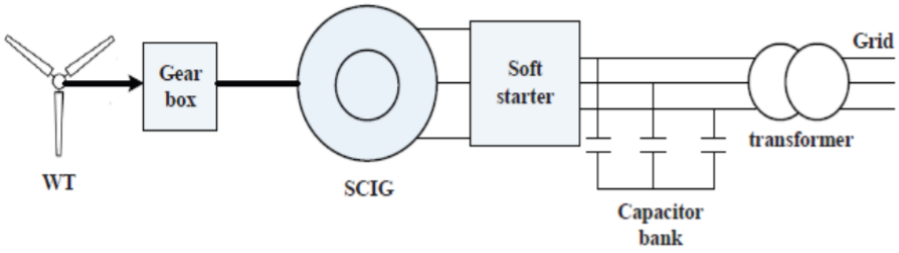

Figure 2.4: Type I topology from Bhutto et al. (2019).

The Type II uses limited variable-speed wind turbine with a WRIG, whose rotor electrical features can be controlled, but it is more expensive and it is not as robust as the SCIG. It uses a variable rotor resistance to control the slip and power output. It also uses a soft-starter and a capacitor bank as described by Bhutto et al. (2019).

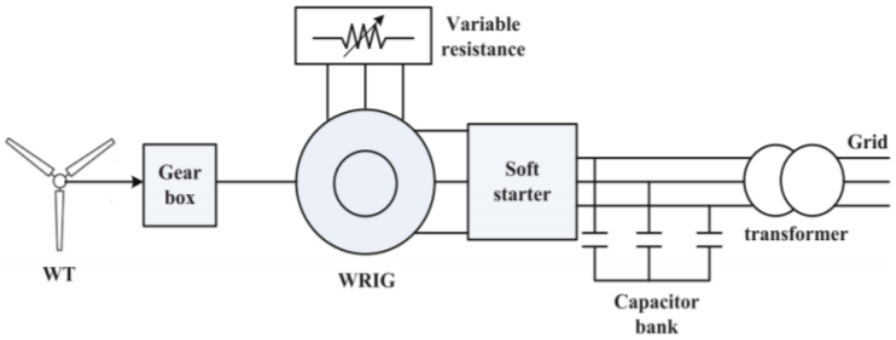

Figure 2.5: Type II topology from Bhutto et al. (2019).

The Type III, known as DFIG concept, uses a limited variable-speed or a variable-speed wind turbine wind turbine with a WRIG and a partial-scale frequency converter on the rotor circuit. It enables control of both active and reactive power delivered by the generator to the grid. It also has a wider range of dynamic speed control, but it needs additional protection in case of grid faults as presented by Bhutto et al. (2019).

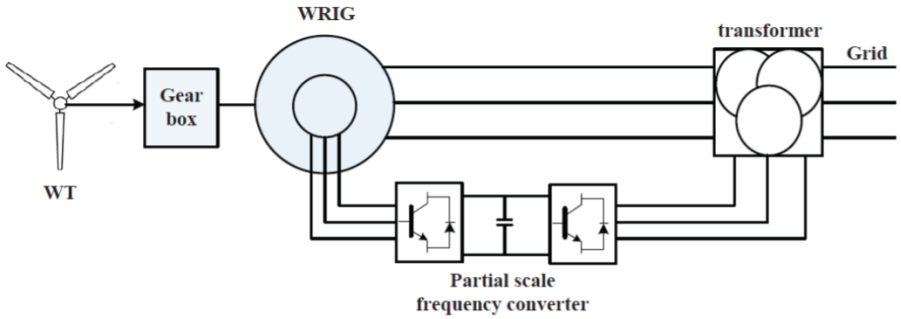

Figure 2.6: Type III topology from Bhutto et al. (2019).

The Type IV uses a full variable-speed wind turbine and the generator is connected to the grid through a full-scale frequency converter. It also enables control of both active and reactive power delivered and it has a smoother connection to the grid, despite the losses in the power conversion as described by Bhutto et al. (2019). This topology is usually used with a PMSG, which has flexibility in speed control and low maintenance as presented by Haque et al. (2008). SCIG used with this topology captures high level of energy, through the the expansion of the speed operation range and has more flexible control as described by Matevosyan et al. (2005).

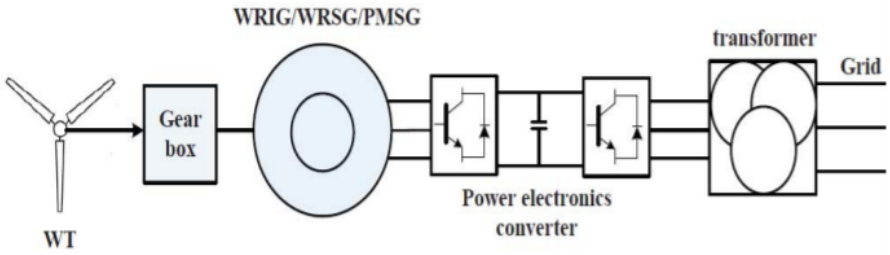

Figure 2.7: Type IV topology from Bhutto et al. (2019).

2.1.4 Power converters of WECS

The two-level voltage source converter (2L-VSC) in back-to-back converter is the most frequently used three-phase power converter topology so far in wind turbines systems. It has a relatively simple structure and few components, which contributes to a well-proven robust and reliable performance, but since it has to deal with great amount of power, at mega-watts and mega-volts power levels, it causes large switching loss and, since many devices may need to be connected in parallel, also the cabling in case of low voltage level can be a great design and physical challenge. Other factors to be considered are that it introduces relatively high ripple stresses to the generator and transformer, and bulky output filters may be needed to limit the voltage gradient and reduce the THD as described by Blaabjerg & Ma (2017).

Despite it is state of the art in DFIG-based wind turbines and several manufacturers are also using this topology for full-rated power converter wind turbines with a squirrel-cage induction generator, it becomes very difficult for a single 2L-VSC topology to achieve acceptable performance for the full-scale wind power converter, even though having the cost advantage as presented by Blaabjerg & Ma (2017).

A multicell solution which have several 2L-VSC converters paralleled both on the generator and grid sides have been introduced. The standard, the proven low voltage converter technologies, redundancy and modular characteristics are the main advantages. This converter configuration is the state of the art solution in the industry for the wind turbines with power level >3 MW as presented by Blaabjerg & Ma (2017). 2L-VSC in back-to-back converter is in the Figure 2.8 as depicted by Blaabjerg & Ma (2017).

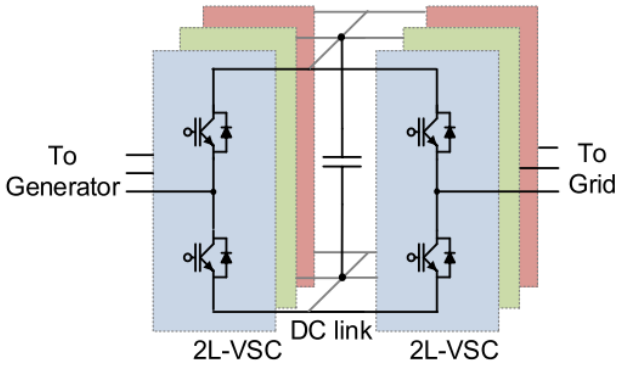

Figure 2.8: 2L-VSC in back-to-back converter for wind turbine from Blaabjerg et al. (2017).

Other topologies like: three-level neutral point diode clamped, three-level H-Bridge, or maybe five-Level H-Bridge, back-to-back topology requires extra cost and loss. Five-Level H-Bridge back-to-back topology introduces more switching devices, which could reduce the reliability of the total system as described by Blaabjerg & Ma (2017).

2.1.5 MPPT control strategies for variable speed WECS

When the wind speed is below the rated speed, the use of a MPPT is indispensable. Through the Figure 2.9 from the author Cheng & Zhu (2014), it is clear that there is a value of TSR, λ, for which the power coefficient, C_p is maximized, thus maximizing the power for a given wind speed. Then the variable speed WECS follows the C_{pmax} to capture the maximum power by varying the rotor speed to keep the system at the optimum TSR: λ_{opt} as demonstrated by Cheng & Zhu (2014).

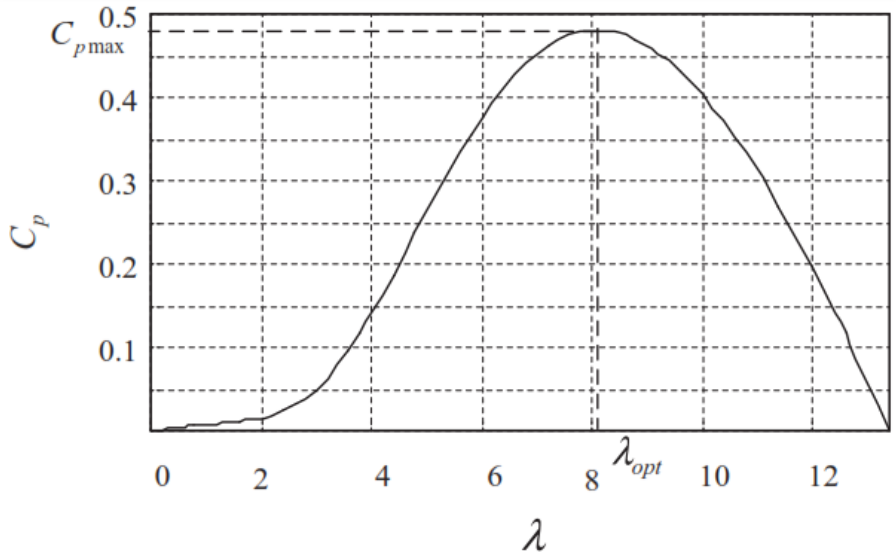

Figure 2.9: Curve of power coefficient versus tip speed ratio λ from Cheng & Zhu (2014).

The mechanical power extracted by a wind turbine can be given by :

$$Power = \frac{1}{2}\rho\pi R^2 C_p(\beta,\lambda)v_w^3. \tag{2.1}$$

Where ρ is the air density, R is the radius of turbine blades, v_w is the wind velocity, and C_p is the power coefficient which is a nonlinear function of the tip speed ratio λ and the blade pitch angle β as described by Dahbi et al. (2014). λ is defined as:

$$\lambda = \frac{\omega_t}{v_w}R. \tag{2.2}$$

To keep the wind turbine at the optimum TSR, the speed of the wind turbine, ω_t, is controlled by regulating the torque of the generator. Hence, various MPPT algorithms have been developed and can be categorized into four types: optimum TSR control, power feedback control, hill climb searching (HCS) control and fuzzy-logic based control as described by Zebraoui & Bouzi (2018).

The optimum TSR control regulates the wind turbine rotor speed to maintain an optimum TSR, as shown in Figure 2.10. This MPPT method requires the measurement of both the wind speed and turbine speed. The wind speed is usually measured by an anemometer which increases the cost of the system and the accurate value is hard to obtain in practice. Besides, the wind turbine characteristic which varies from system to system is also indispensable. Therefore, the optimum TSR MPPT method is rarely applied in the actual WECS though the control strategy is very simple as presented Cheng & Zhu (2014).

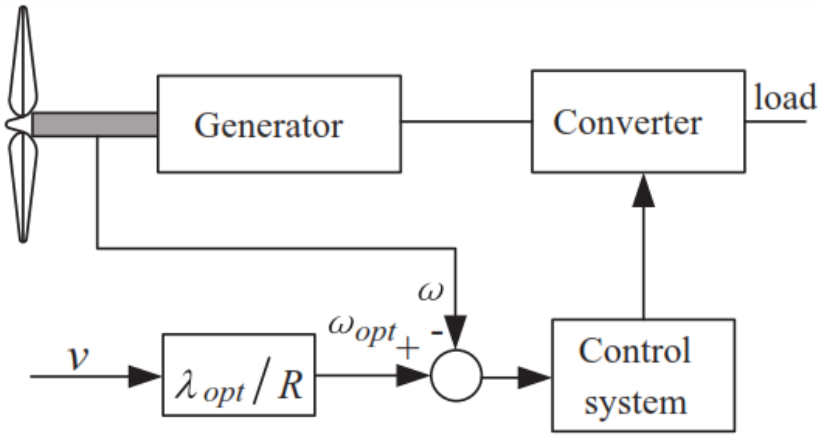

Figure 2.10: Control diagram of optimum TSR MPPT method from Cheng & Zhu (2014).

The power feedback MPPT control is implemented without the need of wind speed, but it requires knowledge of the turbine's maximum power curves, which can be obtained through simulations and practical tests. The wind turbine speed is used to select the stored power curve, which provides the reference power to be tracked by the system. This method can be divided into two categories: the optimum power feedback control and the optimum torque feedback control as shown in Figure 2.11 as depicted by Beltran et al. (2008). Nonetheless the two control methods are essentially the same. The sliding mode

power feedback MPPT method was proposed in Beltran et al. (2008), which can reduce the negative effects of both the uncertainty regarding the wind turbine characteristics and the change in optimal operating point due to wind speed turbulence Cheng & Zhu (2014).

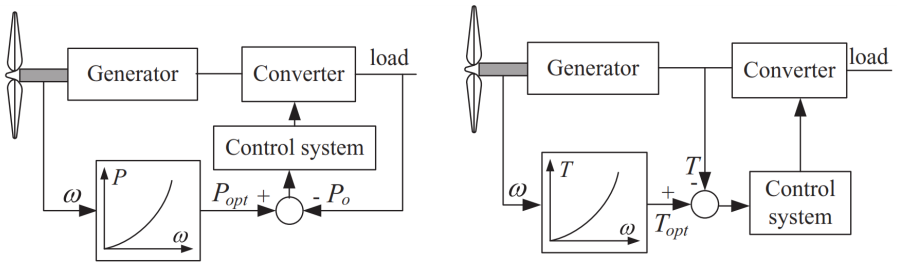

Figure 2.11: Control diagram of optimum power feedback control and the optimum torque feedback control methods from Cheng & Zhu (2014).

The HCS control can be employed by perturbing the control variable and observing the resulting increase or decrease in power, hence also known as perturb and observe method. When the wind turbine speed increases, the output power should normally increase also, as shown in Figure 2.12 as depicted by Cheng & Zhu (2014), otherwise the speed must decrease. This method can be ineffective for large wind turbines, since the large sizes are difficult to adjust the speed quickly and the wrong size perturbation step may lead to deteriorated efficiency of MPPT. Some improved methods have been proposed, such as the recording of the HCS searching results through an on-line training process in an intelligent memory, and then it is used a direct current demand to find the maximum power points rapidly and effectively as presented by Cheng & Zhu (2014) and Wang & Chang (2004).

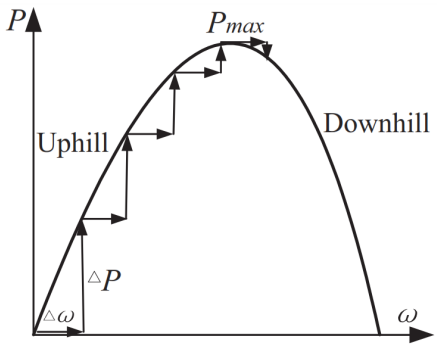

Figure 2.12: Principle of HCS control method from Wang & Chang (2004).

The fuzzy-logic-based MPPT control methods have the advantages of fast convergence, parameter insensitivity and acceptance of noisy and inaccurate signals. The first step fuzzy-logic (FL) which is based on the HCS varies generator speed, observes power output and then tracks the generator speed to extract the maximum power as demonstrated by Simoes et al. (1997). The second FL step programs the machine flux by an on-line search so that to optimize the machine-converter system efficiency. The third FL

step is used to provide robust speed control against turbine oscillatory torque and wind vortex as presented by Cheng & Zhu (2014).

The neural network (NN) based wind velocity estimator was presented by Ro & Choi (2005) to provide fast and accurate velocity information to avoid using anemometers. Besides, the NN based scheme was proposed to compensate the potential drift of wind turbine power coefficient without extra sensors as described by Cheng & Zhu (2014).

The Table 2.2 presents a comparisons of the typical four MPPT methods, where "Need" or "No" correspond to the need or not of the criteria and "Strong", "Medium" and "Weak" correspond to the efficiency of the method for the criteria.

Table 2.2: Comparisons of the typical four MPPT methods.

	Optimum TSR	Power feedback	HCS	FL, NN based
Wind speed	Need	No	No	No
Rotor speed	Need	Need	Need	Need
Wind Turbine characteristcs	Need	Need	No	No
Tracking speed	Strong	Medium	Weak	Weak
Complexity	Strong	Strong	Strong	Weak
Performance under varying wind	Strong	Medium	Weak	Medium

The most commonly used method in practical is the power feedback control due to no need of the wind speed, simple implementation and good dynamic response. The HCS MPPT control methods are studied and verified in small wind turbines, but still not proved to be applied in large-scale wind turbines due to the poor dynamic response under wind turbulence. The optimum TSR MPPT method needs the most system parameters thus it is not used in practice, though the method provides many advantages, including fast tracking speed, implementation simplicity and minor effect of varying wind. The other methods are too complex and still difficult to be realized in practice at this moment as presented by Cheng & Zhu (2014).

2.2 Conclusion

In this Chapter the basics principles of WECS, focusing on the machine-side which is the scope of this work. For the wind energy captured by the blades, the horizontal-axis can offer more power delivered to the grid, being more used for this reason. It is usually used in upwind, with yaw control, and in a variable-speed, since it operates in a wider range of speed wind with more aerodynamic efficiency. In the generator perspective, the SCIG has mechanical simplicity, high efficiency and low maintenance cost. It can be used in a Type IV configuration, delivering the power through a full-scale frequency converter, which enables the control of both active and reactive power to the grid. This converter is usually a 2L-VSC in back-to-back, which has a simple structure and a well-proven performance. The optimum TSR control, despite the difficulty to implement in practice, it has fast tracking speed, implementation simplicity and minor effect of varying wind.

The following chapter deals with the state of art of control strategies for SCIG. It is

discussed their capabilities and limitations for motoring and generating purpose. This last one is important for the MPPT assurance in WECS.

Chapter 3

State of the Art of Control Strategies for SCIG

The most popular control methods for the generator-side converter of SCIG-based WECS is presented in the Figure 3.1 as depicted by Rasul et al. (2017):

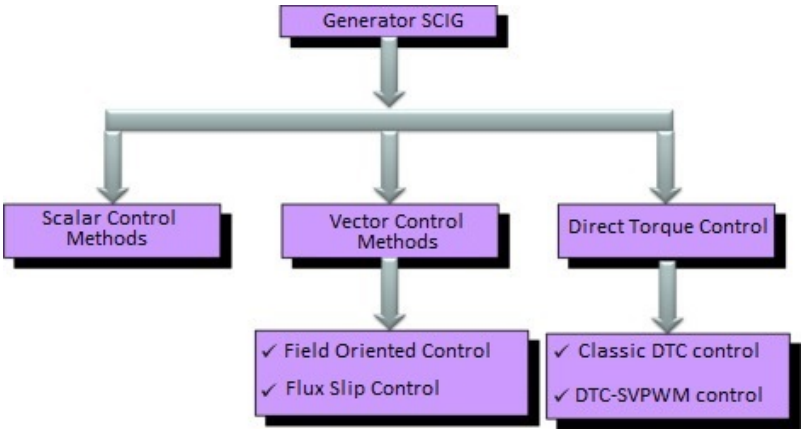

Figure 3.1: Control methods of induction machines from Rasul et al. (2017).

3.1 Scalar Control Strategy

Scalar control is the simplest and most widely used method in most induction machine drive applications. It gives a reasonably good steady-state speed and torque control. The stator flux and torque are not directly controlled and the parameters of the machine must be known as presented by Rasul et al. (2017).

The speed accuracy is low and the dynamic response is slow. In general, in scalar regulation, control by an induction machine can be performed without using information on its current state (the current and voltage of the stator windings, the magnetic flux in the air gap, etc.), which corresponds to lack of feedback in the control system. With control with an open circuit, the machine rotational speed is regulated by changing the frequency of output voltage in such a way that the real shaft rotational speed will be determined by the load torque and output frequency of the converter. The output voltage depends on the frequency according to a relation defined by the chosen system of regulation. The

advantages of this method are simplicity and reliability as described by Kosmodamianskii et al. (2016).

Scalar control can be achieved through the following methods as presented by Manias (2017):

- By varying the root mean square (RMS) value of the stator voltage and keeping the frequency constant. It is a simple control method, but it reduces the capability of the generated electromagnetic torque;
- By varying the frequency of the stator voltage and keeping the RMS value constant. It is a simple control method, but it also reduces the capability of the generated electromagnetic torque;
- By varying the RMS value and frequency of the stator voltage at the same time so that the ratio V_s/f_s to be constant. It is a very simple method that maximizes the electromagnetic torque capability of the induction machine.

The main disadvantages of the scalar control technique with ratio V_s/f_s constant are the following as described by Manias (2017):

- Field orientation is not used;
- Machine status is ignored;
- Torque is not controlled;
- Delaying modulator is used.

3.2 Field Oriented Control

Vector control by field-oriented control (FOC) or DTC are considered as high performance control methods as presented by Rasul et al. (2017). FOC control technique provides decoupling between the torque and magnetic flux of the machine and, consequently, fast torque response can be obtained. FOC is applicable to both induction and synchronous machine drives. Unlike the scalar control the FOC technique, which uses equations and models of the induction machine dynamic state, has the ability to control the amplitude, the frequency, and the position of the space vectors of the voltages, currents, and magnetic flux. Using FOC an ac machine is controlled as a dc separately excited machine. Although the FOC techniques can control separately the torque and the magnetic flux of the induction machine, they are heavily dependent from the parameters and the speed of the machine which results to the reduction of the control robustness. FOC is divided to the following two main types as described by Manias (2017):

- DFOC:
  When DFOC is used the flux vector (amplitude and position) is calculated directly from the measured quantities of the machine;
- Indirect field-oriented control (IFOC):
  When IFOC is used the flux (amplitude and position) is calculated indirectly from existing speed and slip estimations using the field control equations (current model).

The terminology sensorless, which is used in some machine drive systems, signifies that no position/speed feedback devices are used as presented by Manias (2017).

The simulation of IFOC-based WECS was proposed and results show that the proposed control technique is able to maximise the energy extracted from the wind and also demonstrate good transient response characteristics in the decoupled real and reactive powers as demonstrated by Merabet B. et al. (2012).

3.3 Direct Torque Control

In contrast with the scalar control technique, direct torque and flux control (DTC) can control independently the stator magnetic flux and the electromagnetic torque of the induction machine. The basic principle of DTC with space vector modulation (SVM) is the direct selection of a space vector and respective control signals, to control instantaneously the electromagnetic torque, T_e, and stator flux magnitude. The selection of the space vector is made such that to restrict the stator flux and electromagnetic torque errors within the respective flux and torque hysteresis bands, to obtain fast torque response, low inverter switching frequency and low harmonic content. The DTC technique requires only knowledge of the stator resistance and, consequently, reduces the sensitivity associated with the parameters variation and feedback speed is not needed in the DTC, as inputs are considered the desired torque and flux values. The stator magnetic flux is measured by placing Hall sensors in the gap of the machine or by placing inductor sensors in the stator or by using the stator windings as sensors. The DTC, which uses algorithms based on hysteresis control, has the disadvantage of variable switching frequency of the inverter. The DTC presents the following disadvantages as described by Manias (2017):

- Difficulty to control torque and flux at very low speed;
- High current and torque ripple;
- Variable switching frequency;
- High noise level at low speed.

The operation of the conventional DTC is very simple, but it produces high ripple in torque due to hysteresis controllers. Sampling frequency of conventional DTC is not constant and also only one voltage space vector is applied for the entire sampling period. In order to overcome this problem space vector modulation (SVM)-DTC method was proposed by Baader et al. (1992). By using SVM-DTC the sampling frequency is maintained constant and reduced torque ripple with low switching losses as described by Kumar & Rao (2011).

A modulated hysteresis direct torque control applied in an induction generator-based WECS was presented by Abdelli et al. (2013). The results suggested adequate dynamic of the conversion system using the proposed method compared to the classical approaches, with less THD and simplicity.

A space Vector pulse width modulation (SVPWM)-DTC is proposed in a SCIG based WECS with a three levels inverter by Boulouiha et al. (2015). The results suggested that were improved transient responses and reference tracking performance.

A predictive controller for SCIG-based WECS using a DTC was proposed by Lunardi et al. (2016). The simulation results showed the efficiency of the control for active and reactive power tracking and for a low level in the total harmonic distortion for the rotor current, injected by the power converter.

3.4 Flux Slip Control

In scalar strategies, the amplitude and frequency of the magnitude are controlled simultaneously. In the case of vector strategies the control is made through amplitude and phase values or components dq of greatness. Strategies can be classified as according to the chosen flux for the magnetic excitation of the machine and according to the type of variable used in the control of the electromagnetic torque. The magnetic excitation can be done through the stator flux, the rotor flux or interferral flux. The electromagnetic torque can be controlled by the slip frequency of the variable chosen to excite the machine, making what is called the slip control Jacobina & Lima (1996).

The control strategies can be implemented in direct or indirect form. In direct control, there is a closed flux control loop. In indirect control, the flux is controlled without feedback ("feedforward"). The flux feedback signal is obtained directly through of flux sensors or estimated using a closed-loop state observer or still estimated in open loop as described by Jacobina & Lima (1996) and de Rossiter Corrêa et al. (2004).

A closed-loop control strategy was proposed by Abdel-Rahim & Shaltout (2009) and it shows that the proposed scheme is successful in operating the conventional single-phase induction motor as a symmetrical two-phase induction motor with fast dynamic and transient responses.

A hybrid technique which is the combination of adaptive neuro fuzzy inference system and firefly algorithm was applied in slip frequency control of an induction motor as presented by Kulat & Huddar (2018). The dynamic behavior of the induction motors was analyzed in terms of the speed, torque, and slip frequency. The results showed that the proposed method renders better results.

3.5 Conclusion

In this chapter the state of the art is presented for the control of SCIG, which is used for the machine-side control of WECS beeing the scope of this work. The control strategies DTC, FOC and Slip Control are commonly used in induction motor, but DTC and FOC were already used in WECS, but slip control were not used in this application yet. In control perspective, the FOC, DTC and Slip control can be implemented in order to perform the MPPT. This works aims to evaluate the performance of direct torque control, stator-field oriented control, rotor-field oriented control, stator-flux slip control and rotor-flux slip control in order to analyse the pros and cons for a SCIG-based WECS and then choose the best control strategy.

For induction motor speed control, the SFSC is the simplest strategy due to its scheme with decoupled loops for stator flux dq components and that does not require internal cur-

rent controllers, presenting good results with fast dynamics response. Nevertheless, DTC is the most common strategy presenting good results including for the induction machine generating, but it presents a more complex scheme. In turn, FOC is able to control the electromagnetic torque in an equivalent way to that of independent excitation dc machine and with similar performance of DTC, but with an even more complex scheme.

The Table 3.1 presents a summary of state of art of control strategies.

Table 3.1: Summary of state of art of control strategies.

Control	Purpose	Performance indexes	Year
SVM-DTC	Motoring	Dynamic response	1992
DRFOC, DSFOC, SFSC and RFSC	Motoring	Dynamic response	1996
Closed loop FSC	Motoring	Dynamic response	2009
IFOC	WECS	MPPT	2012
Modulated hysteresis DTC	WECS	THD	2013
SVPWM-DTC	WECS	THD	2015
Predictive DTC	WECS	THD, MPPT	2016
Hybrid technic SFC	Motoring	Dynamic response	2018

The following chapter deals with the modeling used in the simulations. It explains the math involved of the aerodynamics, the machine and the control strategies.

Chapter 4

Modeling of WECS

In this Chapter it is presented the modeling used in the simulations being the mechanical model, which includes the wind turbine aerodynamic and the shaft dynamics, the electrical model which refers to the generator, the control strategies and the grid-side control. The models were applied and simulated in MATALAB/Simulink.

4.1 Aerodynamic Model

The turbine captures the energy of wind by the blades and convertes in rotating mechanical energy, as shown in the Figure 4.1 as depicted by Ricardo Cruz (2009). It depends on the power coefficient C_p and the tip speed ratio λ. The power captured is also affected by the tower shadowing and the moments of inertia of the turbine and the generator, which are connected by the shaft causing torsion on it.

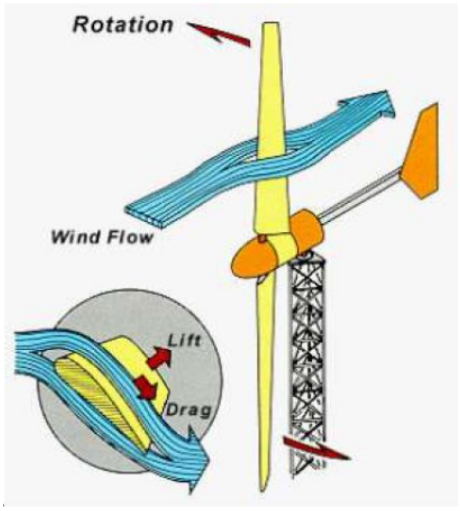

Figure 4.1: The turbine converts the kinetic energy of the wind into rotating mechanical energy from Ricardo Cruz (2009).

The energy of wind is captured by the blades and converted in rotating mechanical energy. However, just a part of this is used in the machine, because it is necessary to

maintain a wind flux through the generator. The model that is used was presented by Siegfried (2014) and Alves (2017). It is based on the power coefficient C_p to represent the kinetic energy captured. The mechanical torque T_m captured by the blade depends on the air density ρ, the length of the blade R, the pitch angle β, the turbine speed ω_t, and the wind speed v_w. It is given by:

$$T_m = \frac{1}{2}\rho\pi R^3 \frac{C_p(\beta,\lambda)}{\lambda} v_w^2; \tag{4.1}$$

and

$$\lambda = \frac{\omega_t}{v_w} R. \tag{4.2}$$

Cp is calculated by these expressions:

$$C_p(\beta,\lambda) = 0,5(\frac{116}{\lambda_i} - 0,4\beta - 5)exp^{\frac{-21}{\lambda_i}}; \tag{4.3}$$

and

$$\frac{1}{\lambda_i} = \frac{1}{\lambda + 0,08\beta} - \frac{0,035}{\beta^3 + 1}. \tag{4.4}$$

The curves of the power coefficient C_p with different tip speed ratio λ according to the pitch angle of the blade β is presented in the Figure 4.2 as depicted by Alves (2017).

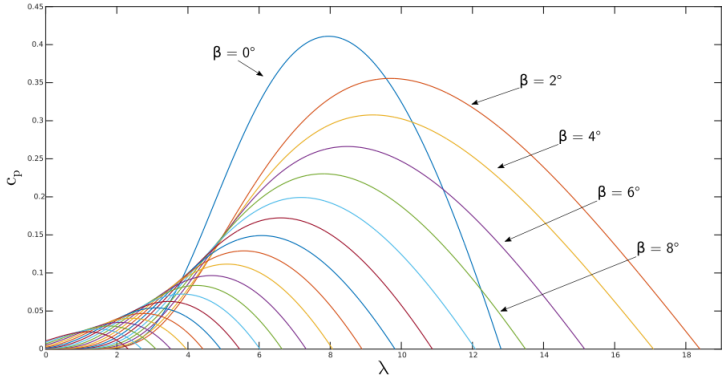

Figure 4.2: Curves C_p x λ from Alves (2017).

4.2 Mechanical Model

The mechanical model used was presented by Siegfried (2014). It is composed of the aerodynamic model and the dynamics of the shaft. The aerodynamic model includes the curves of power coefficient C_p versus the tip speed ratio λ and the tower shadowing. The phenomenon of tower shadowing is considered due to the turbulence caused each time that a blade moves forward to the tower and decreases the system efficiency. A gear box is also considered in this system, because the turbine has a low rotating speed and the generator a high speed.

The coupling of the turbine and the generator is made by the two-mass model presented in the equations (4.9) - (4.11). Tower shadowing (T_s) which is the torque caused by the perturbation of the wind flux every time the blade passes close to the tower is presented in the Figure 4.3 as depicted by Alves (2017) and modeled by:

$$T_s = K_s(0,5cos(FPOS(\theta_t)) - 0,5)T_m; \tag{4.5}$$

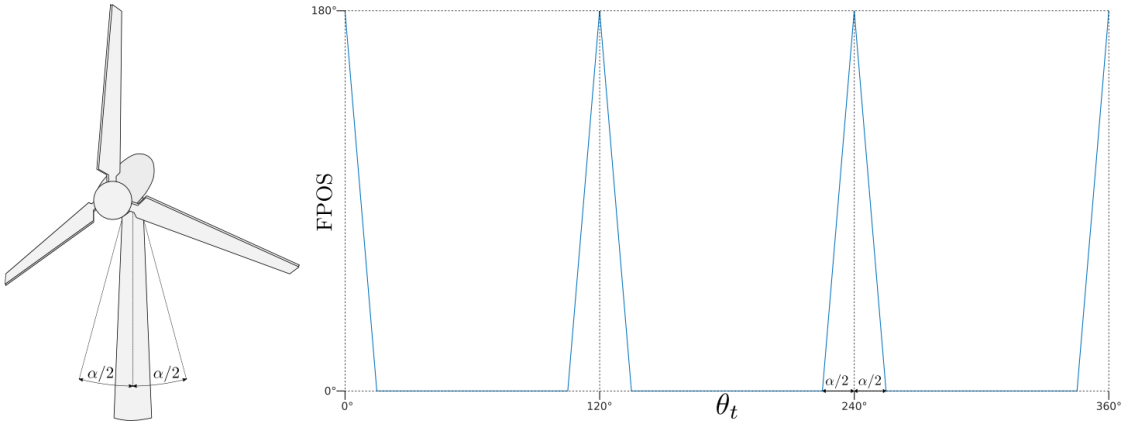

Figure 4.3: FPOS Function from Alves (2017).

Where T_m is the mechanical torque, α is the angle in which the effect occurs, K_s it the loss facto and $FPOS$ is a function that gives different values according to the angle of the turbine θ_t. Thus, the total torque T_t is given by:

$$T_t = T_m + T_s. \tag{4.6}$$

A gear is necessary in this system, because the turbine has a low rotating speed and the generator needs a high speed. The torque of the high velocity side is given by T_h, the torque of the low velocity side is T_l, the frequency of the high velocity side is ω_h, the frequency of the low velocity side ω_l, the radius of the high velocity side is r_h, radius of the low velocity side is r_l and the gear constant is K_v. The model is given by:

$$\frac{T_h}{T_l} = \frac{r_h}{r_l} = \frac{1}{K_v}; \tag{4.7}$$

and:

$$\frac{\omega_h}{\omega_l} = \frac{r_l}{r_h} = K_v. \tag{4.8}$$

The coupling of the turbine and the generator is presented in Figure 4.4 as depicted by Alves (2017) and it is modelled by torsion torque T_{torsion}, electromagnetic torque T_e, resulting torque T_r, constant of torsion K_{torsion}, inertia of the turbine J_t, inertia of the machine J_m, damping coefficient of the turbine F_t, damping coefficient of the machine F_m, mechanical frequency ω_m, mechanical torque captured by the blades T_m and it is give by the following equations:

$$T_t - T_{torsion} = J_t \frac{d\omega_t}{dt} + F_t \omega_t; \tag{4.9}$$

$$T_e + T_{torsion} = J_m \frac{d\omega_m}{dt} + F_m \omega_m; \tag{4.10}$$

$$T_{torsion} = K_{torsion} \int (\omega_t - \omega_m) dt. \tag{4.11}$$

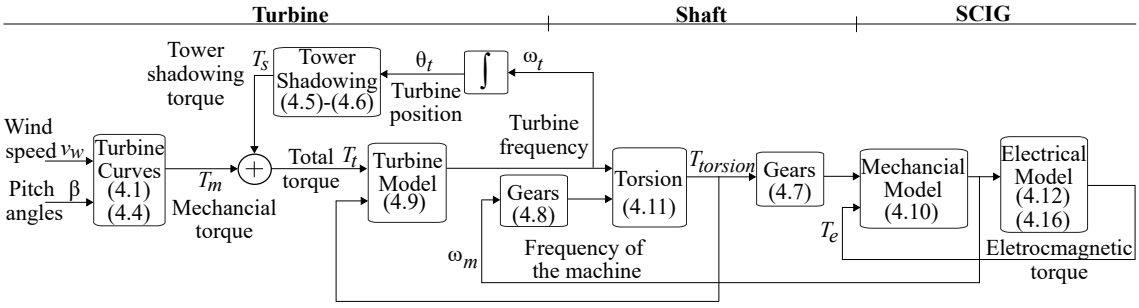

Figure 4.4: Generator and turbine coupling from Alves (2017).

4.3 Electrical Model

The electrical dynamic of the windings of the stator and the rotor is considered in this section. The three phase induction generator can be described by three windings in the stator and three in the rotor. There are some assumptions that are made to simplify the model: the windings are equals and shifted by 120 degrees from each other, the air gap is considered constant, the magnetic circuit is ideal and the flux density distribution in the gap is sinusoidal. The model is presented in the Figure 4.5 as depicted by Alves (2017). The stator fluxes ϕ_{s123}, rotor fluxes ϕ_{r123}, stator voltages v_{s123}, rotor voltages v_{r123}, and the electromagnetic torque T_e are given by:

$$\phi_{s123} = \overline{L}_{ss} i_{s123} + \overline{L}_{sr} i_{r123}; \tag{4.12}$$

$$\phi_{r123} = \overline{L}_{rs} i_{s123} + \overline{L}_{rr} i_{r123}; \tag{4.13}$$

$$v_{s123} = R_s i_{s123} + \frac{d\phi_{s123}}{dt}; \tag{4.14}$$

$$v_{r123} = R_r i_{r123} + \frac{d\phi_{r123}}{dt}; \tag{4.15}$$

$$T_e = P i_{s123}^T \frac{d\overline{L}_{sr}}{d\theta_r} i_{r123}. \tag{4.16}$$

Where:

$$i_{s123} = \begin{bmatrix} i_{s1} \\ i_{s2} \\ i_{s3} \end{bmatrix} \; v_{s123} = \begin{bmatrix} v_{s1} \\ v_{s2} \\ v_{s3} \end{bmatrix} \; \phi_{s123} = \begin{bmatrix} \phi_{s1} \\ \phi_{s2} \\ \phi_{s3} \end{bmatrix}; \tag{4.17}$$

$$i_{r123} = \begin{bmatrix} i_{r1} \\ i_{r2} \\ i_{r3} \end{bmatrix} \; v_{r123} = \begin{bmatrix} v_{r1} \\ v_{r2} \\ v_{r3} \end{bmatrix} \; \phi_{r123} = \begin{bmatrix} \phi_{r1} \\ \phi_{r2} \\ \phi_{r3} \end{bmatrix}; \tag{4.18}$$

$$L_{ss} = \begin{bmatrix} L_s & M_s & M_s \\ M_s & L_s & M_s \\ M_s & M_s & L_s \end{bmatrix} \; L_{rr} = \begin{bmatrix} L_r & M_r & M_r \\ M_r & L_r & M_r \\ M_r & M_r & L_r \end{bmatrix}; \tag{4.19}$$

$$L_{rs}(\theta_r) = M_{sr} \begin{bmatrix} cos(\theta_r) & cos(\theta_r + \frac{2\pi}{3}) & cos(\theta_r + \frac{4\pi}{3}) \\ cos(\theta_r + \frac{4\pi}{3}) & cos(\theta_r) & cos(\theta_r + \frac{2\pi}{3}) \\ cos(\theta_r + \frac{2\pi}{3}) & cos(\theta_r + \frac{4\pi}{3}) & cos(\theta_r) \end{bmatrix}; \tag{4.20}$$

$$L_{rs}(\theta_r) = L_{sr}^t(\theta_r); \tag{4.21}$$

$$\frac{d\overline{L}_{sr}}{d\theta_r} = -M_{sr} \begin{bmatrix} \sin(\theta_r) & \sin(\theta_r + \frac{2\pi}{3}) & \sin(\theta_r + \frac{4\pi}{3}) \\ \sin(\theta_r + \frac{4\pi}{3}) & \sin(\theta_r) & \sin(\theta_r + \frac{2\pi}{3}) \\ \sin(\theta_r + \frac{2\pi}{3}) & \sin(\theta_r + \frac{4\pi}{3}) & \sin(\theta_r) \end{bmatrix}. \tag{4.22}$$

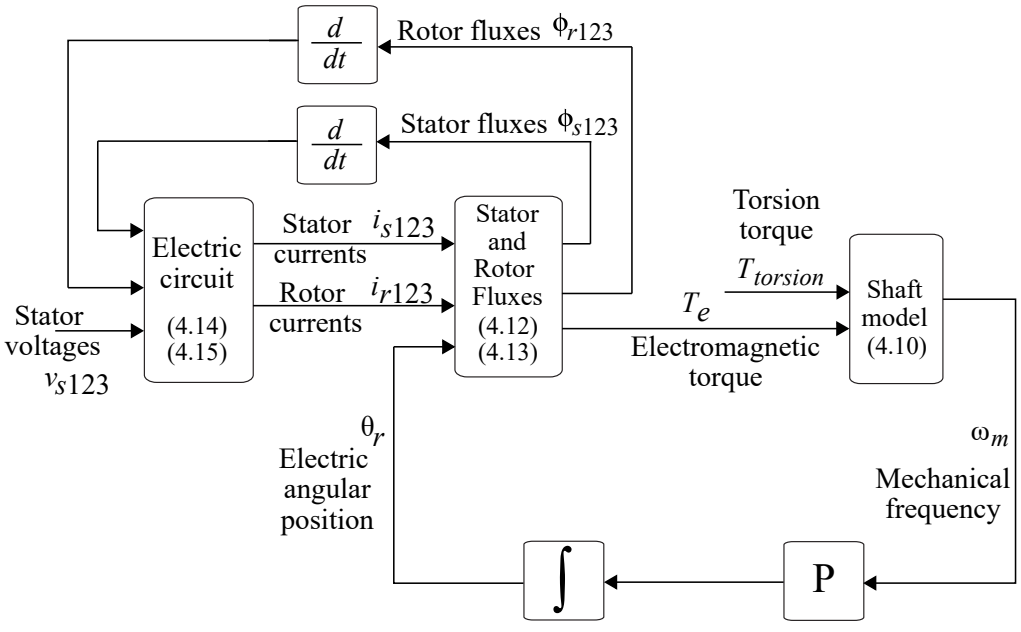

Figure 4.5: Machine model from Alves (2017).

Where i_{s123} is the stator currents, i_{r123} is the rotor currents, L_s is the self inductance of the stator winding, L_r is the self inductance of the rotor winding, M_s is the linkage

inductance between two stator windings, M_r is the linkage inductance between two rotor windings, M_{sr} is the linkage inductance between a winding of the stator and a winding of the rotor, P is the number of pairs of poles, θ_r is the electric angular position of the rotor and θ_t is the turbine angular position.

4.4 Control Systems

The control systems consist of machine side control and grid side control, moreover there exist the converters and their PWM commands. The whole system is shown in the diagram of the Figure 4.6 as depicted by Alves (2017).

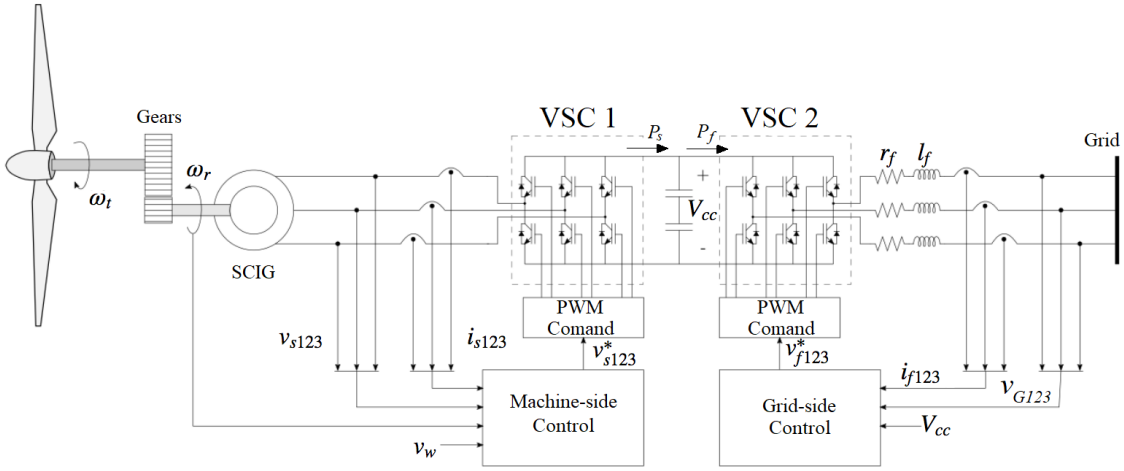

Figure 4.6: The scheme of the wind energy conversion systems used in simulation from Alves (2017).

4.5 Machine Side

The machine-side control is responsible to the MPPT. To do this, it has to control the turbine speed ω_t in response to the wind variations and keep the optimum power coefficient of the turbine. The control of ω_t is carried out through the control of ω_r since these speeds are at the ends of the shaft.

In order to find the control equations, one applies the Park Transform to the equations (4.12)-(4.16) of the machine model results in a simplified version. In $0dq$, in a generic reference g, the equations are:

$$\phi_s^g = l_s i_s^g + l_m i_r^g; \tag{4.23}$$

$$\phi_r^g = l_r i_r^g + l_m i_s^g; \tag{4.24}$$

$$v_s^g = r_s i_s^g + \frac{d\phi_s^g}{dt} + j\omega_g \phi_s^g; \tag{4.25}$$

$$v_r^g = 0 = r_r i_r^g + \frac{d\phi_r^g}{dt} + j(\omega_g - \omega_r)\phi_r^g; \tag{4.26}$$

$$T_e = P i_s^g \phi_s \sin(\delta_i - \delta_a) = \frac{l_m}{l_r} i_s^g \phi_r \sin(\delta_i - \delta_b). \tag{4.27}$$

Where ϕ_s is the stator flux, ϕ_r is the rotor flux, v_s is the stator voltage, v_{r123} is the rotor voltage, $r_s = Rs$ and $r_r = Rr$ are the stator and rotor resistances, ω_g is the frequency of a generic referential, $l_s = Ls - Ms$ and $l_r = Lr - Mr$ are stator and rotor cyclic inductance, $l_m = (3/2)Mrs$ is the linkage cyclic inductance, δ_i is the angular position of the stator current vector, δ_a is the angular position of the stator flux vector, δ_b is the angular position of the rotor flux vector and ω_r is the rotor flux frequency.

These equations and the following subsections deals with common modeling and control strategies used to control the SCIG in motoring operations as demonstrated by Jacobina & Lima (1996), but these are used in this work for the machine-side control of SCIG-based WECS.

4.5.1 Stator-Flux Slip Control (SFSC)

In this control strategy the torque control and flux are performed directly to the stator flux vector. If the stator is used as referential ($\omega_g = 0$) and if ϕ_r^g is considered a disturbance, the equation (4.25) gets simplified. Based on it, it is possible to design a PI controller for the fluxes in dq without current controllers.

Isolating i_s^g from equation (4.23) and i_r^g from equation (4.24):

$$i_s^g = \frac{1}{l_s}\phi_s^g - \frac{l_m}{l_s} i_r^g; \tag{4.28}$$

$$i_r^g = \frac{1}{l_r}\phi_r^g - \frac{l_m}{l_r} i_s^g; \tag{4.29}$$

Applying equation (4.29) in equation (4.28):

$$i_s^g = \frac{1}{l_s}\phi_s^g - \frac{l_m}{l_s}\left(\frac{1}{l_r}\phi_r^g - \frac{l_m}{l_r} i_s^g\right). \tag{4.30}$$

Considering the dispersion coefficient as:

$$\sigma = 1 - \frac{l_m^2}{l_s l_r}. \tag{4.31}$$

The equation equation (4.30) results in:

$$i_s^g = \frac{1}{l_s \sigma}\phi_s^g - \frac{l_m}{\sigma l_s l_r}\phi_r^g. \tag{4.32}$$

Applying equation (4.32) in equation (4.25):

$$v_s^g = r_s\left(\frac{1}{l_s\sigma}\phi_s^g - \frac{l_m}{\sigma l_s l_r}\phi_r^g\right) + \frac{d\phi_s^g}{dt} + j\omega_g\phi_s^g. \tag{4.33}$$

In dq and with the stator referential s:

$$v_{sd}^s = \frac{r_s}{\sigma l_s}\phi_{sd}^s + \frac{d\phi_{sd}^s}{dt} - \frac{l_m r_s}{\sigma l_s l_r}\phi_{rd}^s; \tag{4.34}$$

$$v_{sq}^s = \frac{r_s}{\sigma l_s}\phi_{sq}^s + \frac{d\phi_{sq}^s}{dt} - \frac{l_m r_s}{\sigma l_s l_r}\phi_{rq}^s. \tag{4.35}$$

esd^s and esq^s are disturbances:

$$esd^s = -\frac{l_m r_s}{\sigma l_s l_r}\phi_{rd}^s; \tag{4.36}$$

$$esq^q = -\frac{l_m r_s}{\sigma l_s l_r}\phi_{rq}^s. \tag{4.37}$$

In order to control equation for T_e, it is adopted the stator flux referential, $\omega_g = \omega_a$, where $\omega_{ar} = \omega_a - \omega_r$ is the stator flux slipe frequency. It is assumed the steady state for ϕ_r^g in the equation (4.26):

$$0 = r_r i_r^g + \underbrace{\frac{d\phi_r^g}{dt}}_{0} + j(\omega_{ar})\phi_r^g. \tag{4.38}$$

Isolating ϕ_r^g from equation (4.38):

$$\phi_r^g = \frac{r_r i_r^g}{j(\omega_{ar})}. \tag{4.39}$$

Applying equation (4.39) in equation (4.24):

$$\frac{r_r i_r^g}{j(\omega_{ar})} = l_r i_r^g + l_m i_s^g. \tag{4.40}$$

Isolating i_r^g from equation (4.40):

$$i_r^g = \frac{\omega_{ar} l_m i_s^g}{j r_r - \omega_{ar} l_r}. \tag{4.41}$$

Applying equation (4.41) in equation (4.28):

$$i_s^g = \frac{1}{l_s}\phi_s^g - \frac{l_m}{l_s}\left(\frac{\omega_{ar} l_m i_s^g}{j r_r - \omega_{ar} l_r}\right). \tag{4.42}$$

Isolating i_s^g from equation (4.42):

$$i_s^g = \frac{jr_r - \omega_{ar} l_r}{jl_s r_r - \omega_{ar} l_r l_s + l_m^2 \omega_{ar}} \phi_s^g. \tag{4.43}$$

Multiplying this fraction by $(-jl_s r_r - \omega_{ar} l_r l_s + l_m^2 \omega_{ar})/r_r$:

$$i_s^g = \frac{jr_r - \omega_{ar} l_r}{jl_s r_r - \omega_{ar} l_r l_s + l_m^2 \omega_{ar}} \phi_s^g \frac{(-jl_s r_r - \omega_{ar} l_r l_s + l_m^2 \omega_{ar})/r_r}{(-jl_s r_r - \omega_{ar} l_r l_s + l_m^2 \omega_{ar})/r_r}. \tag{4.44}$$

Simplifying equation (4.44):

$$i_s^g = \frac{jl_m^2 \omega_{ar}}{l_s^2 r_r (1 + (\omega_{ar} \frac{l_r}{r_r} \sigma)^2)} \phi_s^g. \tag{4.45}$$

Applying equation (4.45) in equation (4.27):

$$Te = P \frac{jl_m^2 \omega_{ar}}{l_s^2 r_r (1 + (\omega_{ar} \frac{l_r}{r_r} \sigma)^2)} (\phi_s^g)^2 \sin(\delta_i - \delta_a). \tag{4.46}$$

Simplifying this expression:

$$Te = P \frac{l_m^2 \omega_{ar}}{l_s^2 r_r (1 + (\omega_{ar} \frac{l_r}{r_r} \sigma)^2)} (\phi_s^s)^2. \tag{4.47}$$

For usual slip operation (slow slip):

$$Te = \frac{P l_m^2 \omega_{ar} (\phi_s^s)^2}{r_r l_s^2}; \tag{4.48}$$

$$\phi_s^s = \phi_s e^{j\delta_a}; \tag{4.49}$$

$$\delta_a = \int_0^t \omega_{ar}(\tau) d\tau + \int_0^t \omega_r(\tau) d\tau. \tag{4.50}$$

The electromagnetic torque can be indirectly controlled by ω_{ar} since the magnitude of the flux is kept fixed. The flux can be controlled by imposition of the stator voltage components in dq.

In summary, this control can be design by the following equations:

$$v_{sd}^s = \frac{r_s}{\sigma l_s} \phi_{sd}^s + \frac{d\phi_{sd}^s}{dt}; \tag{4.51}$$

$$\frac{\phi_{sd}^s}{v_{sd}^s} = \frac{1}{\frac{r_s}{\sigma l_s} + s}; \tag{4.52}$$

$$v_{sq}^s = \frac{r_s}{\sigma l_s} \phi_{sq}^s + \frac{d\phi_{sq}^s}{dt}; \tag{4.53}$$

$$\frac{\phi_{sq}^s}{v_{sq}^s} = \frac{1}{\frac{r_s}{\sigma l_s} + s}. \tag{4.54}$$

The equation for the stator flux estimator is given by:

$$\phi_s^s = \int_0^t [v_s^s(\tau) - r_s i_s^s(\tau)] d\tau. \tag{4.55}$$

The dq components are:

$$\phi_{sd}^s = \int_0^t [v_{sd}^s(\tau) - r_s i_{sd}^s(\tau)] d\tau; \tag{4.56}$$

$$\phi_{sq}^s = \int_0^t [v_{sq}^s(\tau) - r_s i_{sq}^s(\tau)] d\tau. \tag{4.57}$$

The control diagram is shown in the Figure 4.7. It presents a cascade control, where the speed controller feeds the flux reference for the flux controllers and the superscript $*$ represents the reference.

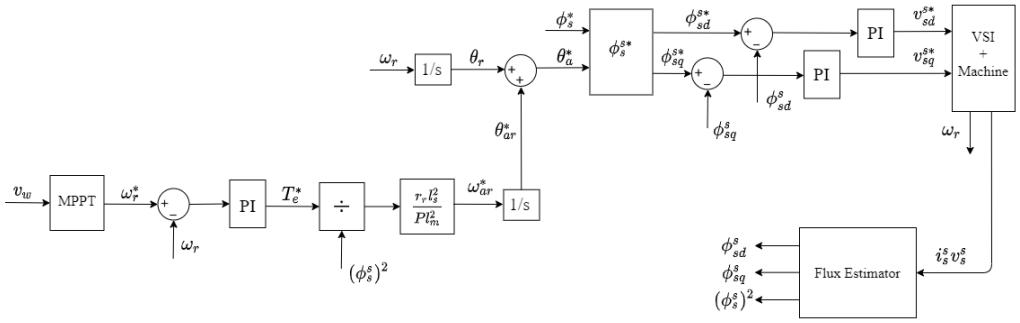

Figure 4.7: SFSC scheme.

4.5.2 Direct Torque Control (DTC)

A small variation in the Figure 4.7 scheme allows a faster torque response. The torque is directly controlled through a PI.

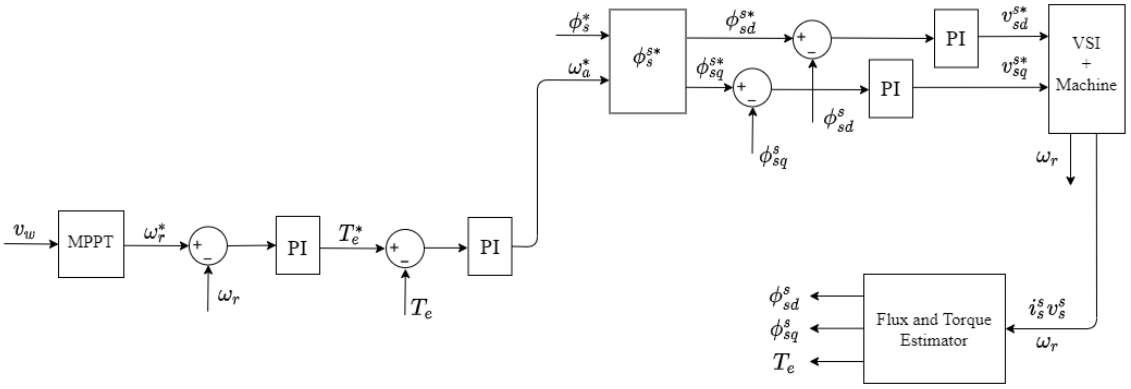

Figure 4.8: DTC scheme.

4.5.3 Rotor-Flux Slip Control (RFSC)

In this subsection RFSC is presented. Applying equation (4.29) in equation (4.26):

$$0 = r_r \left(\frac{1}{l_r} \phi_r^g - \frac{l_m}{l_r} i_s^g \right) + \frac{d\phi_r^g}{dt} + j(\omega_g - \omega_r)\phi_r^g. \tag{4.58}$$

Adopting the rotor referential r, in which $\omega_g = \omega_r$ and $\delta_g = \delta_r$, the dq components are given by:

$$\frac{r_r l_m}{l_r} i_{sd}^r = \frac{r_r}{l_r} \phi_{rd}^r + \frac{d\phi_{rd}^r}{dt}. \tag{4.59}$$

The transfer function is give by:

$$\frac{\phi_{rd}^r}{i_{sd}^r} = \frac{r_r l_m}{lr(\frac{r_r}{lr} + s)}. \tag{4.60}$$

The q component:

$$\frac{r_r l_m}{l_r} i_{sd}^r = \frac{r_r}{l_r} \phi_{rd}^r + \frac{d\phi_{rd}^r}{dt}. \tag{4.61}$$

The transfer function is give by:

$$\frac{\phi_{rq}^r}{i_{sq}^r} = \frac{r_r l_m}{lr(\frac{r_r}{l_r} + s)}. \tag{4.62}$$

The T_e for this control is defined by the equation (4.27) adopting the rotor flux referential b, in which $\phi_{rd}^b = \phi_r$, $\phi_{rq}^b = 0$, $\omega_g = \omega_b$ and $\delta_g = \delta_b$:

$$Te = P\frac{l_m}{l_r}(i_{sd}^b + j i_{sq}^b)(\phi_{rd}^b + j\phi_{rq}^b)\sin(\delta_i - \delta_b) = P\frac{l_m}{l_r}\phi_{rd}^b i_{sq}^b. \tag{4.63}$$

i_{sq}^b can be found by the equation (4.58) in rotor flux referential b, in which $\phi_{rd}^b = \phi_r$, $\phi_{rq}^b = 0$, $\omega_g = \omega_b$ and $\delta_g = \delta_b$:

$$0 = \frac{r_r}{l_r}\phi^b_{rd} - \frac{r_r l_m}{l_r} i^b_s + \frac{d\phi^b_{rd}}{dt} + j(\omega_{br})\phi^b_{rd}. \tag{4.64}$$

With the assumption of steady state, the q component is defined by:

$$\frac{r_r l_m}{l_r} i^b_{sq} = \omega_{br}\phi^b_{rd}. \tag{4.65}$$

Applying i^b_{sq} from the equation (4.65) in equation (4.63):

$$Te = P\frac{l_m}{l_r}\phi^b_{rd}\left(\frac{\omega_{br} l_r}{r_r l_m}\phi^b_{rd}\right). \tag{4.66}$$

Simplifying this expression:

$$Te = P\frac{\omega_{br}}{r_r}(\phi^b_{rd})^2. \tag{4.67}$$

The equation for the rotor flux estimator in stator referential is given by:

$$\phi^s_r = \frac{l_r}{l_m}\phi^s_s - \frac{\sigma l_r ls}{l_m} i^s_s. \tag{4.68}$$

The dq components are:

$$\phi^s_{rd} = \frac{l_r}{l_m}\phi^s_{sd} - \frac{\sigma l_r l_s}{l_m} i^s_{sd}; \tag{4.69}$$

$$\phi^s_{rq} = \frac{l_r}{l_m}\phi^s_{sq} - \frac{\sigma l_r l_s}{l_m} i^s_{sq}. \tag{4.70}$$

The Figure 4.9 presents the scheme. A change in referential rotor flux estimator of the equations (4.69) and (4.70) is performed.

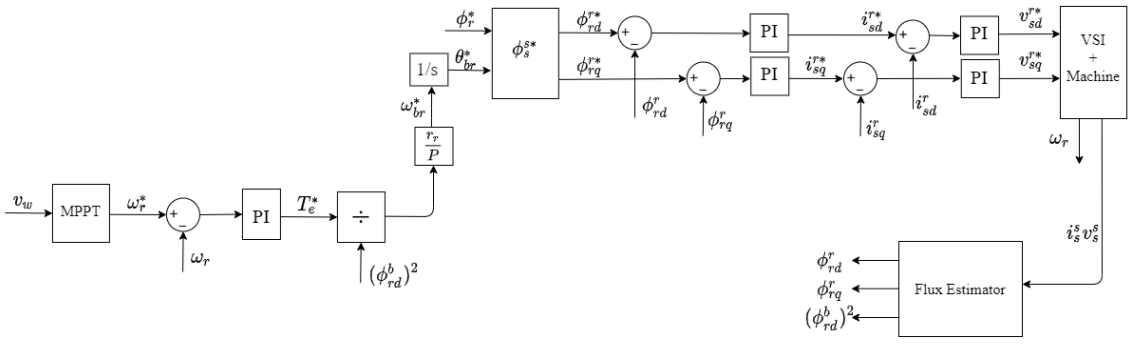

Figure 4.9: RFSC scheme.

4.5.4 Direct Stator-Field-Oriented Control (DSFOC)

In this subsection DSFOC is presented. Isolating i^g_r from equation (4.23):

$$i_r^g = \frac{1}{l_m}\phi_s^g - \frac{l_s}{l_m}i_s^g. \tag{4.71}$$

Applying equation (4.71) in equation (4.24):

$$\phi_r^g = l_r\left(\frac{1}{l_m}\phi_s^g - \frac{l_s}{l_m}i_s^g\right) + l_m i_s^g. \tag{4.72}$$

Applying equation (4.71) and equation (4.72) in equation (4.26):

$$\begin{aligned} 0 = \frac{r_r}{l_m}\phi_s^g - \frac{r_r l_s}{l_m}i_s^g + \frac{d}{dt}\left(\frac{l_r}{l_m}\phi_s^g - \frac{l_r l_s}{l_m}i_s^g + l_m i_s^g\right) \\ + j(\omega_g - \omega_r)\left(\frac{l_r}{l_m}\phi_s^g - \frac{l_r l_s}{l_m}i_s^g + l_m i_s^g\right). \end{aligned} \tag{4.73}$$

Simplifying and multiplying this equation by $\frac{l_m}{l_r}$:

$$\frac{l_s l_r}{r_r}i_s^g + \sigma l_s\frac{di_s^g}{dt} + j\sigma l_s(\omega_g - \omega_r)i_s^g = \frac{l_r}{r_r}\phi_s^g + \frac{d\phi_s^g}{dt} + j(\omega_g - \omega_r)\phi_s^g. \tag{4.74}$$

Adopting the referential a, in which $\phi_{sd}^a = \phi_s$, $\phi_{sq}^a = 0$, $\omega_g = \omega_a$ and $\delta_g = \delta_a$, the d component is:

If $-\sigma l_s \omega_{ar} i_{sq}^a$ is considered a disturbance, it is possible to control the flux through the following equation:

$$\frac{l_s l_r}{r_r}i_{sd}^a + \sigma l_s\frac{di_{sd}^a}{dt} = \frac{l_r}{r_r}\phi_{sd}^a + \frac{d\phi_{sd}^a}{dt}. \tag{4.75}$$

The transfer function is given by:

$$\frac{\phi_{sd}^a}{i_{sd}^a} = \frac{l_s + (\sigma l_s\frac{l_r}{r_r})s}{s\frac{l_r}{r_r} + 1}. \tag{4.76}$$

From the equation (4.27) and adopting the flux referential a:

$$Te = Pi_{sq}^a\phi_s. \tag{4.77}$$

The Figure 4.10 presents the scheme:

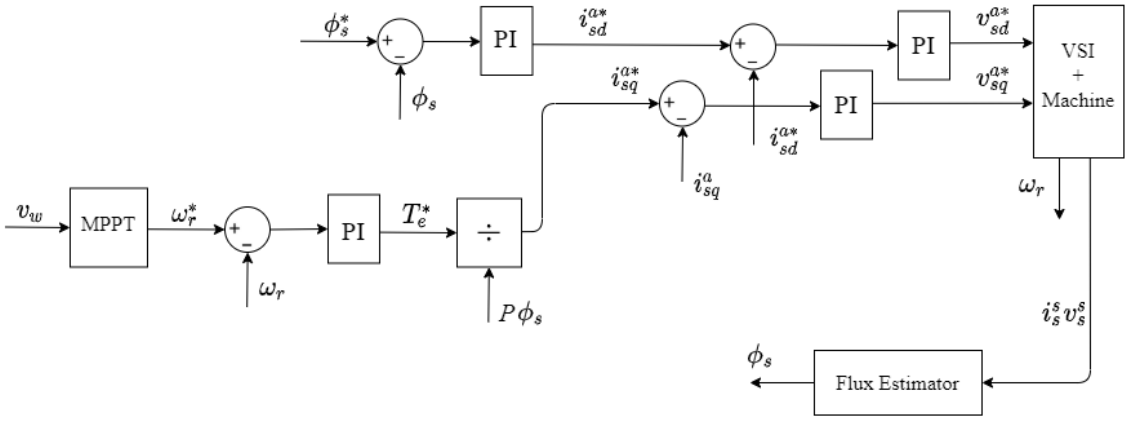

Figure 4.10: DSFOC scheme.

4.5.5 Direct Rotor-Field-Oriented Control (DRFOC)

In this subsection DRFOC is presented. Applying equation (4.29) in equation (4.26):

$$0 = r_r\left(\frac{1}{l_r}\phi_r^g - \frac{l_m}{l_r}i_s^g\right) + \frac{d\phi_r^g}{dt} + j(\omega_g - \omega_r)\phi_r^g. \tag{4.78}$$

Using the rotor reference b, in which $\phi_{rd}^b = \phi_r$, $\phi_{rq}^b = 0$, $\omega_g = \omega_b$ and $\delta_g = \delta_b$:

$$0 = \frac{r_r}{l_r}\phi_r^b - \frac{r_r l_m}{l_r}i_s^b + \frac{d\phi_r^b}{dt} + j(\omega_{br})\phi_r^b. \tag{4.79}$$

The component in the d axis does not have imaginary parts leading to:

$$\frac{r_r l_m}{l_r}i_{sd}^b = \frac{r_r}{l_r}\phi_r^b + \frac{d\phi_r^b}{dt}. \tag{4.80}$$

The transfer function is given by:

$$\frac{\phi_r^b}{i_{sd}^b} = \frac{r_r l_m}{r_r + l_r s}. \tag{4.81}$$

For the T_e can be found by adopting the flux referential b, in which $i_{sq}^b = i_s sin(\delta_i - \delta_a)$:

$$Te = P\frac{l_m}{l_r}i_{sq}^b\phi_r. \tag{4.82}$$

The Figure 4.11 presents the scheme:

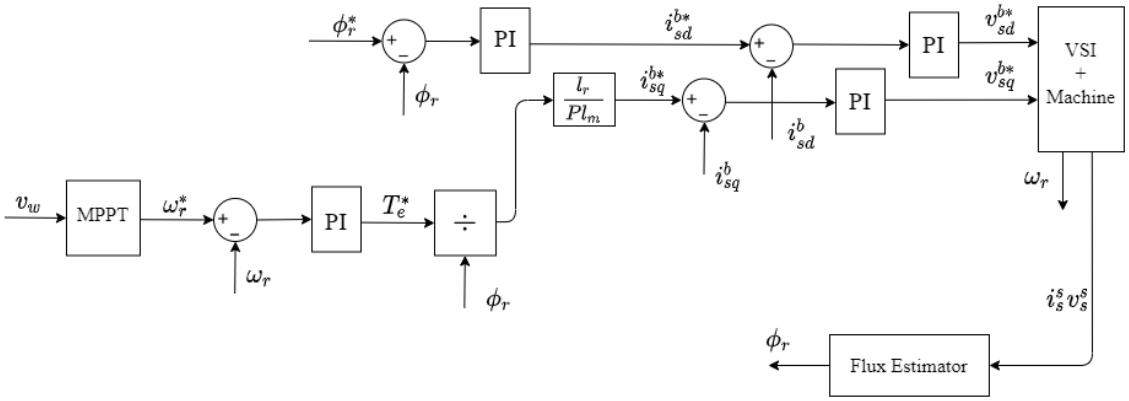

Figure 4.11: DRFOC scheme.

4.5.6 Current Control

In this work, current control is needed in RFSC, DSFOC and DRFOC. A generic expression for its design is presented in this subsection.

Applying equation (4.23) in equation (4.25):

$$v_s^g = r_s i_s^g + \frac{d}{dt}\left(l_s i_s^g + l_m i_r^g\right) + j\omega_g\left(l_s i_s^g + l_m i_r^g\right). \tag{4.83}$$

Applying equation (4.29) in equation (4.83):

$$v_s^g = r_s i_s^g + l_s\frac{di_s^g}{dt} + l_m\frac{d}{dt}\left(\frac{1}{l_r}\phi_r^g - \frac{l_m}{l_r}i_s^g\right) + j\omega_g l_s i_s^g + j\omega_g l_m\left(\frac{1}{l_r}\phi_r^g - \frac{l_m}{l_r}i_s^g\right). \tag{4.84}$$

Simplifying this equation:

$$v_s^g = r_s i_s^g + \sigma l_s\frac{di_s^g}{dt} + \frac{l_m}{lr}\frac{d\phi_r^g}{dt} + j\omega_g\sigma l_s i s^g + j\omega_g\frac{l_m}{l_r}\phi_r^g. \tag{4.85}$$

Isolating derivative of ϕ_r^g from the equation (4.26):

$$\frac{d\phi_r^g}{dt} = -r_r i_r^g - j(\omega_g - \omega_r)\phi_r^g. \tag{4.86}$$

Applying equation (4.86) in equation (4.85):

$$v_s^g = r_s i_s^g + \sigma l_s\frac{di_s^g}{dt} + \frac{l_m}{lr}\frac{d}{dt}\left(-r_r i_r^g - j(\omega_g - \omega_r)\phi_r^g\right) + j\omega_g\sigma l_s i s^g + j\omega_g\frac{l_m}{l_r}\phi_r^g. \tag{4.87}$$

Simplifying this equation:

$$v_s^g = r_s i_s^g + \sigma l_s\frac{di_s^g}{dt} - \frac{l_m r_r}{l_r}i_r^g + j\frac{l_m}{l_r}\omega_r\phi_r^g + j\omega_g\sigma l_s i_s^g. \tag{4.88}$$

Applying equation (4.29) in equation (4.88):

$$v_s^g = r_s i_s^g + \sigma l_s \frac{di_s^g}{dt} - \frac{l_m r_r}{l_r}\left(\frac{1}{l_r}\phi_r^g - \frac{l_m}{l_r} i_s^g\right) + j\frac{l_m}{l_r}\omega_r \phi_r^g + j\omega_g \sigma l_s i_s^g. \tag{4.89}$$

Simplifying this expression and knowing that $l_m^2/l_r = l_s - \sigma l_s$:

$$v_s^g = \left(r_s + \frac{r_r(l_s - \sigma l_s)}{l_r}\right) i_s^g + \sigma l_s \frac{di_s^g}{dt} + j\omega_g \sigma l_s i_s^g + j\frac{l_m}{l_r}\omega_r \phi_r^g - \frac{l_m r_r}{l_r^2}\phi_r^g. \tag{4.90}$$

With this expression it is possible to design the current controller through the following equation:

$$v_s^g = \left(r_s + \frac{r_r(l_s - \sigma l_s)}{l_r}\right) i_s^g + \sigma l_s \frac{di_s^g}{dt} + e_s^g. \tag{4.91}$$

The transfer function is given by:

$$\frac{i_s^g}{v_s^g} = \frac{1}{\left(r_s + \frac{r_r(l_s - \sigma l_s)}{l_r}\right) + \sigma l_s s}. \tag{4.92}$$

e_s^g is considered a disturbance:

$$e_s^g = j\omega_g \sigma l_s i_s^g + j\frac{l_m}{l_r}\omega_r \phi_r^g - \frac{l_m r_r}{l_r^2}\phi_r^g. \tag{4.93}$$

4.6 Grid-Side Control

Conventionally, the MPPT is done by the voltage source converter 1 (VSC 1) in WECS with SCIG connected to the grid by a back-to-back, while through voltage source converter 2 (VSC 2) is done the grid-side control. The 2L-VSC is used in both VSC 1 and VSC 2 as presented by Fernandes et al. (2013) and Barros & Barros (2017).

The grid side control is responsible to deliver the power to the grid. The active power control has two parts, the first is responsible to keep the voltage in the capacitor. The other controls the current i_{fd}. The reactive power of reference controls the current i_{fq}. The angle θ_G is estimated by the phase-locker loop (PLL) and the referential adopted is the grid voltage, denoted by superscript G. The diagram is shown in the Figure 4.12.

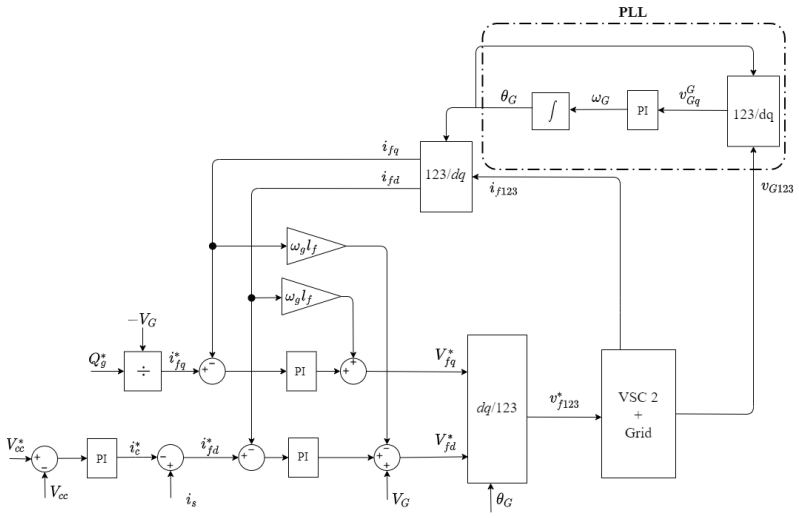

Figure 4.12: Grid-side control used in the WECS.

The connection to the grid is performed through the three-phase RL filter. The filter model in dq with the grid referential is:

$$v^G_{fd} = r_f i^G_{fd} + l_f \frac{di^G_{fd}}{dt} - \omega_G l_f i^G_{fq} + V_G; \tag{4.94}$$

$$v^G_{fq} = r_f i^G_{fq} + l_f \frac{di^G_{fq}}{dt} - \omega_G l_f i^G_{fd}. \tag{4.95}$$

In this referential, the active and reactive powers delivered to the grid are given by:

$$P_g = V_G i^G_{fd}; \tag{4.96}$$

$$Q_g = -V_G i^G_{fq}. \tag{4.97}$$

The dynamic of the capacitor is given by:

$$C\frac{dV_{cc}}{dt} = \frac{P_s - P_f}{V_{cc}}. \tag{4.98}$$

Where $v_{f,dq}$ is the voltage vectors in dq components applied by the converter, i_{f123} is the grid currents, i_s is the current provided by VSC 1, v_{f123} is the voltage applied by the converter, V_G is the absolute of grid voltage vector, v_{G123} is the grid voltages, V_{Gq} is the grid voltage vector in q component, $i_{f,dq}$ is the current vector in dq, ω_G is the grid angular frequency, θ_G is the grid angular position, l_f is the filter inductance, r_f is the filter resistance, P_g is the active power delivered to the grid, Q_g is the reactive power delivered to the grid, V_{cc} is the voltage in the capacitor, C is the capacitance, P_s is the power provided by VSC 1 and P_f is the power provided by VSC 2.

4.7 PWM Model

The topology of the converters consists of six insulated gate bipolar transistor, two of them for each branch, as shown in Figure 4.6. The IGBT's of the same branch cannot conduct at the same time.

The phase disposition pulse width modulation is used for the switching control as presented by Santos (2011). It calculates, for each phase $j = 1, 2$ and 3, the interval τ_j of time that is needed the switch to conduct. The switch, in beneath and in the same branch, conducts during the interval $\tau - \tau_j$, where τ is the total period of switching conducting and not conducting.

For each period of PWM the command sets the average pole voltage $(\overline{v_{10}}, \overline{v_{20}}, \overline{v_{30}})$ of mean value equals to the sinusoidal reference given by the controller v^*_{s123}, where a single fase is given by $v_{ref} = v^*_{sj}$. The pole mean voltage for a phase j is calculated by:

$$\overline{v_{j0}} = v_{ref} = \frac{1}{\tau}[\tau_j \frac{V_{cc}}{2} - (\tau - \tau_j)\frac{V_{cc}}{2}] \tag{4.99}$$

From equation (4.99):

$$\tau_j = (\frac{v_{ref}}{V_{cc}} + \frac{1}{2})\tau \tag{4.100}$$

From this equation, it is possible to determine the interval τ_j.

4.8 Conclusion

In this chapter, the models used in the simulations are presented. The turbine model deals with the capturing of the energy of wind by the blades and the conversion in rotating mechanical energy. This energy is transferred to the rotor by the coupling of the turbine and the generator by the two-mass model. Then, the electrical model is presented, followed by the control strategies. The grid-side control is presented with the PD-PWM.

The following chapter deals with the implementation and results of the five control strategies applied in SCIG-based WECS. They are evaluated by MPPT, THD, inrush current and dyncamic response at this work.

Chapter 5

Implementation and Results

This chapter presents the final results of the control strategies for SCIG-based WECS, which are evaluated by the following performance indexes at this work: MPPT, THD, inrush current and dyncamic response and the machine-side control response with three-phase fault and load rejection circumstances. The voltage in DC-link is 1500 V, the capacitor is 2mF and the converter frequency is 5000 Hz. The simulations are performed with fixed-step size of 1e-5 s. The Table 5.1 presents the machine parameters, the Table 5.2 presents the turbine parameters and the Table 5.3 presents the grid-side control used in all control strategies. The control parameters were achieved by trial and error method and the reference for the THD limit is 5% according to suggestion of IEEE (2014).

Table 5.1: SCIG parameters used in the simulations

Parameter	**Value**
Voltage	380/220 (V)
Power	3400 (W)
Resistance: R_s and R_r	2.8237 (Ω)
Self-inductance: L_s and L_r	0.2140 (H)
Linkage inductance: M_s and M_r	-0.1070 (H)
Linkage inductance: M_{sr}	0.1989 (H)
Pairs of poles: P	2
Damping constant: F_m	0.00146 ($N \cdot m \cdot s$)
Inertia constant: J_m	0.0133 ($Kg \cdot m^2$)

Table 5.2: Wind turbine parameters used in the simulations

Parameter	**Value**
Number of blades:	3
Length of the blade: R	2.1 (m)
Air density: ρ	1.21 (Kg/m^3)
Inertia constant: J_t	5 (Kg $\cdot$ m^2)
Damping constant: F_t	0.02 (N $\cdot$ m $\cdot$ s)
Tower shadowing constant: K_s	0.2
Angle of the tower shadowing: α	30 (^{o})
Gear constant: K_v	5
Torsion constant: $K_{torsion}$	10000

Table 5.3: Control parameters used in grid-side

Parameter	K_p	K_i
Voltage in the capacitor	1.6	120
PLL	30	200
Direct axis filter current	120	200
Quadrature axis filter current	120	200

5.1 SFSC

The Table 5.4 presents the parameters used in this control strategy.

Table 5.4: Control parameters used in SFSC

Parameter	K_p	K_i	K_d
Rotor speed	0.1	29	1.8
Direct axis stator flux	4000	380770.4	0
Quadrature axis stator flux	4000	380770.4	0

The Figure 5.1 presents the stator currents. With this control the machine performs a inrush current of 14.3A and presented significant variation at the amplitude since it does not have inner current control.

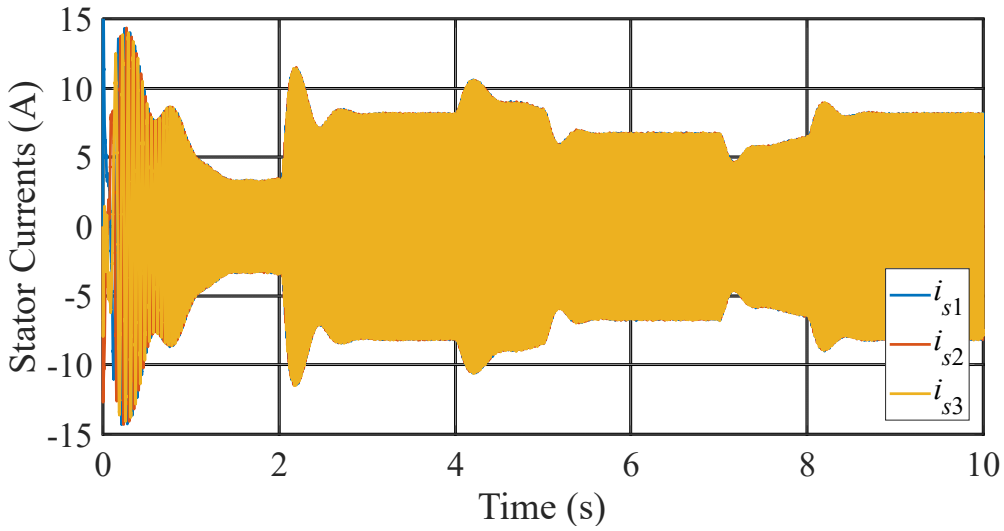

Figure 5.1: Stator currents of SFSC.

The Figure 5.2 presents the zoom of stator currents which has a desirable sinusoidal behavior.

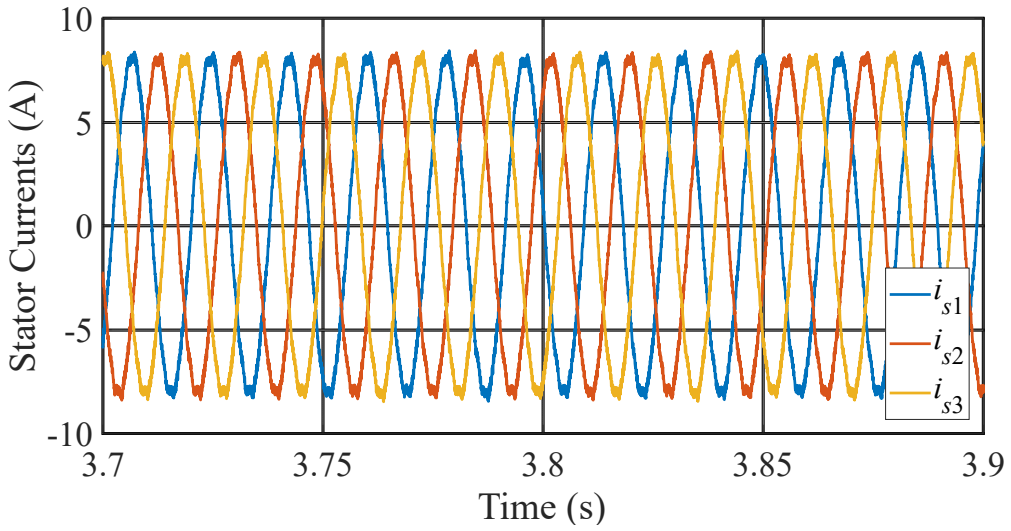

Figure 5.2: Zoom of stator currents of SFSC.

The Figure 5.3 presents the frequency spectrum of the first phase of the stator current. It presented a low THD of 3%, below the 5% recommended, since the currents can move with more freedom due to the few quantity of controllers.

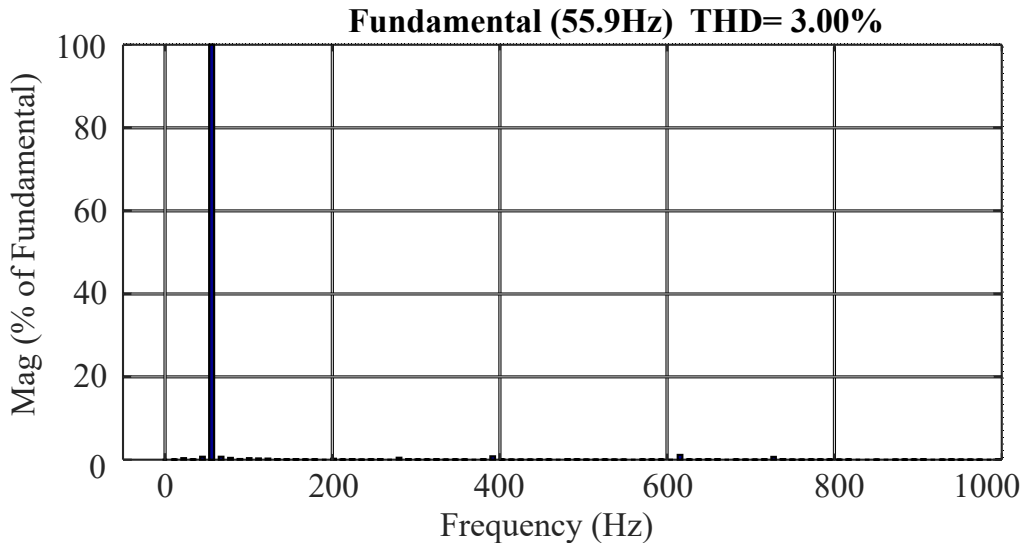

Figure 5.3: Frequency spectrum of stator current of SFSC.

The Figure 5.4 presents the *d* component of stator flux control. There is no significant variation at the amplitude and the reference presents a sinusoidal behavior due to the stator referential.

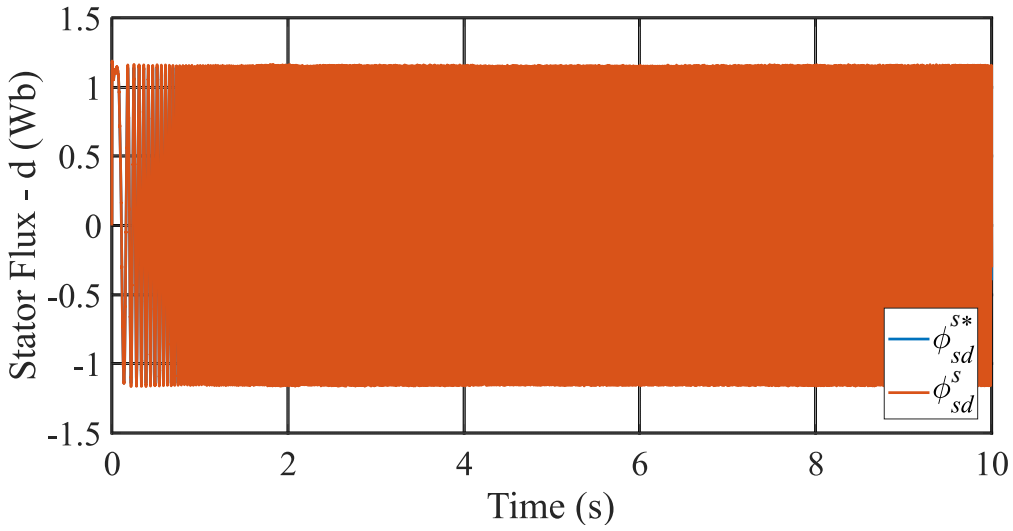

Figure 5.4: Direct component of stator flux of SFSC.

The Figure 5.5 presents the zoom of *d* component of stator flux control. It is possible to see that the flux followed the reference perfectly and it is the most desirable response.

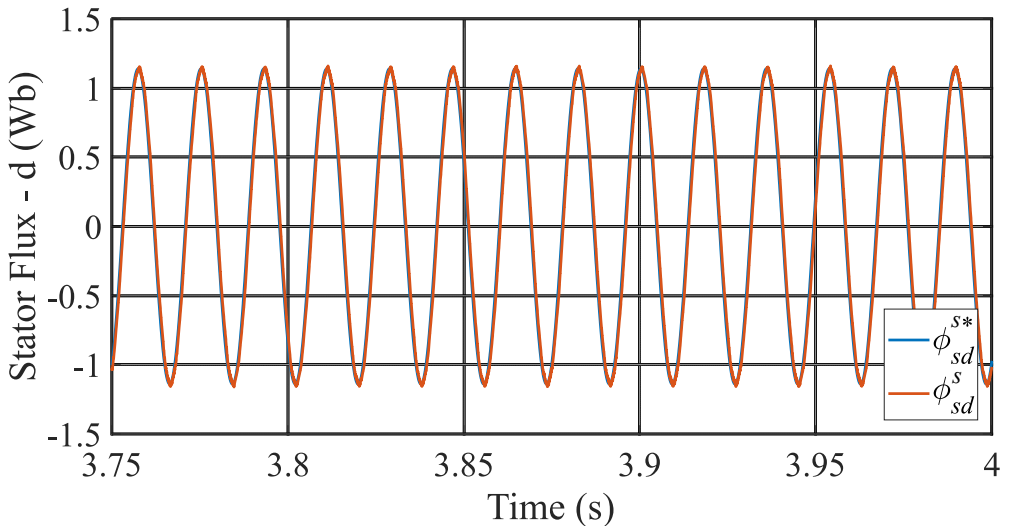

Figure 5.5: Zoom of direct component of stator flux of SFSC.

The Figure 5.6 presents the q component of stator flux control. There is no significant variation at the amplitude and the reference presents a sinusoidal behavior due to the stator referential.

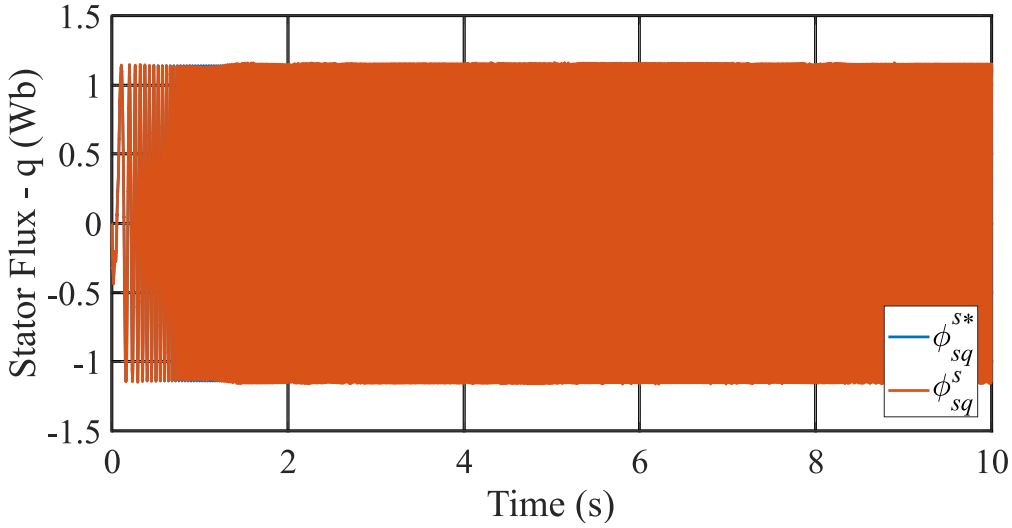

Figure 5.6: Quadrature component of stator flux of SFSC.

The Figure 5.7 presents the zoom of q component of stator flux control. It is possible to see that the flux followed the reference perfectly and it is the most desirable response.

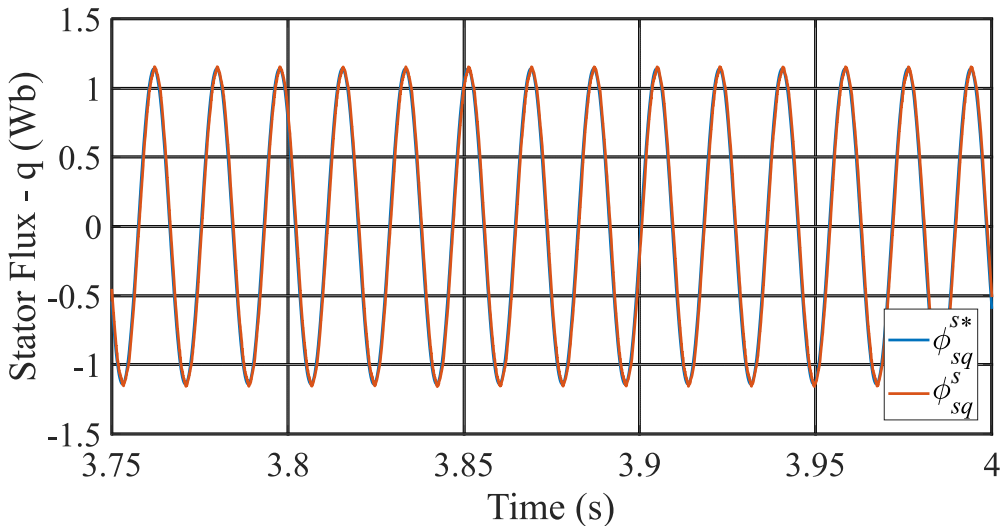

Figure 5.7: Zoom of quadrature component of stator flux of SFSC.

The Figure 5.8 presents the rotor speed. With this control there is a severe oscillation at start-up of the machine, which is not desirable, but as soon as the rotor starts rotating it tracks the reference which is the expected behavior.

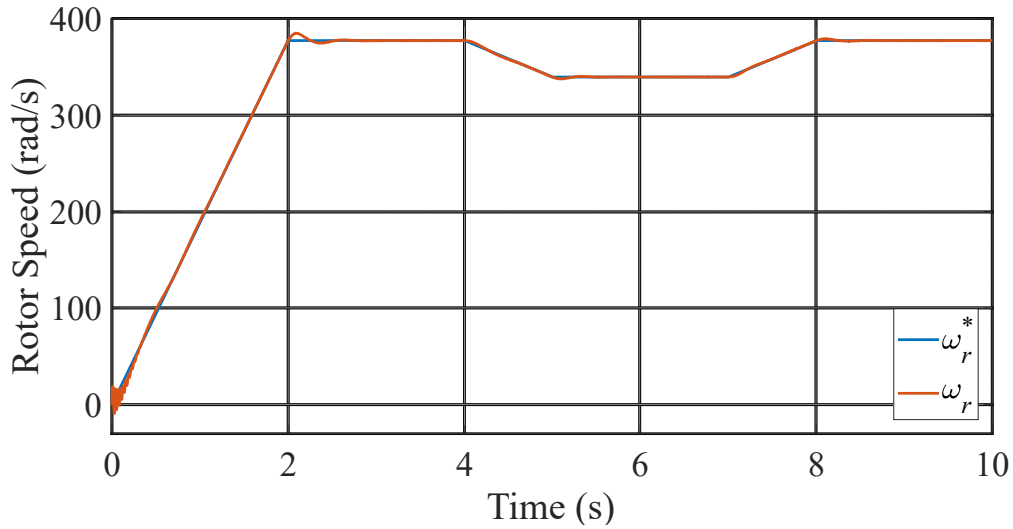

Figure 5.8: Rotor speed of SFSC.

The Figure 5.9 presents the MPPT. It is possible to see that the rotor speed followed the reference, but with an overshoot of 0.53%, which is one of the highest among the control strategies of this work and this is not desirable.

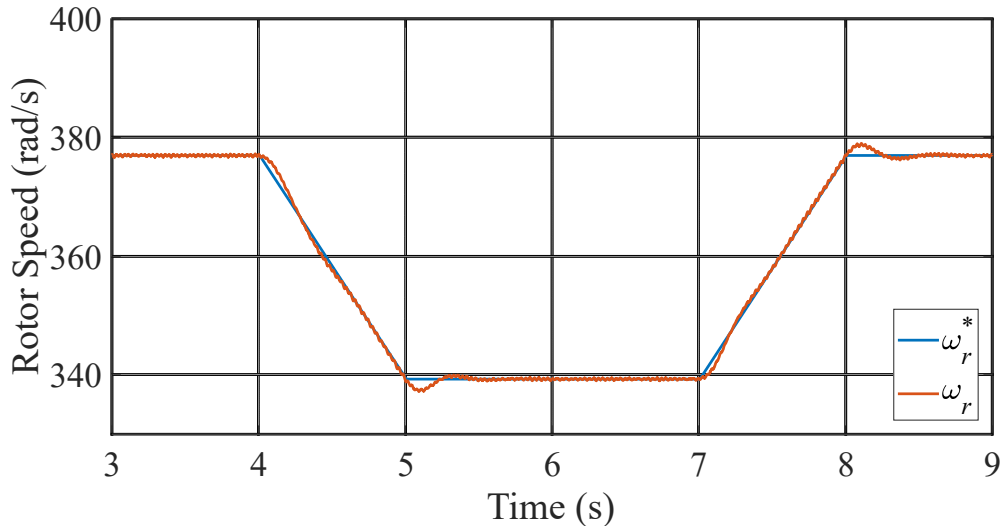

Figure 5.9: Zoom of rotor speed of SFSC.

The Figure 5.10 presents the control voltages of SFSC. It presented a desirable response since it is far from the limit of a half of de DC link voltage of the 2L-VSC used in the back-to-back converter.

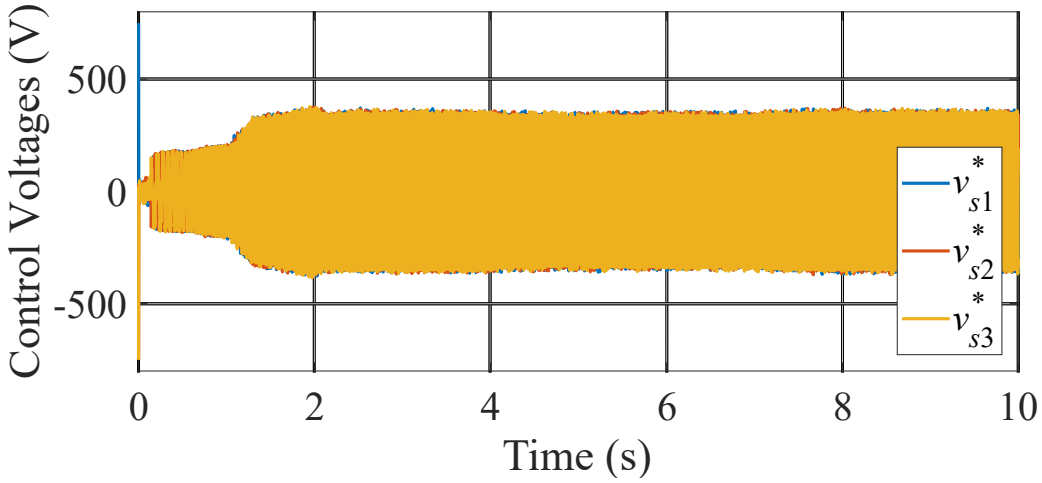

Figure 5.10: Control Voltages of SFSC.

The Figure 5.11 presents a zoom of the control voltages of SFSC. Here it is possible to see that it presented ripple and it is not a desirable response since these are control signals which are going to VSC1 to be synthesized.

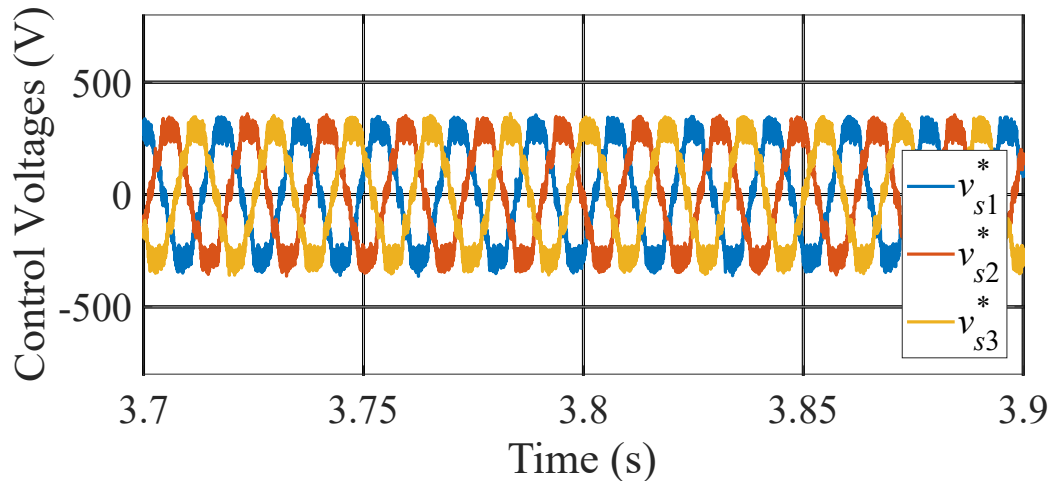

Figure 5.11: Zoom of Control Voltages of SFSC.

The Figure 5.12 presents the phase voltages of SFSC. As expected, the amplitude of the phase voltage is $2/3$ of the DC link voltage due to the 2L-VSC used in the back-to-back converter.

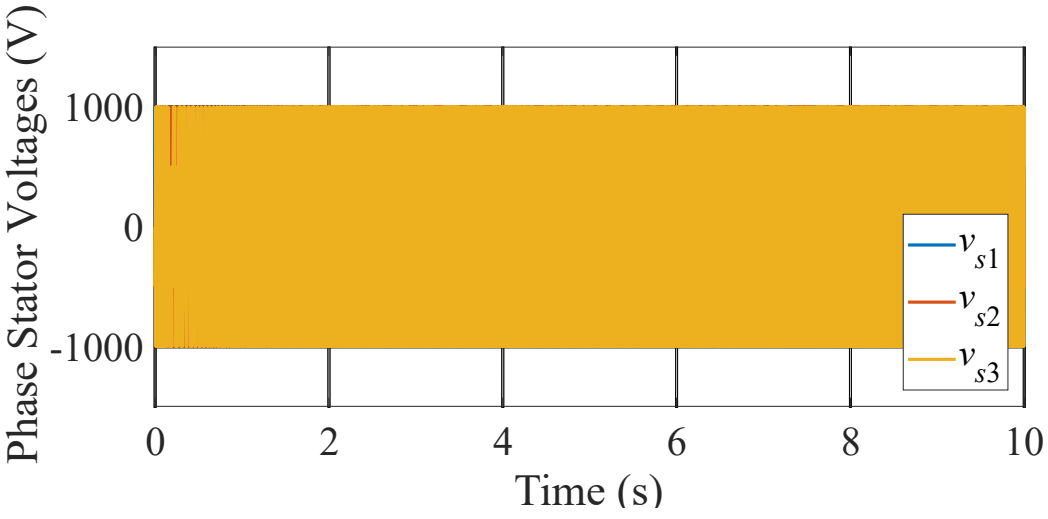

Figure 5.12: Phase Voltages of SFSC.

The Figure 5.13 presents a zoom of the phase voltages of SFSC. It presented an expected behavior since the sinusoidal wave is synthesized by the 5 operating points of the phase voltages of the 2L-VSC.

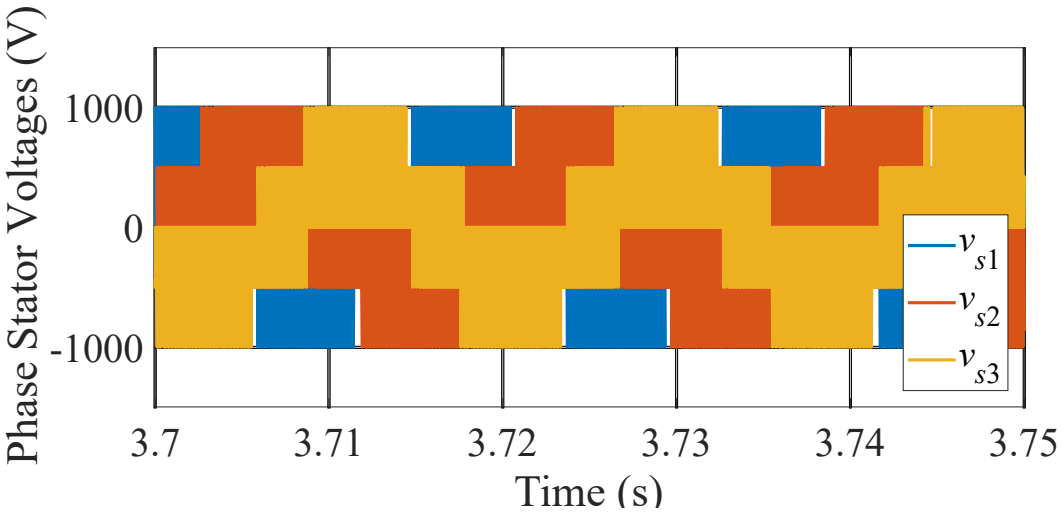

Figure 5.13: Zoom of Phase Voltages of SFSC.

5.2 DTC

The Table 5.5 presents the parameters used in this control strategy.

Table 5.5: Control parameters used in DTC

Parameter	K_p	K_i	K_d
Rotor speed	0.1	29	1.8
Electromagnetic torque	0.01	400	0
Direct axis stator flux	4000	380770.4	0
Quadrature axis stator flux	4000	380770.4	0

The Figure 5.14 presents the stator currents. With the torque control, the machine performs a inrush current of 28.5A and presented a smaller variation at the amplitude in comparison to SFSC due to the fact that controlling the torque implies in controlling the currents which is an expected behavior.

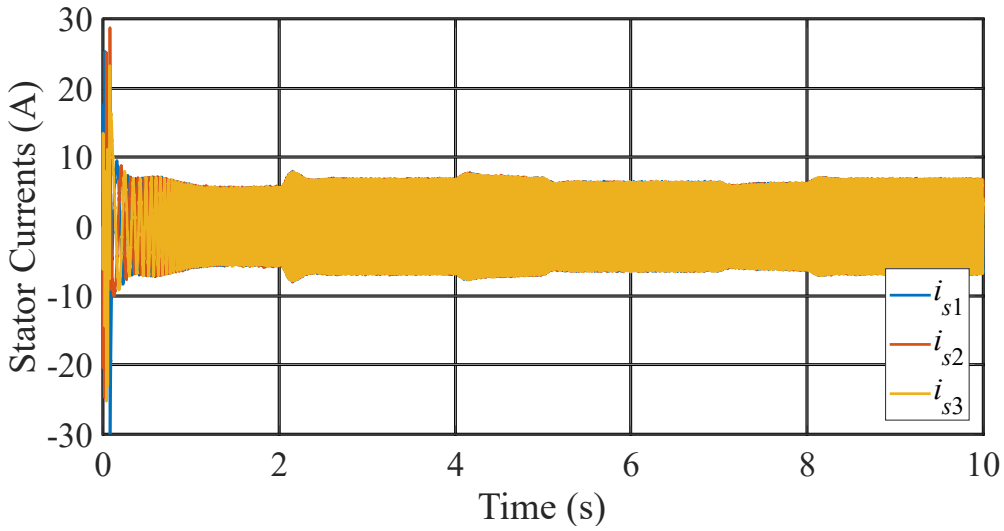

Figure 5.14: Stator currents of DTC.

The Figure 5.15 presents the zoom of stator currents. This result is expected and the closer to a perfect sine wave the better for structure longevity of the machine presenting less vibrations.

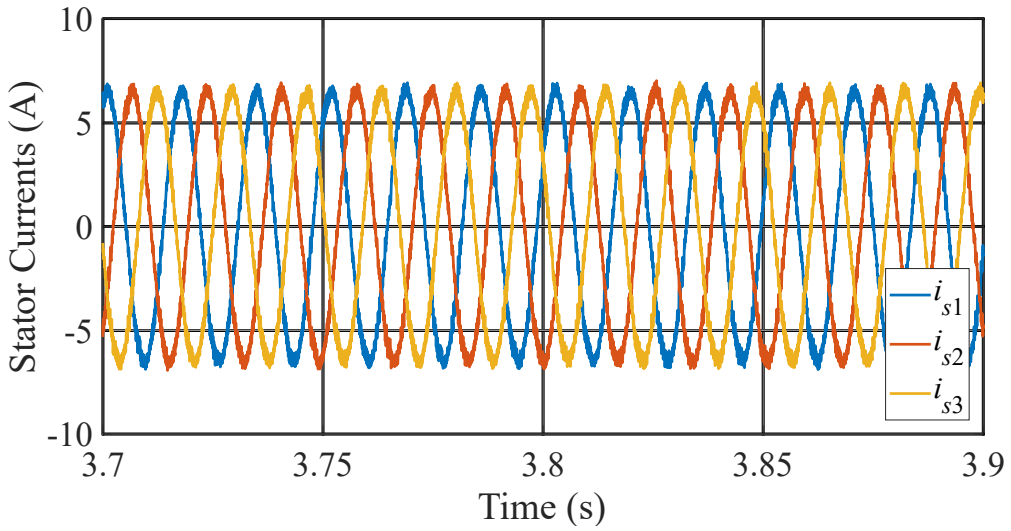

Figure 5.15: Zoom of stator currents of DTC.

The Figure 5.16 presents the frequency spectrum of the first phase of the stator current. It presented a higher THD of 5.98% in comparison to SFSC due to the torque control and above the 5% recommended. It is not a desirable response for the power quality delivered.

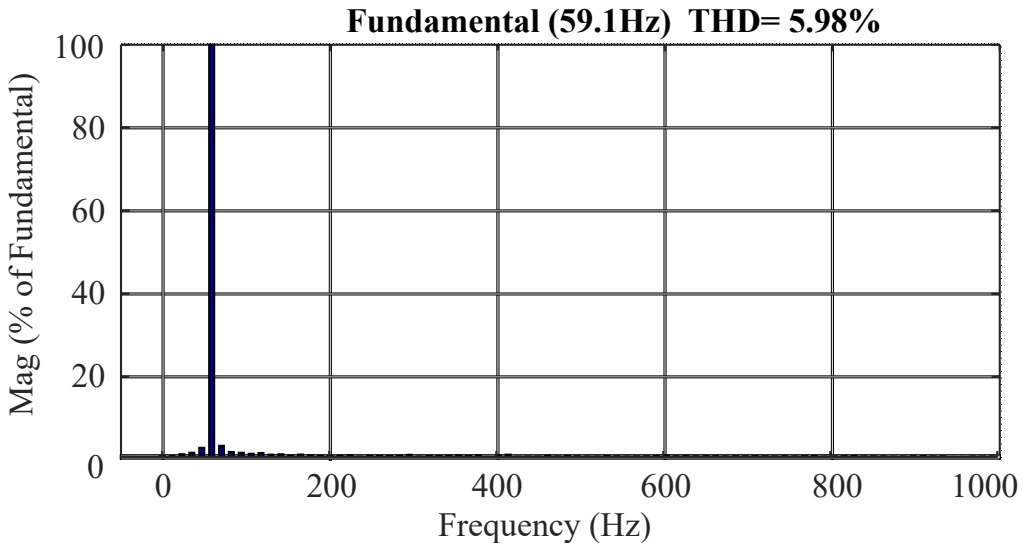

Figure 5.16: Frequency spectrum of stator current of DTC.

The electromagnetic torque presents a maximum value of 33Nm at start-up and presents a ripple of 6Nm. It presented an expected response with a positive torque since the machine is accelerating and then it has a negative response which means it is generating power.

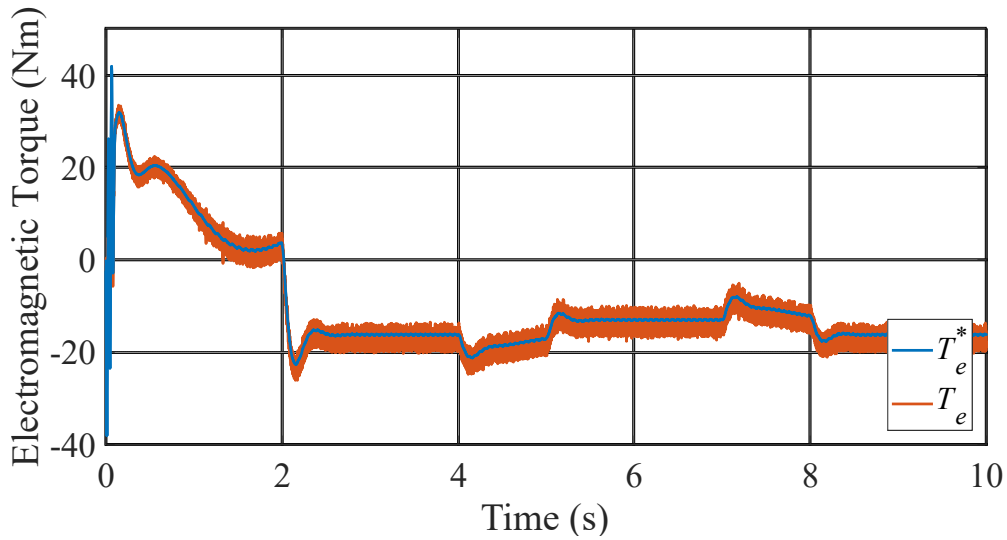

Figure 5.17: Electromagnetic torque of DTC.

The Figure 5.18 presents the *d* component of stator flux control. There is no significant variation at the amplitude, the reference presents a sinusoidal behavior due to the stator referential and it presented a slower transient in comparison to SFSC which is expected since it has one more PI control which delays the response.

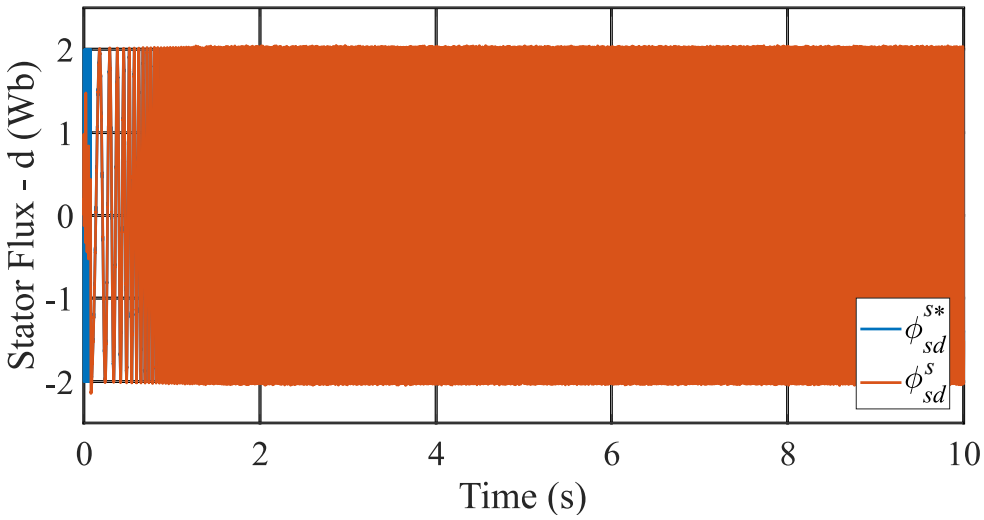

Figure 5.18: Direct component of stator flux of DTC.

The Figure 5.19 presents the zoom of *d* component of stator flux control. It is possible to see that the flux followed the reference perfectly and it is the most desirable response. The response is expected to be similar to SFSC since the control schemes are similar.

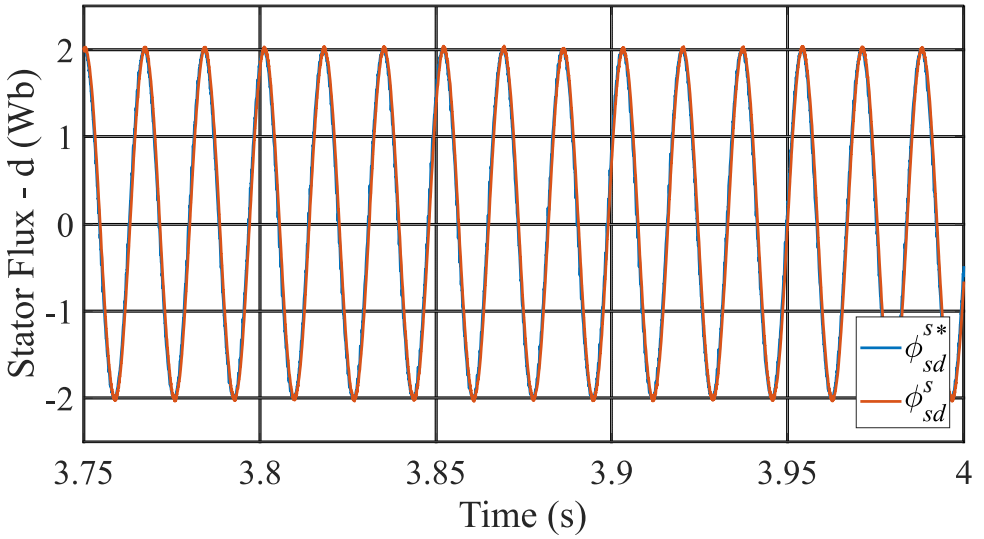

Figure 5.19: Zoom of direct component of stator flux of DTC.

The Figure 5.6 presents the *q* component of stator flux control. There is no significant variation at the amplitude , the reference presents a sinusoidal behavior due to the stator referential and it presented a slower transient in comparison to SFSC which is expected since it has one more PI control which delays the response.

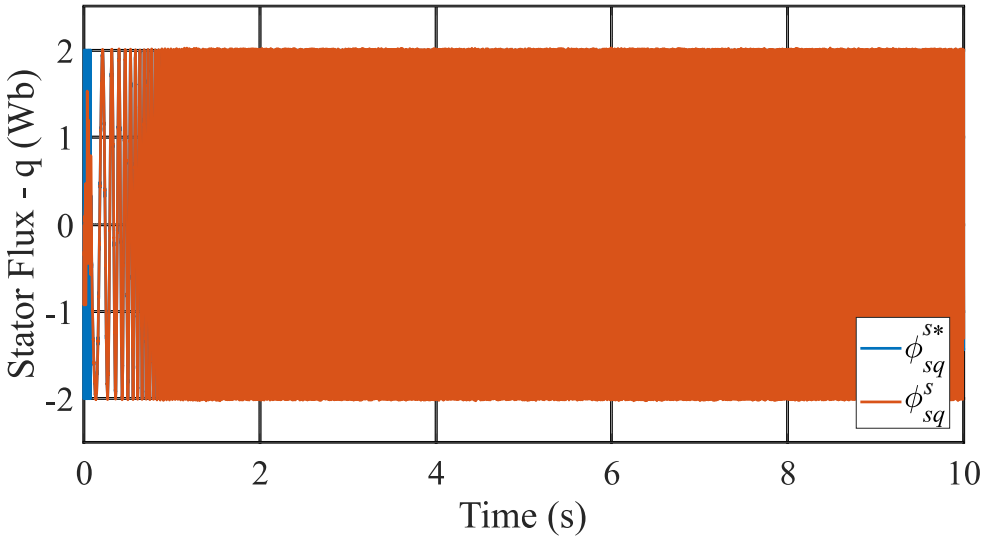

Figure 5.20: Quadrature component of stator flux of DTC.

The Figure 5.21 presents the zoom of q component of stator flux control. It is possible to see that the flux followed the reference perfectly and it is the most desirable response. The response is expected to be similar to SFSC since the control schemes are similar.

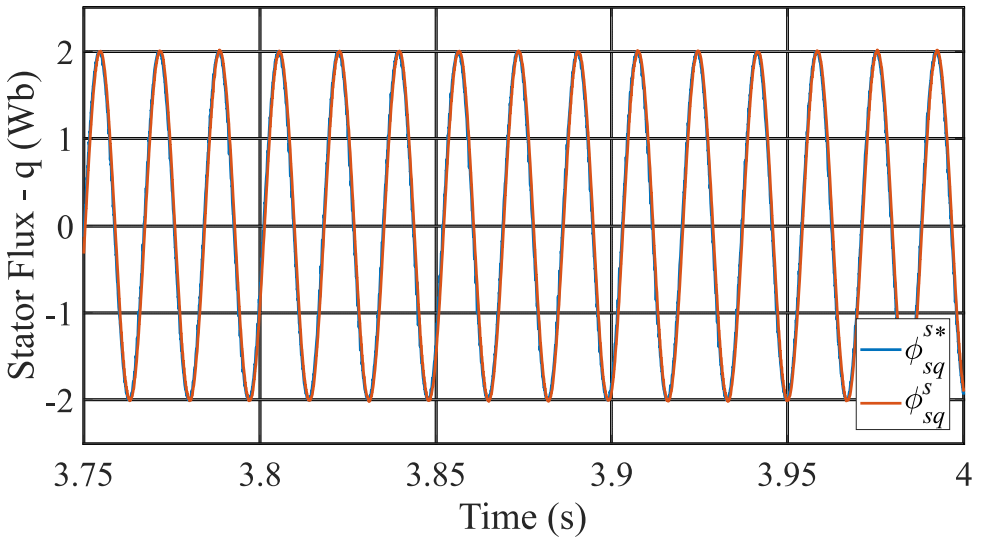

Figure 5.21: Zoom of quadrature component of stator flux of DTC.

The Figure 5.22 presents the rotor speed. With this control there is a severe oscillation at start-up of the machine, which is not desirable, but as soon as the rotor starts rotating it tracks the reference which is the expected behavior.

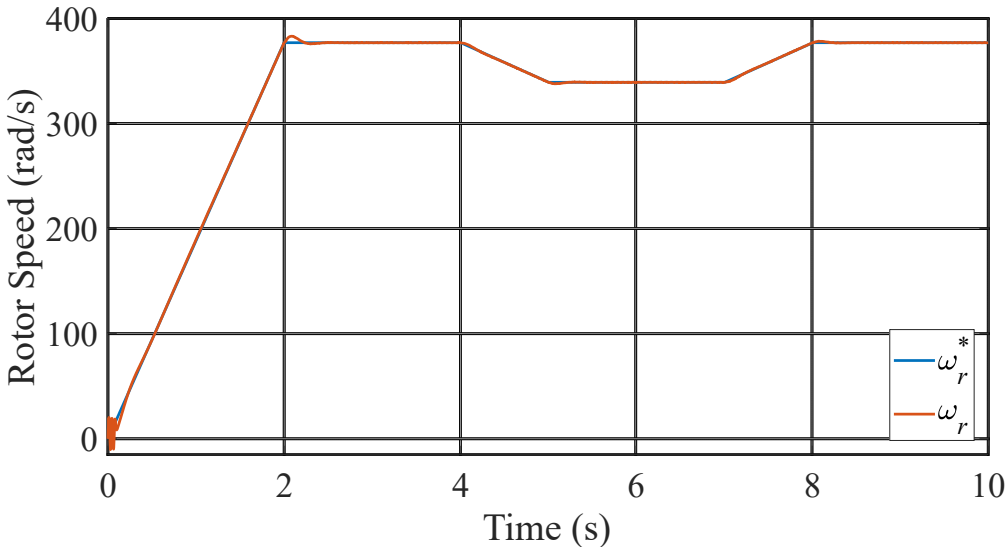

Figure 5.22: Rotor speed of DTC.

The Figure 5.23 presents the MPPT. It is possible to see that the rotor speed followed the reference, but with an overshoot of 0.37%, which is lesser than the SFSC and it is an expected behavior due to the torque controller.

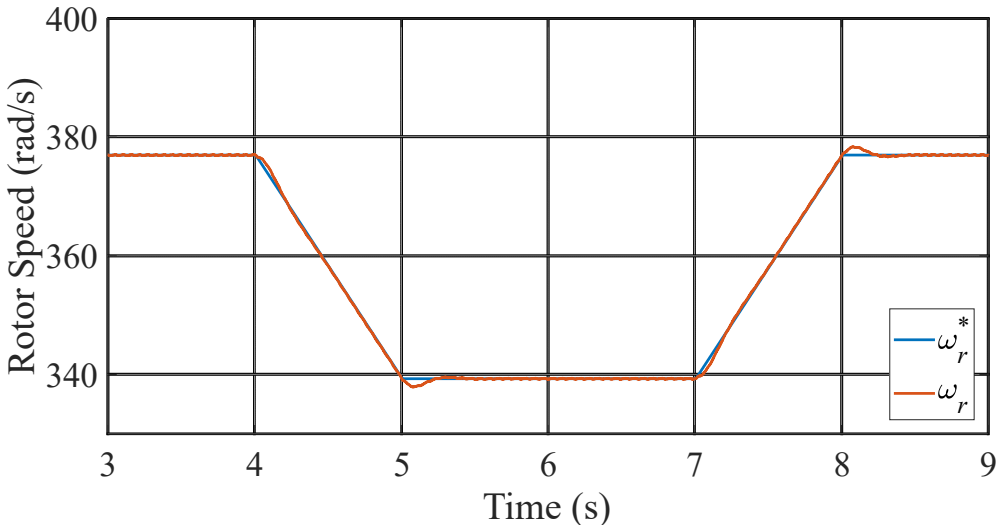

Figure 5.23: Zoom of rotor speed of DTC.

The Figure 5.24 presents the control voltages of DTC. It presented a response with the half of de DC link voltage of the 2L-VSC used in the back-to-back converter. It is not desirable since it means that this control is achieving the limit of the converter, but it is an expected result in comparison to SFSC since it has the electromagnetic torque control which imposes more stress to the system.

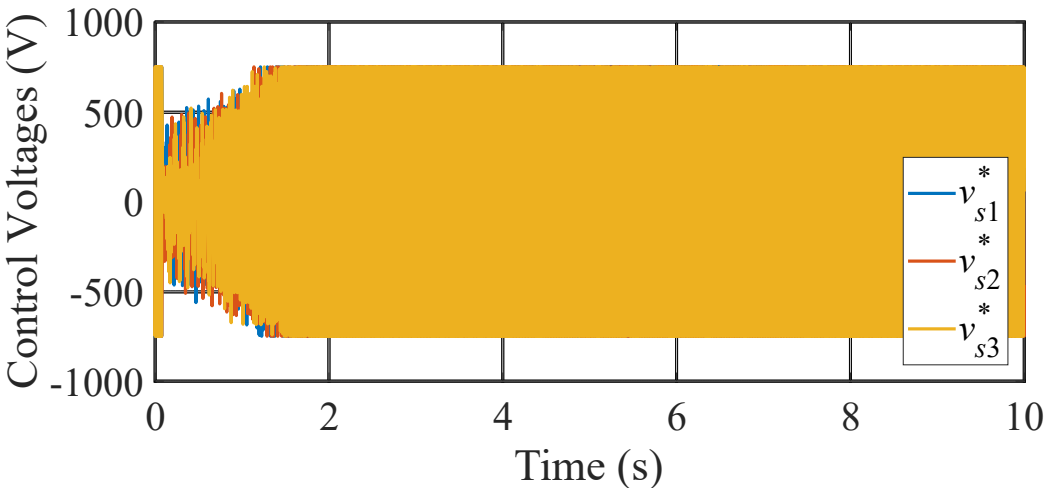

Figure 5.24: Control Voltages of DTC.

The Figure 5.25 presents a zoom of the control voltages of DTC. Here it is possible to see that it presented more ripple than the SFSC and it is not a desirable response since these are control signals which are going to VSC1 to be synthesized.

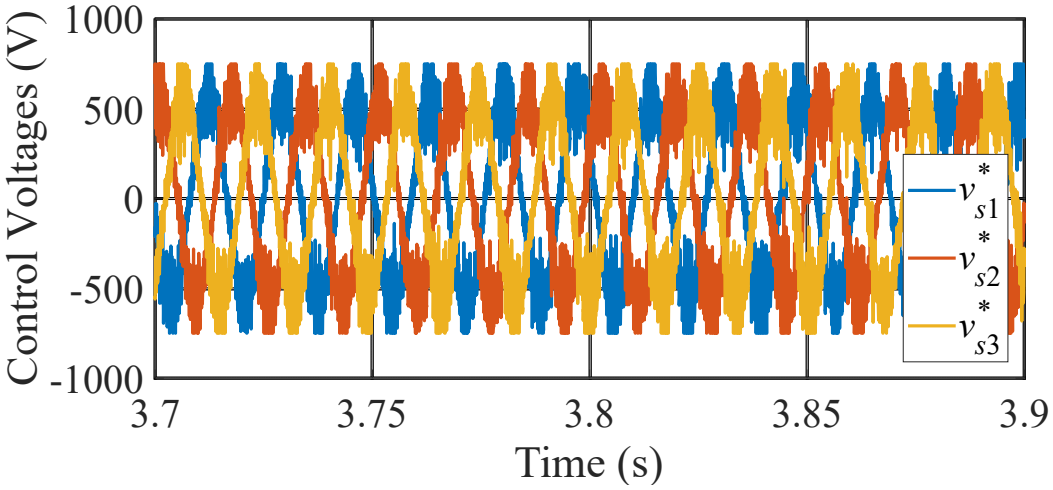

Figure 5.25: Zoom of Control Voltages of DTC.

The Figure 5.26 presents the phase voltages of DTC. As expected, the amplitude of the phase voltage is $2/3$ of the DC link voltage due to the 2L-VSC used in the back-to-back converter.

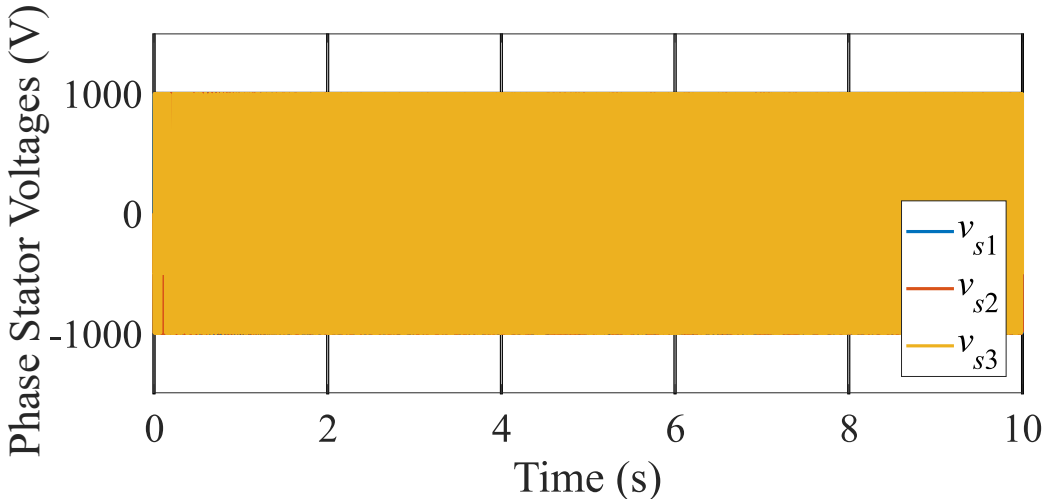

Figure 5.26: Phase Voltages of DTC.

The Figure 5.27 presents a zoom of the phase voltages of DTC. It presented an expected behavior since the sinusoidal wave is synthesized by the 5 operating points of the phase voltages of the 2L-VSC.

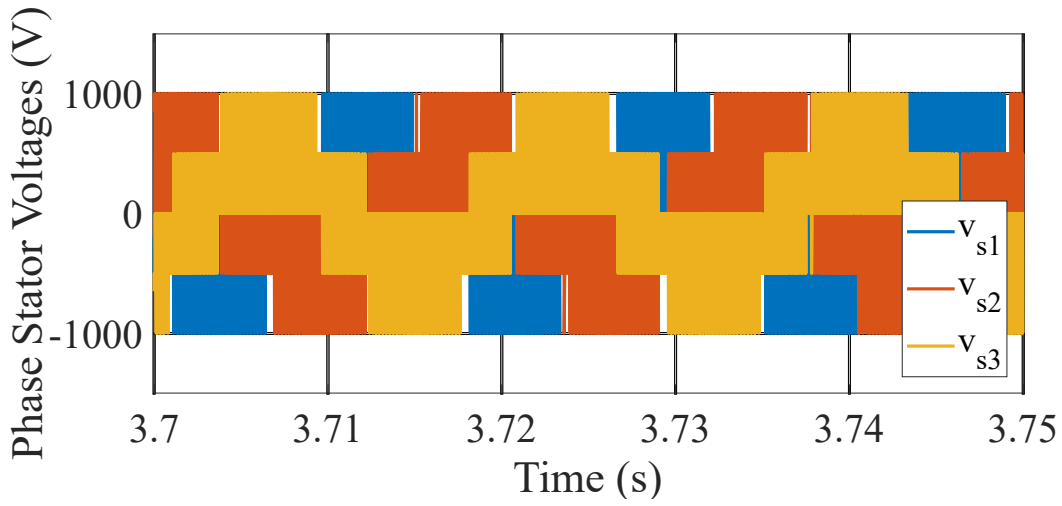

Figure 5.27: Zoom of Phase Voltages of DTC.

5.3 RFSC

The Table 5.6 presents the parameters used in this control strategy.

Table 5.6: Control parameters used in RFSC

Parameter	K_p	K_i	K_d
Rotor speed	0.1	19.8	0.49
Direct axis rotor flux	12	150	0
Quadrature axis rotor flux	12	150	0
Direct axis stator current	40	300	0
Quadrature axis stator current	40	300	0

This control strategy is the most difficult control strategy of the five, since it has the highest number of PI controllers, which increases the difficulty of fine tuning them. For this reason, the results were not as good as the others.

The Figure 5.28 presents the *d* component of rotor flux control. The machine *d* component of rotor flux presented a higher magnitude in comparison to the reference not following it properly which is not a desirable response.

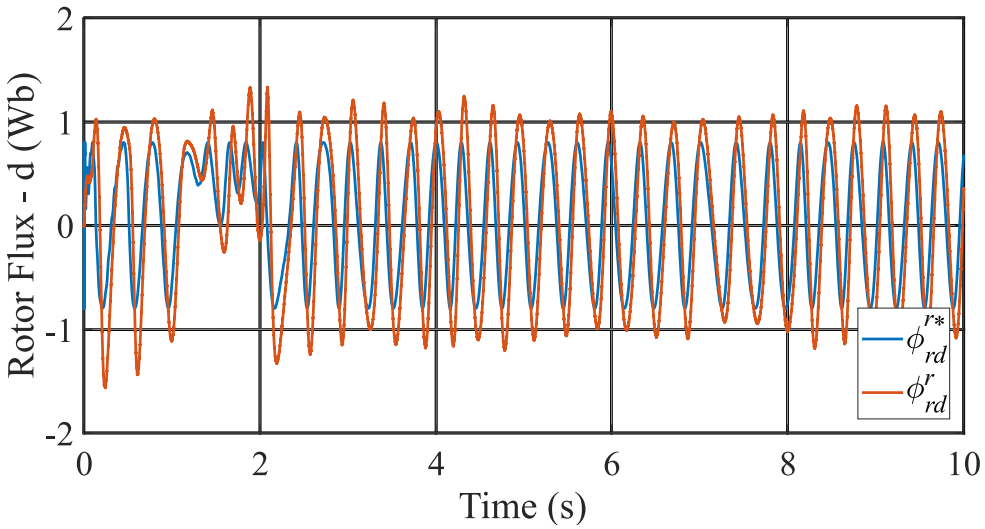

Figure 5.28: Direct component of rotor flux of RFSC.

The Figure 5.29 presents the *q* component of rotor flux control. The machine *q* component of rotor flux presented a higher magnitude in comparison to the reference not following it properly which is not a desirable response.

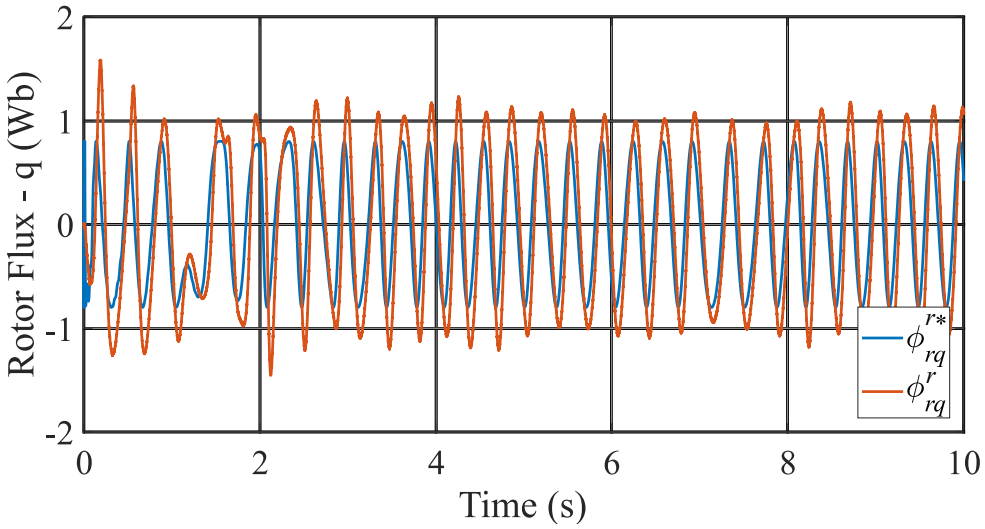

Figure 5.29: Quadrature component of rotor flux of RFSC.

The Figure 5.30 presents the stator currents. It presented the highest variation at the amplitude and presented the highest peak of current of 18A around 2s. It presented a high settling time which degraded the response.

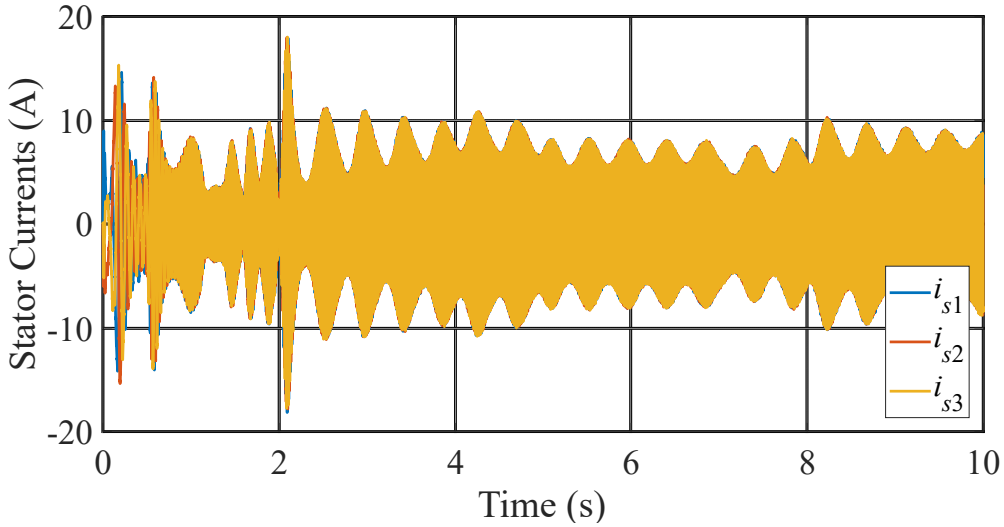

Figure 5.30: Stator currents of RFSC.

The Figure 5.31 presents a zoom of stator currents. Here, the wind is not varying, but the amplitude of the current still did not achieve the steady state and it is not a desirable response.

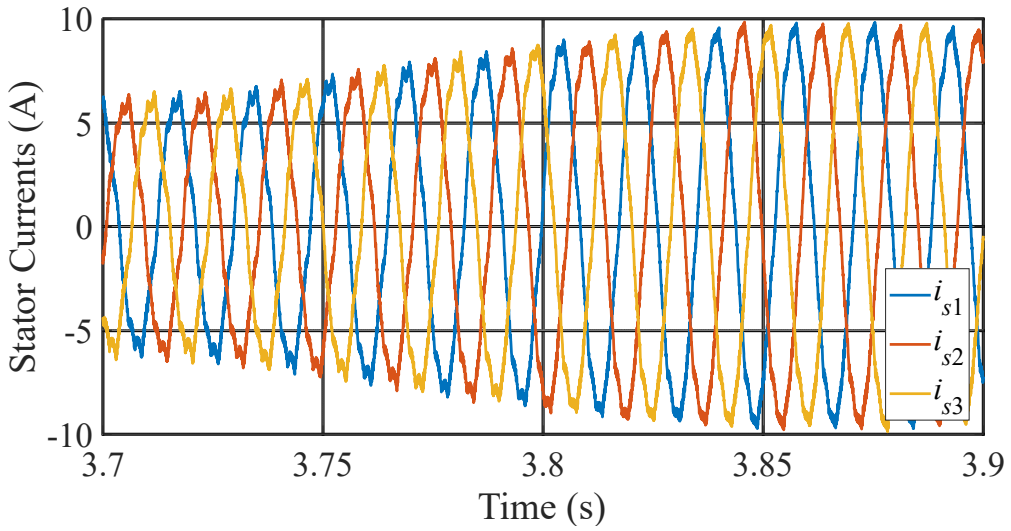

Figure 5.31: Zoom of stator currents of DSFOC.

The Figure 5.32 presents the frequency spectrum for this control. It presented one of the highest THD value among the control strategies, above the 5% recommended and it is not a desirable response.

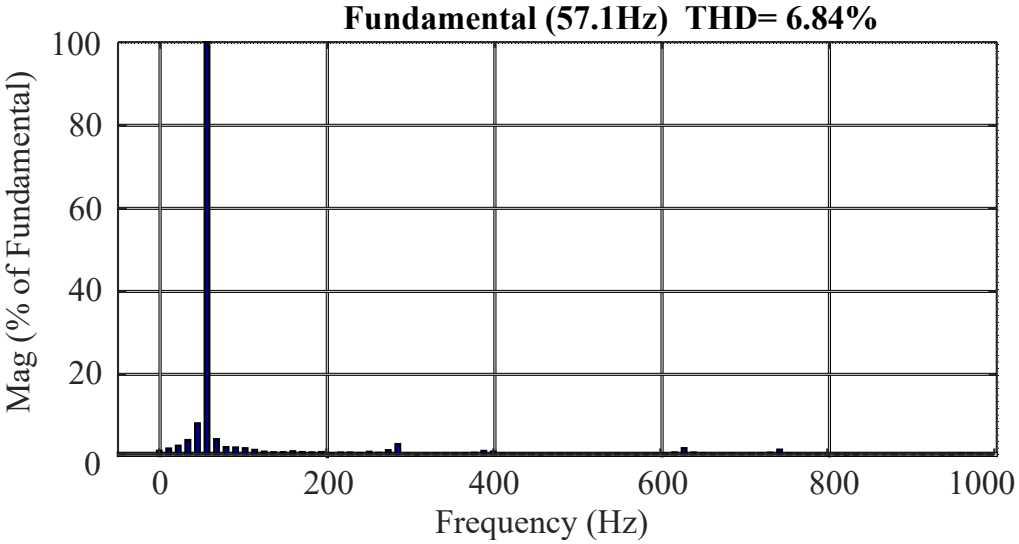

Figure 5.32: Frequency spectrum of stator current of RFSC.

The Figure 5.33 presents the *d* component of stator current control. Here, it is possible to see that the reference is varying the amplitude which makes severe oscillations in the hole system degrading the response.

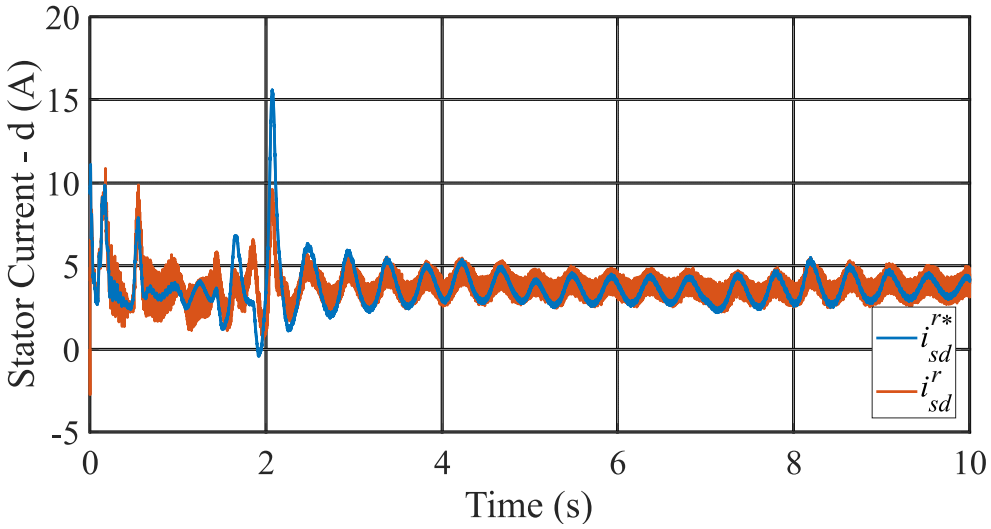

Figure 5.33: Direct component of stator current of RFSC.

The Figure 5.34 presents the q component of stator current control. Here, it is also possible to see that the reference is varying the amplitude which makes severe oscillations in the hole system degrading the response.

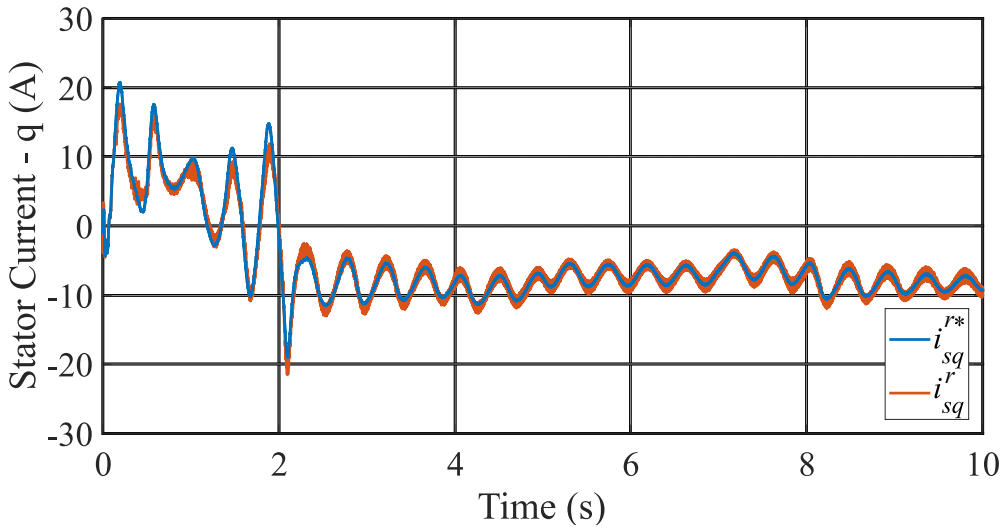

Figure 5.34: Quadrature component of stator of RFSC.

The Figure 5.35 presents the rotor speed. The rotor speed managed to followed the reference which is a desirable response.

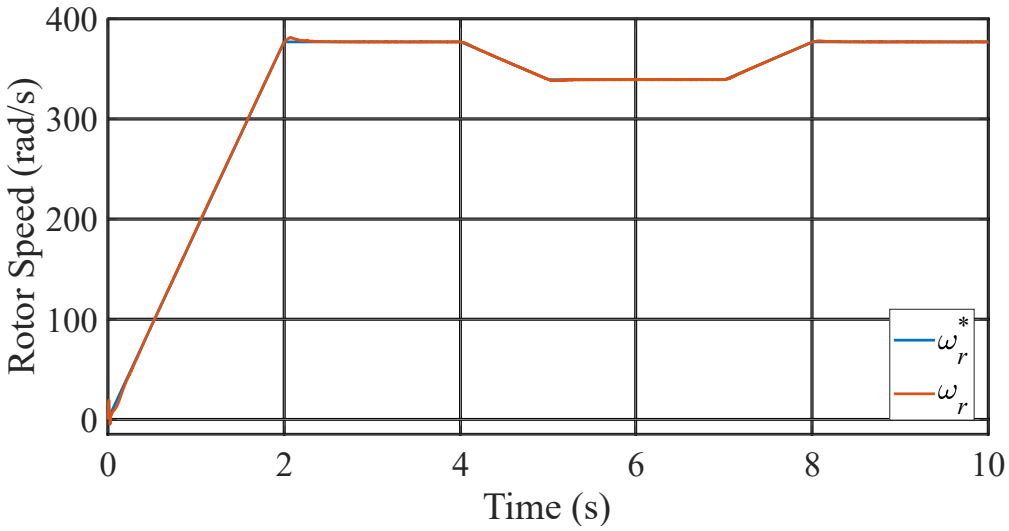

Figure 5.35: Rotor speed of RFSC.

The Figure 5.36 presents the zoom. It is possible to see that this control has the poorest MPPT performance with the highest settling time and highest overshoot which degrades the response.

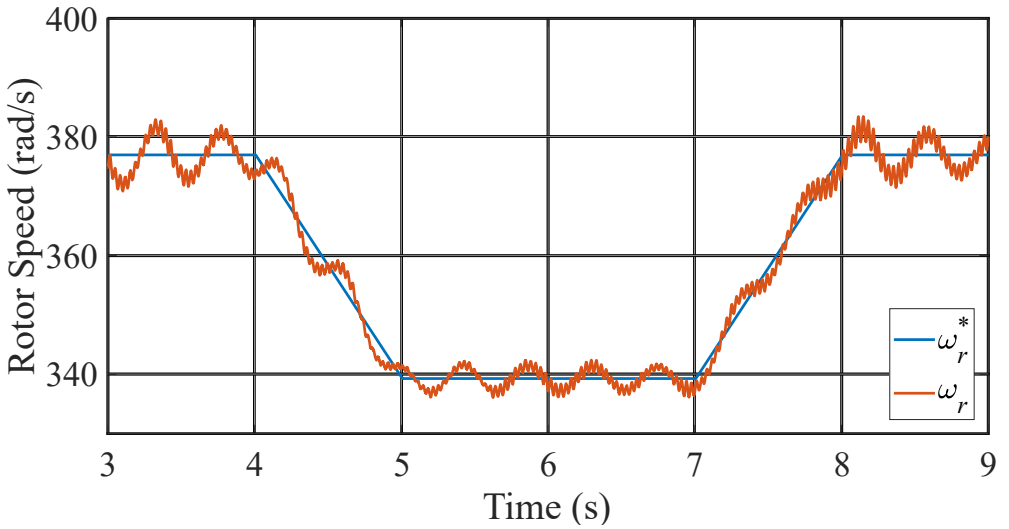

Figure 5.36: Zoom of rotor speed of RFSC.

The Figure 5.37 presents the control voltages of RFSC. It is far from the limit of a half of de DC link voltage of the 2L-VSC used in the back-to-back converter, but it presented high settling time which is not a desirable response.

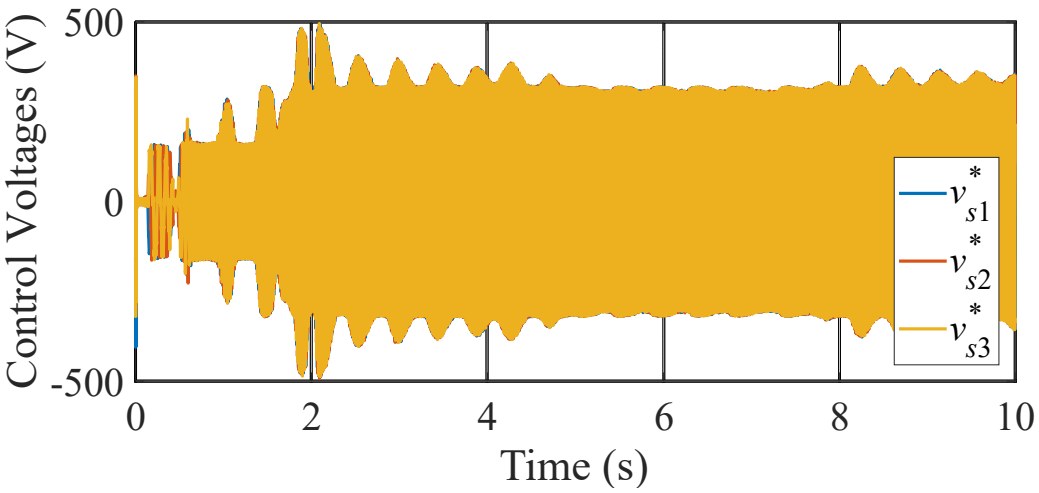

Figure 5.37: Control Voltages of RFSC.

The Figure 5.38 presents a zoom of the control voltages of RFSC. Here is possible to see that it presented a variation of the magnitude and it is not a desirable response since in this region there is no variation of the wind.

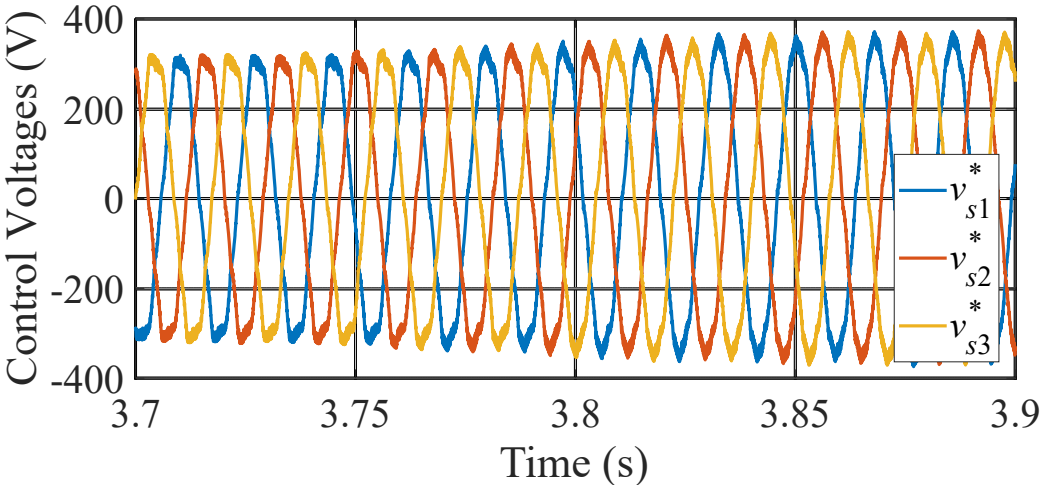

Figure 5.38: Zoom of Control Voltages of RFSC.

The Figure 5.39 presents the phase voltages of RFSC. As expected, the amplitude of the phase voltage is $2/3$ of the DC link voltage due to the 2L-VSC used in the back-to-back converter.

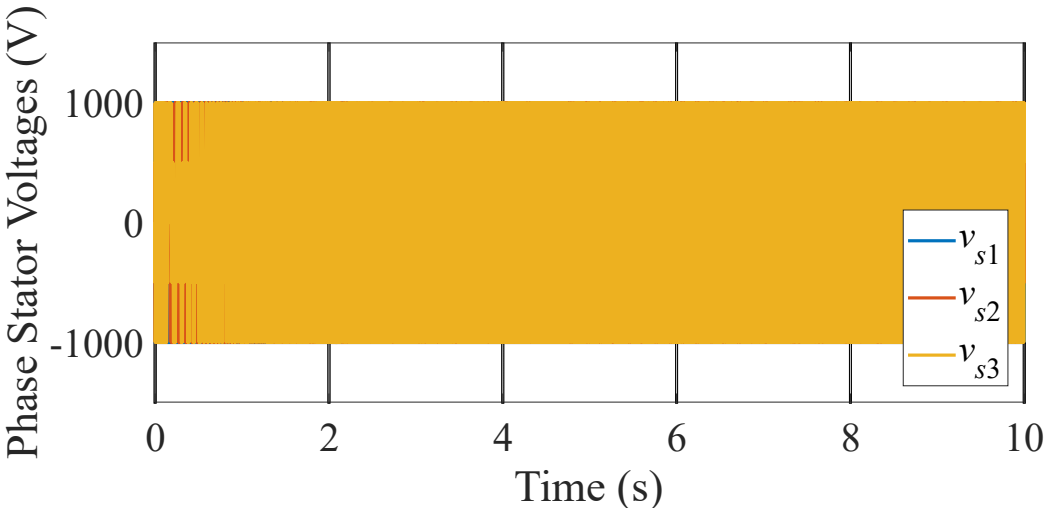

Figure 5.39: Phase Voltages of RFSC.

The Figure 5.40 presents a zoom of the phase voltages of RFSC. It presented an expected behavior since the sinusoidal wave is synthesized by the 5 operating points of the phase voltages of the 2L-VSC.

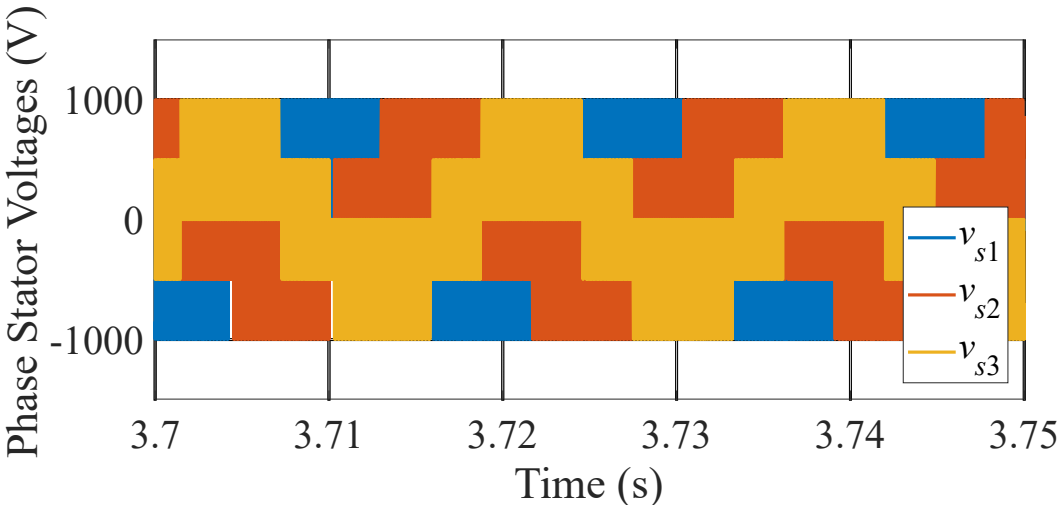

Figure 5.40: Zoom of Phase Voltages of RFSC.

5.4 DSFOC

The Table 5.7 presents the parameters used in this control strategy.

Table 5.7: Control parameters used in DSFOC

Parameter	K_p	K_i	K_d
Rotor speed	5.32	29.2	0
Stator flux	30	70	0
Direct axis stator current	10	526	0
Quadrature axis stator current	60	526	0

The Figure 5.41 presents the stator flux. The flux followed the reference, presenting an average ripple of 0.08 of magnitude and a desirable response. The reference has a fixed value and represents the magnitude of the stator flux, which should not vary significantly for a good operation of this control.

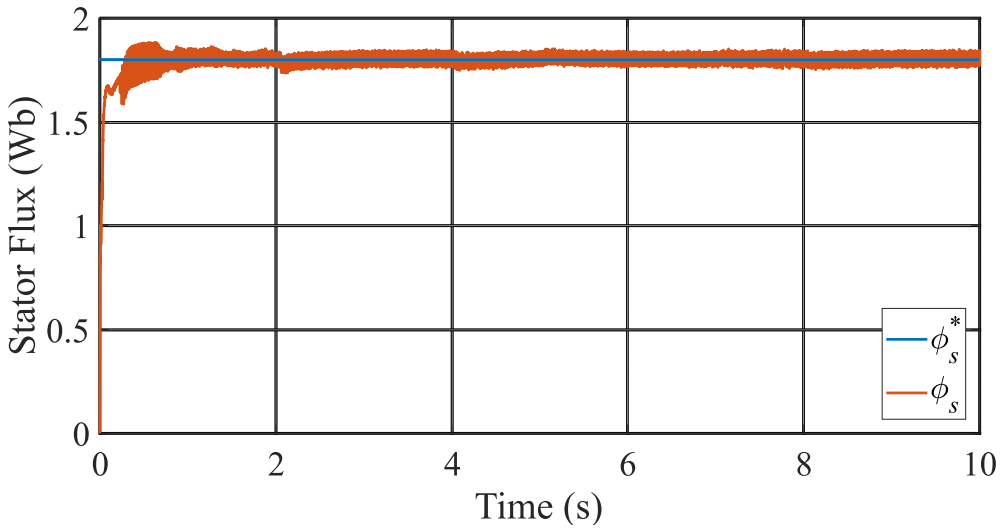

Figure 5.41: Stator flux of DSFOC.

The Figure 5.42 presents the stator currents. This control has the smallest inrush current whith a value of 10A, due to the inner current controllers, among the control strategies which is a desirable response.

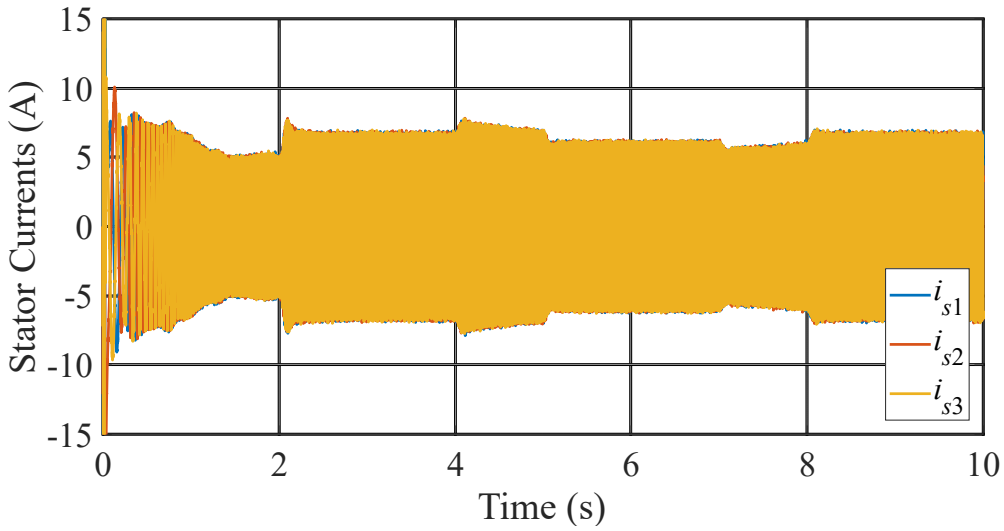

Figure 5.42: Stator currents of DSFOC.

The Figure 5.43 presents a zoom of stator currents. This result is expected and the closer to a perfect sine wave the better for the quality of the power delivered.

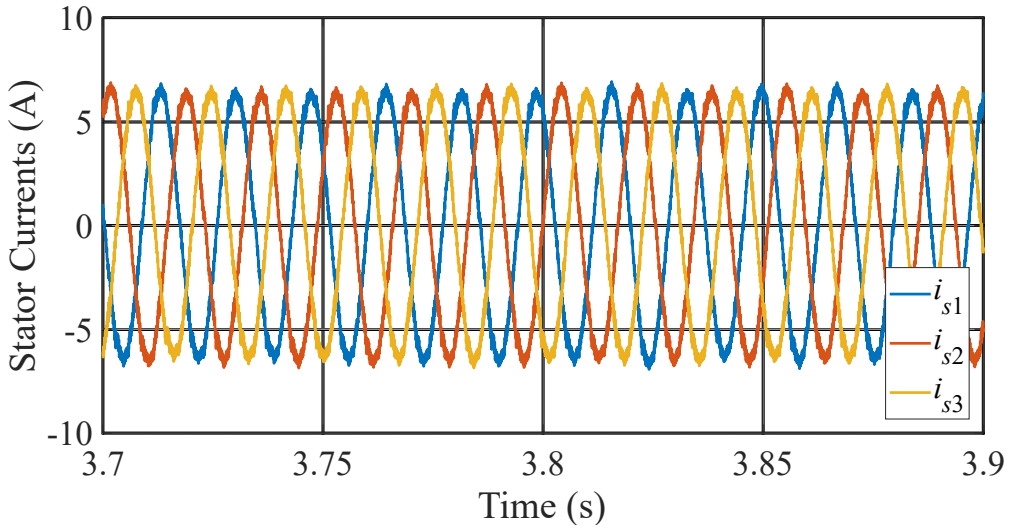

Figure 5.43: Zoom of stator currents of DSFOC.

The Figure 5.44 presents the frequency spectrum for this control. It presented the highest THD of all five control strategies and above the 5% recommended. It is not a desirable response, but it was expected since this control strategies the magnitude of the flux and the stator currents are controlled and a tiny control adjustment of these can affect the THD.

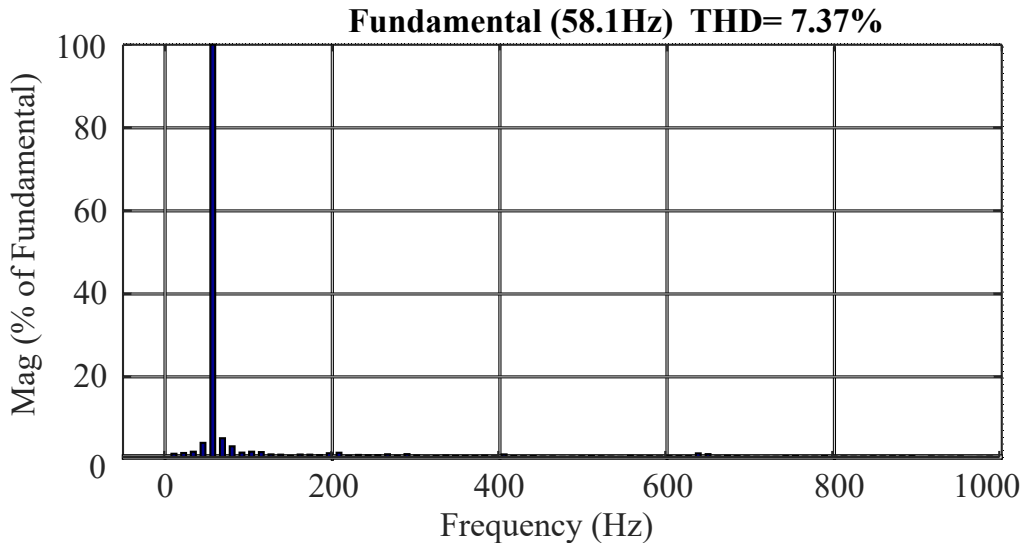

Figure 5.44: Frequency spectrum of stator current of DSFOC.

The Figure 5.45 presents the *d* component of stator current control. It has a high ripple of 2A and it was not a desirable response since it affects the THD.

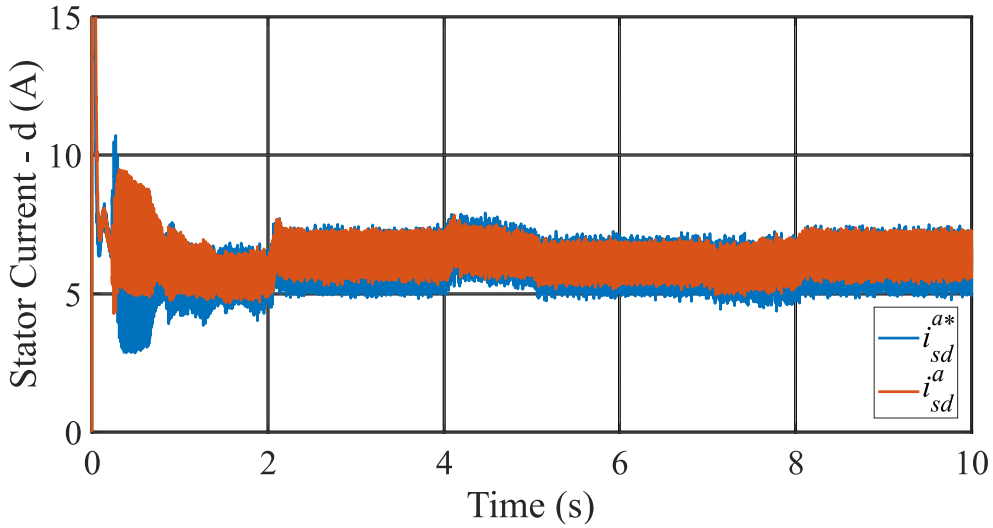

Figure 5.45: Direct component of stator current of DSFOC.

The Figure 5.46 presents the *q* component of stator current control. It has a high ripple of 1.45A and it was not a desirable response since it affects the THD.

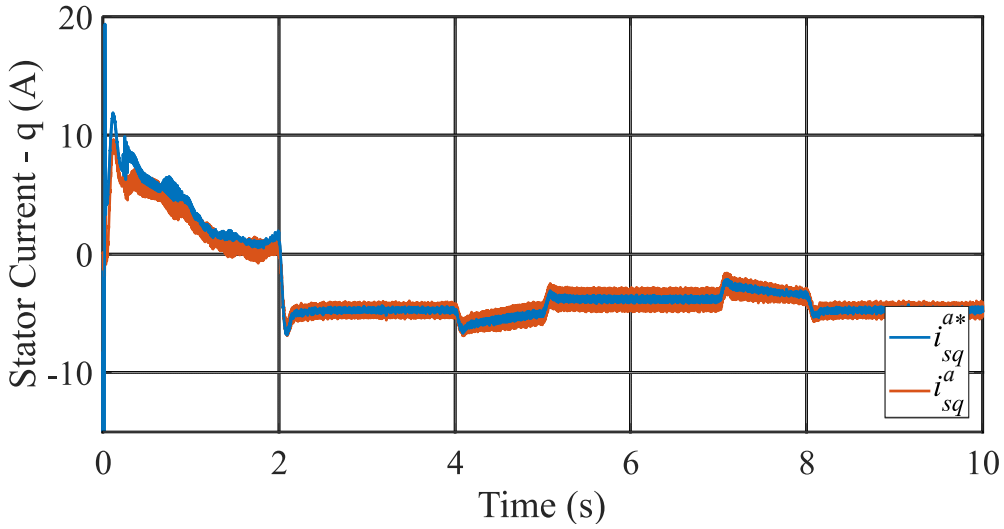

Figure 5.46: Quadrature component of stator of DSFOC.

The Figure 5.47 presents the rotor speed. It presents less oscillation at transient in comparison to SFSC and followed the reference as expected.

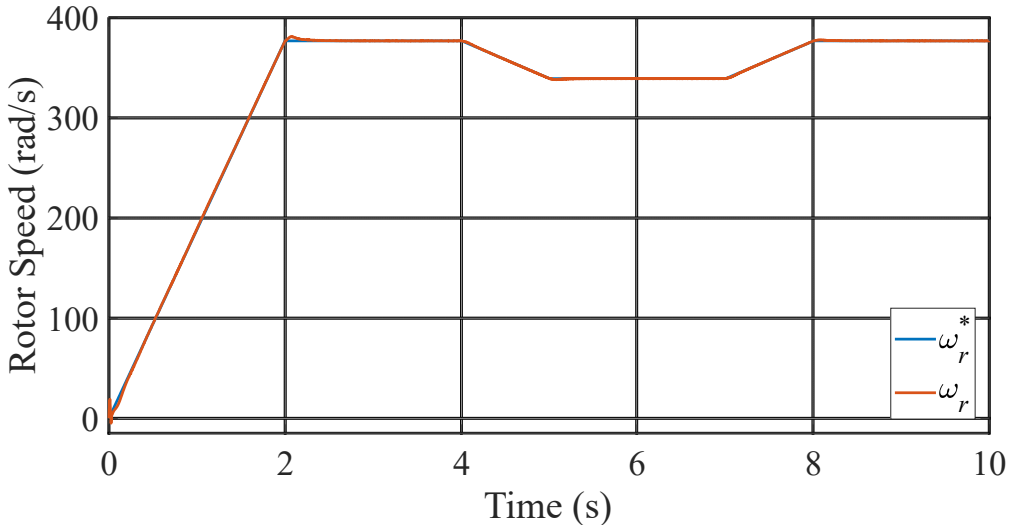

Figure 5.47: Rotor speed of DSFOC.

The Figure 5.48 presents the zoom. This control performs the MPPT with a small overshoot of 0.27%, with less oscillation at start-up in comparison to SFSC and DTC and a short settling time. It was one of the best dynamic response among the control strategies.

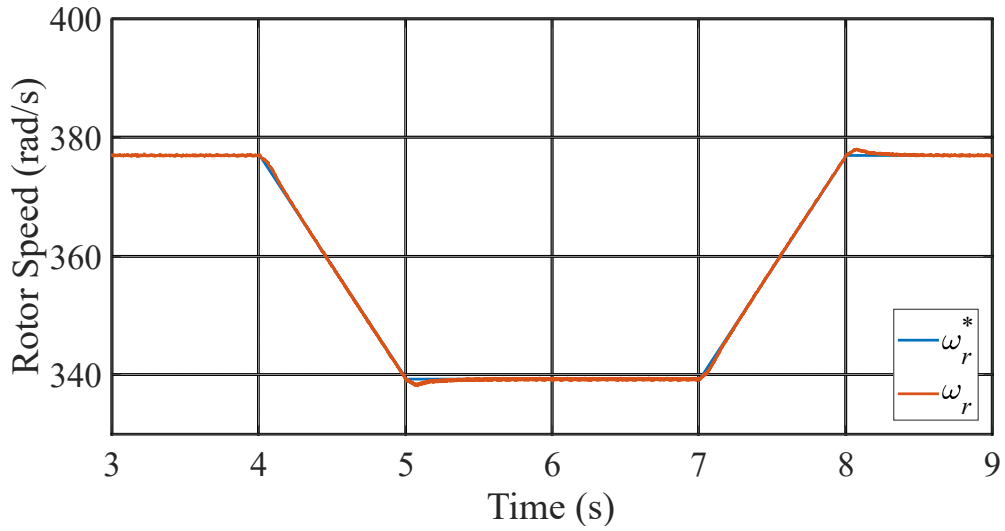

Figure 5.48: Zoom of rotor speed of DSFOC.

The Figure 5.49 presents the control voltages of DSFOC. It presented a desirable response since it is far from the limit of a half of de DC link voltage of the 2L-VSC used in the back-to-back converter.

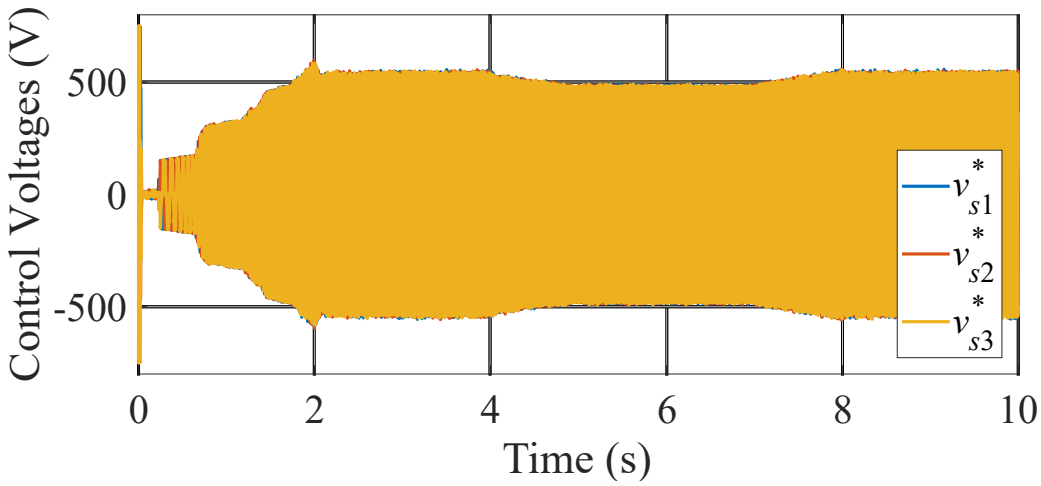

Figure 5.49: Control Voltages of DSFOC.

The Figure 5.50 presents a zoom of the control voltages of DSFOC. Here is possible to see that it presented the least ripple among the control strategies and it is a desirable response since these are control signals which are going to VSC1 to be synthesized.

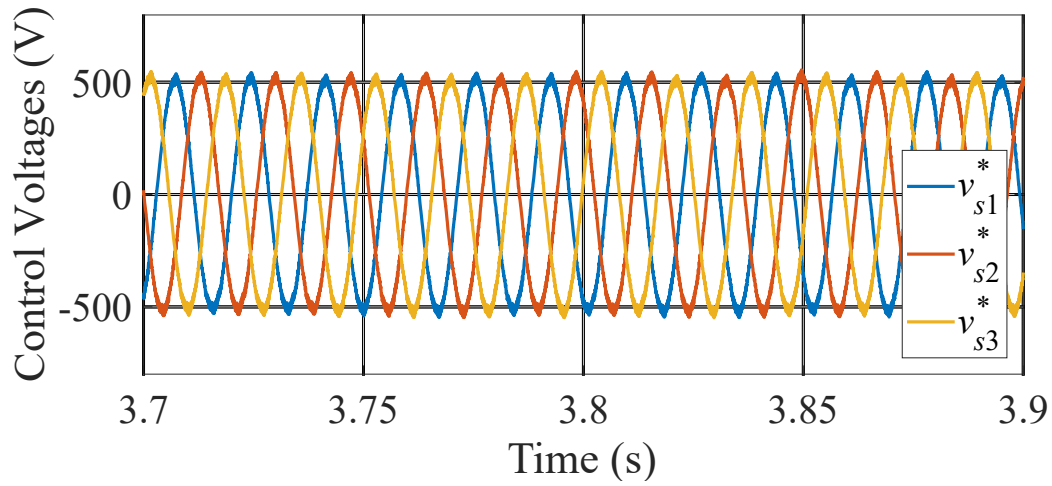

Figure 5.50: Zoom of Control Voltages of DSFOC.

The Figure 5.51 presents the phase voltages of DSFOC. As expected, the amplitude of the phase voltage is $2/3$ of the DC link voltage due to the 2L-VSC used in the back-to-back converter.

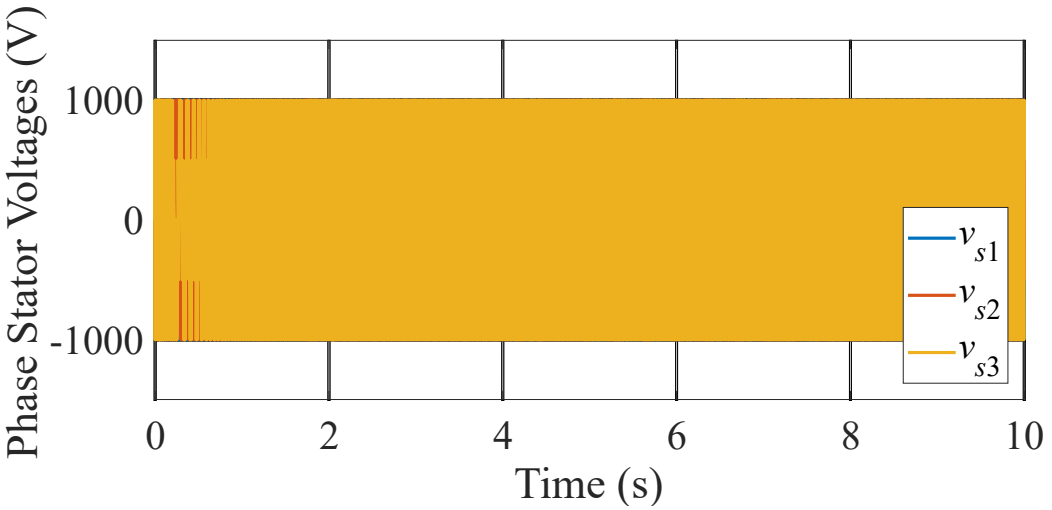

Figure 5.51: Phase Voltages of DSFOC.

The Figure 5.52 presents a zoom of the phase voltages of DSFOC. It presented an expected behavior since the sinusoidal wave is synthesized by the 5 operating points of the phase voltages of the 2L-VSC.

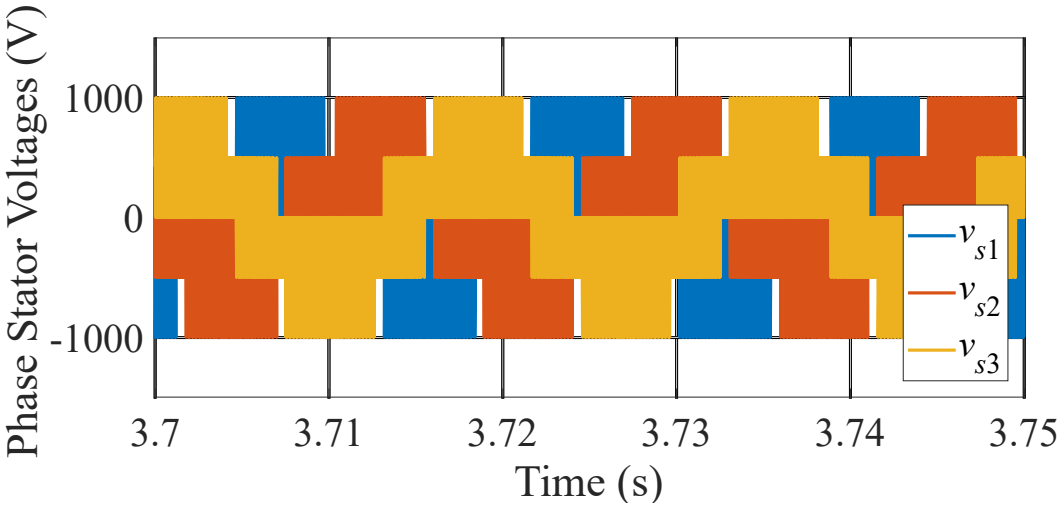

Figure 5.52: Zoom of Phase Voltages of DSFOC.

5.5 DRFOC

The Table 5.8 presents the parameters used in this control strategy.

Table 5.8: Control parameters used in DRFOC

Parameter	K_p	K_i	K_d
Rotor speed	5.32	29.2	0
Rotor flux	30	150	0
Direct axis stator current	500	550	0
Quadrature axis stator current	500	550	0

The Figure 5.53 presents the rotor flux control. It presented a desirable response and the flux followed the reference with a small ripple of 0.02 of magnitude. The reference has a fixed value and represents the magnitude of the rotor flux, which should not vary significantly for a good operation of this control.

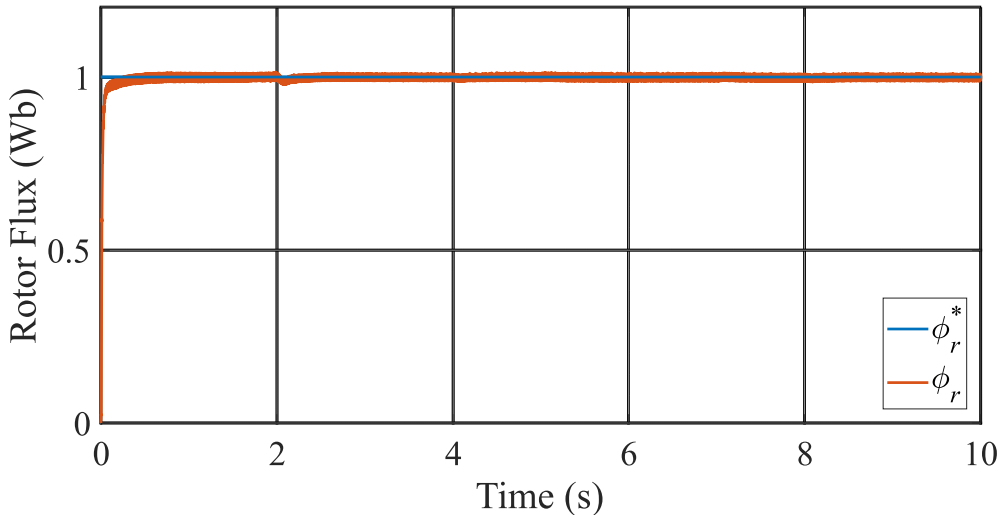

Figure 5.53: Rotor flux of DRFOC.

The Figure 5.54 presents the the stator currents. It has an inrush current of 13.3 A, which is one of the smallest inrush current and it presented a desirable response.

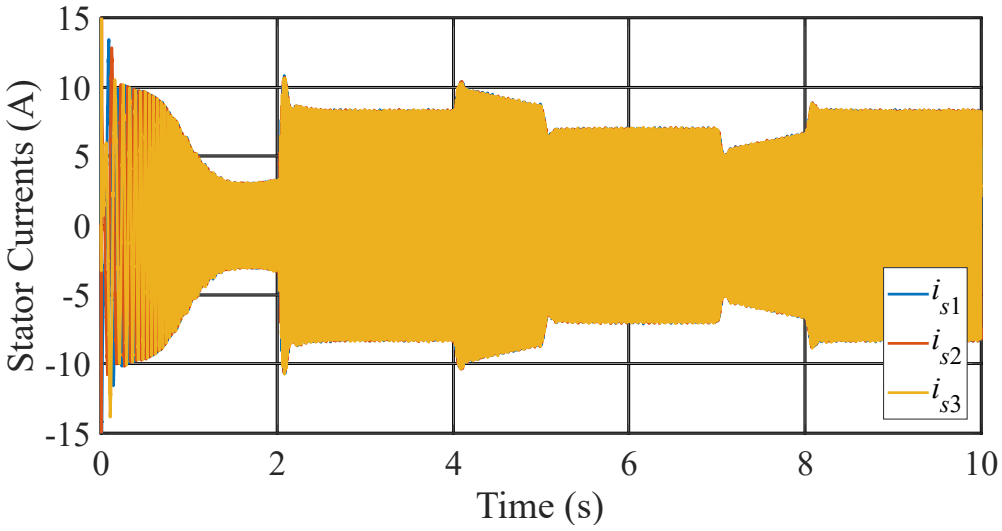

Figure 5.54: Stator currents of DRFOC.

The Figure 5.55 presents a zoom. This result is expected and the closer to a perfect sine wave the better for the quality of the power delivered.

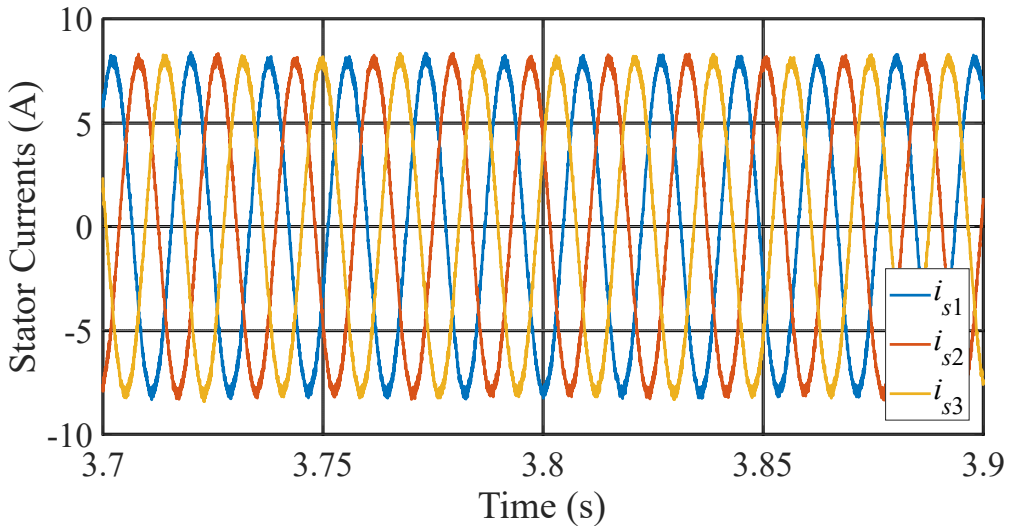

Figure 5.55: Zoom of stator currents of DRFOC.

The Figure 5.56 presents the frequency spectrum. It presented one of the smallest THD among the control strategies, below the 5% recommended and it was a desirable response.

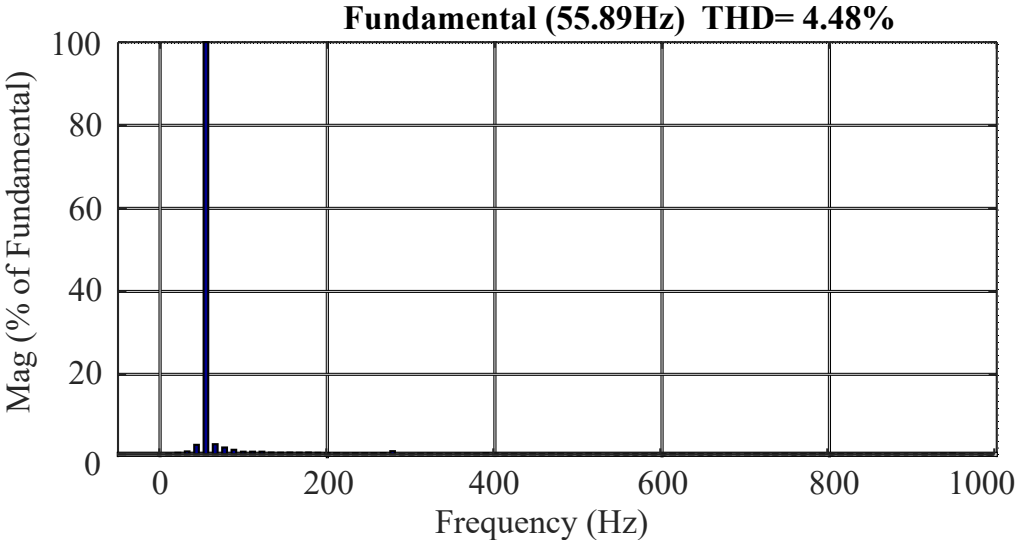

Figure 5.56: Frequency spectrum of stator current of DRFOC.

The Figure 5.57 presents the d component of stator current control. It presents a small ripple of 1A and it followed the reference during start-up and MPPT, producing a desirable response.

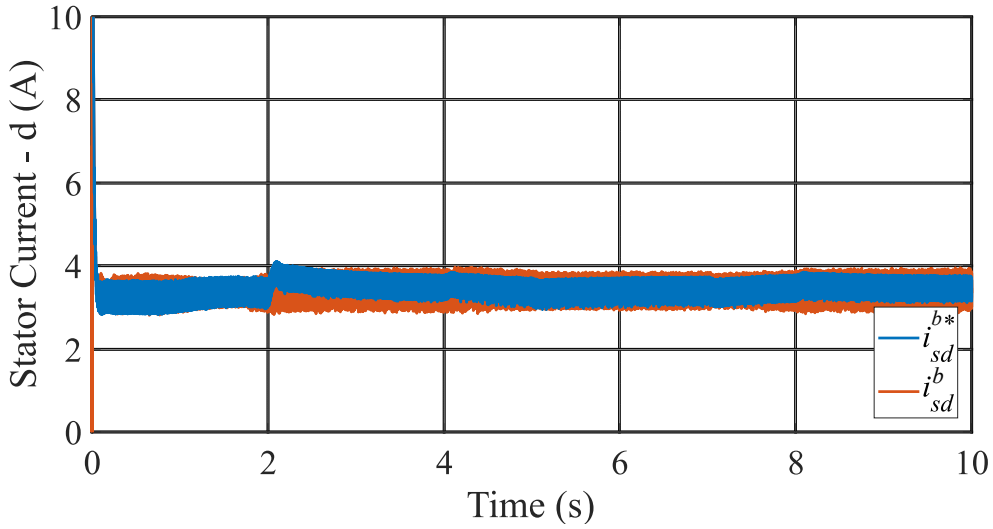

Figure 5.57: Direct component of stator current of DRFOC.

The Figure 5.58 presents the q component of stator current control. It presents a small ripple of 1.2A and it followed perfectly the reference during MPPT, producing a desirable response.

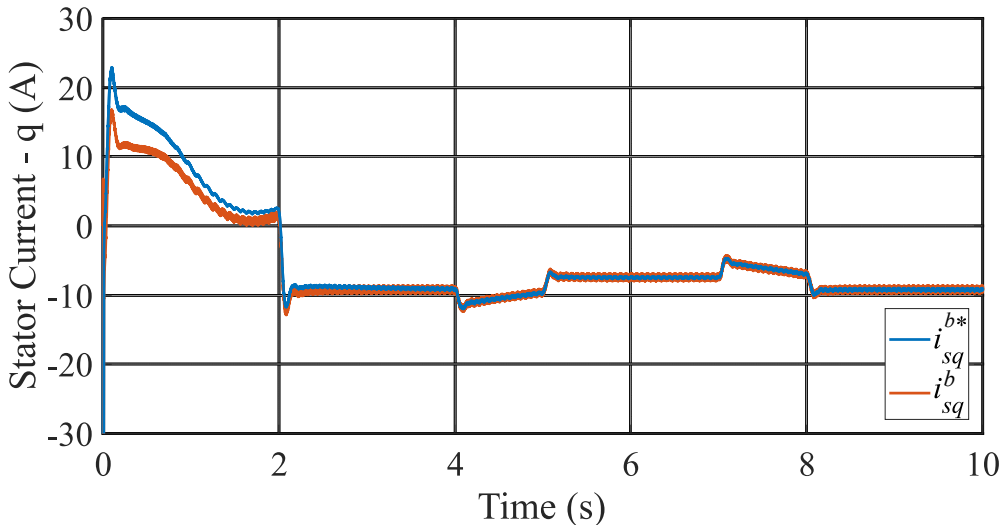

Figure 5.58: Quadrature component of stator current of DRFOC.

The Figure 5.59 presents the rotor speed. It performs similarly to DSFOC and followed the reference as expected.

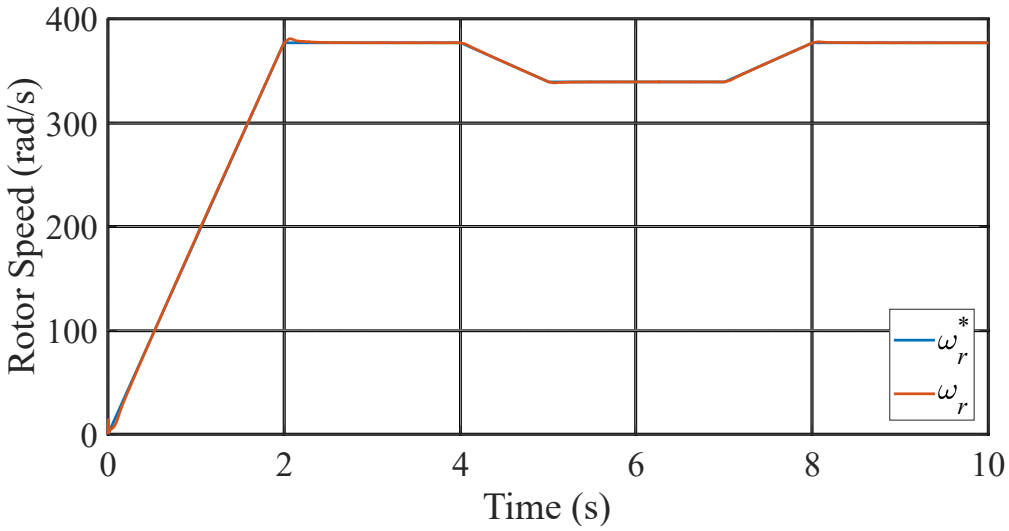

Figure 5.59: Rotor speed of DRFOC.

The Figure 5.60 presents the MPPT. It presented the smallest overshoot of 0.24% and a close response to the DSFOC, with less oscillation at start-up in comparison to SFSC and DTC and the shortest settling time. It was the best dynamic response among all control strategies.

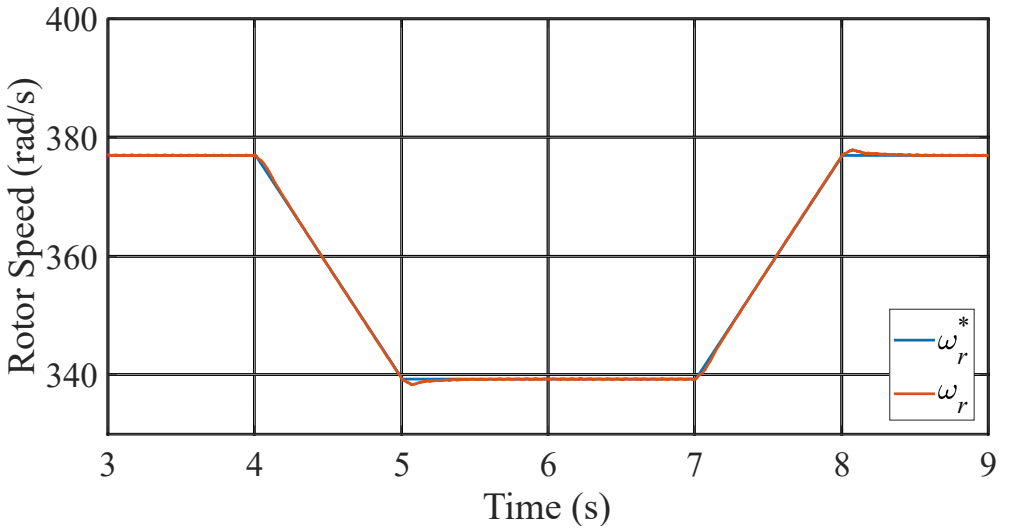

Figure 5.60: Zoom of rotor speed of DRFOC.

The Figure 5.61 presents the control voltages of DRFOC. It presented a desirable response since it is far from the limit of a half of de DC link voltage of the 2L-VSC used in the back-to-back converter.

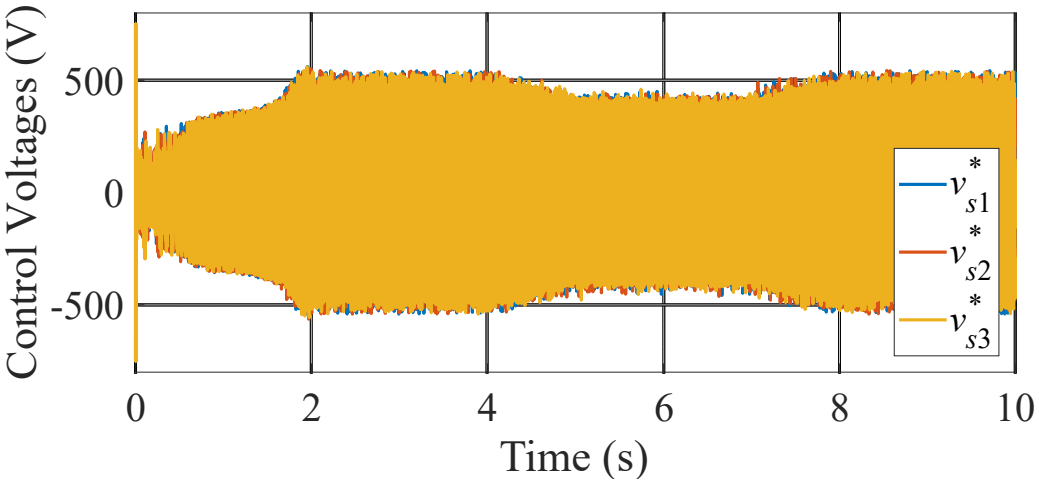

Figure 5.61: Control Voltages of DRFOC.

The Figure 5.62 presents a zoom the control voltages of DRFOC. Here is possible to see that it presented the highest ripple among the control strategies and it is not a desirable response since these are control signals which are going to VSC1 to be synthesized.

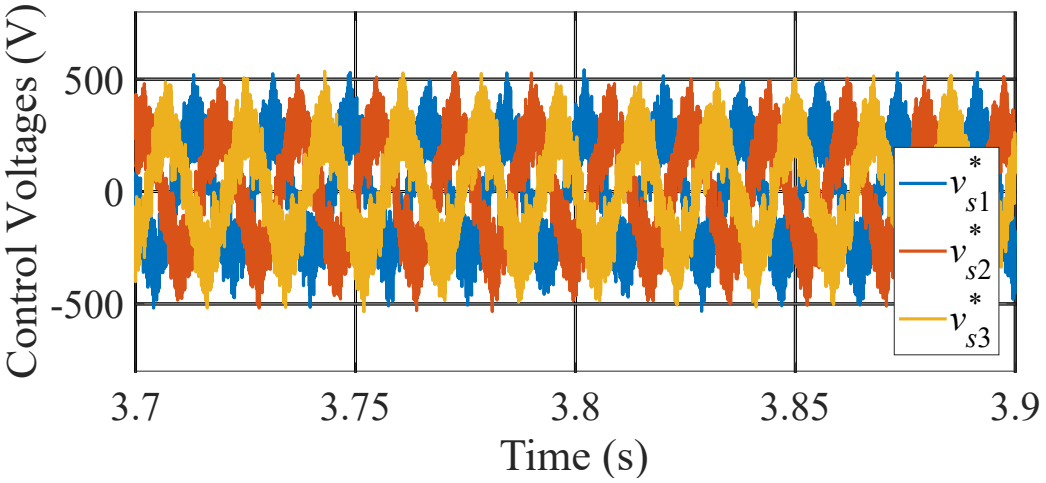

Figure 5.62: Zoom of Control Voltages of DRFOC.

The Figure 5.63 presents the phase voltages of DRFOC. As expected, the amplitude of the phase voltage is $2/3$ of the DC link voltage due to the 2L-VSC used in the back-to-back converter.

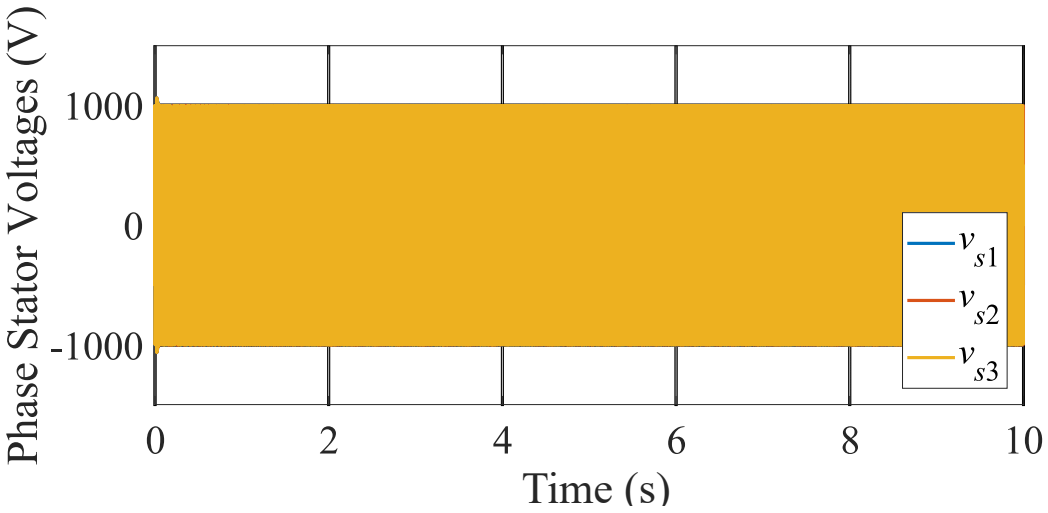

Figure 5.63: Phase Voltages of DRFOC.

The Figure 5.64 presents a zoom of the phase voltages of DRFOC. It presented an expected behavior since the sinusoidal wave is synthesized by the 5 operating points of the phase voltages of the 2L-VSC.

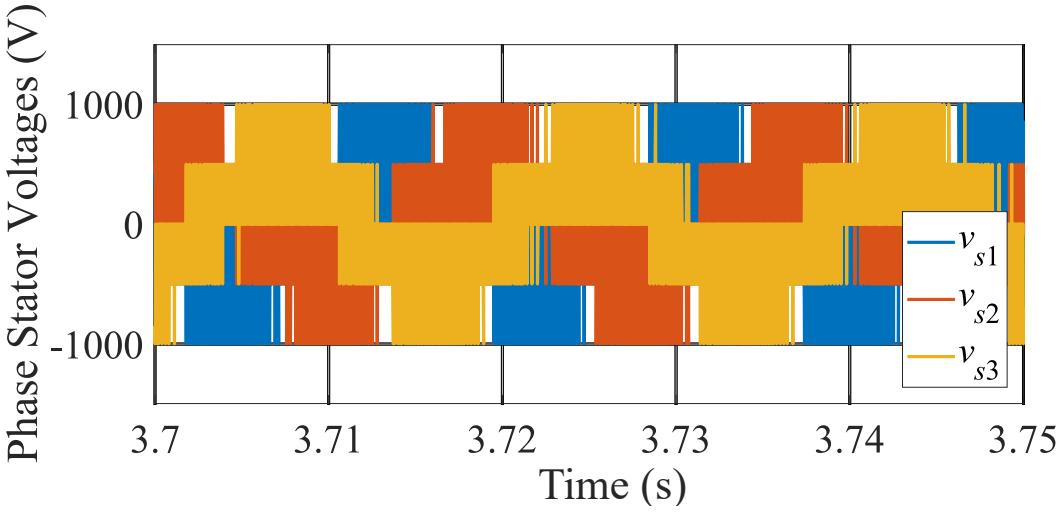

Figure 5.64: Zoom of Phase Voltages of DRFOC.

5.5.1 Summary of results analysis

The Table 5.9 presents a summary of results analysis. SFSC, DTC, RFSC, DSFOC and DRFOC were evaluated by the following parameter indexes: MPPT, THD, inrush current and dynamic response. The dynamic response is evaluated according to the settling time and percent overshoot and MPPT is evaluated according to the mean squared error.

Table 5.9: Summary of results analysis for SFSC, DTC, RFSC, DSFOC and DRFOC.

	Settling Time (s)	Percent Overshoot (%)	THD	Inrush Current (A)	Mean Squared Error of MPPT
Stator-Flux Slip Control (SFSC)	0.1944	0.53	3	14.3	0.3141
Direct Torque Control (DTC)	0.1392	0.37	5.98	28.5	0.1202
Rotor-Flux Slip Control (RFSC)	5.74	1.69	6.48	15.25	75.0723
Direc Stator-Field-Oriented Control (DSFOC)	0.08367	0.27	7.37	10	0.0561
Direc Rotor-Field-Oriented Control (DRFOC)	0	0.24	4.48	13.3	0.0434

SFSC does not present current controller, resulting in one of the highest inrush current, with more oscillated current magnitude and an oscillated rotor speed, but with the lowest total harmonic distortion. The presence of torque control in DTC provides a better dynamic response in comparison to SFSC, but it has the disadvantage of a higher inrush current and a higher THD. DSFOC has current control which provided the smallest inrush current among all control strategies and a more smoother magnitude current variation during maximum power point tracking in comparison to SFSC. It presented the highest total harmonic distortion and a smoother rotor speed variation at the start-up and at the maximum power point tracking in comparison to SFSC. It has similar rotor dynamic speed in comparison to DRFOC. DRFOC also has current control, but presented a higher magnitude current variation in comparison to DSFOC, the second smallest total harmonic distortion and a smooth rotor speed dynamic at the start-up and at the maximum power point tracking among all control strategies.

For all of this, the DRFOC is considered the best control strategy, since it presented the one of the best total harmonic distortion, the best dynamic performance at start-up and and the best maximum power point tracking, despite it presents a higher inrush-current in comparison to DSFOC. The second best control strategy is the DSFOC with a fast dynamic response, good MPPT error and low inrush current. The third best control strategy is the SFSC with its lowest total harmonic distortion, followed by the DTC with its fast dynamic response and lower MPPT error in comparison to SFSC. The least control strategy is the RFSC due to its high difficulty of control design and poor indexes performance.

5.6 Three-phase fault

The Figure 5.65 presents the voltage level at the coupling point with the grid. In it, a three-phase short-circuit has been applied for 100ms at 4s causing the voltage level to 0 as desired. The SFSC is used in this test.

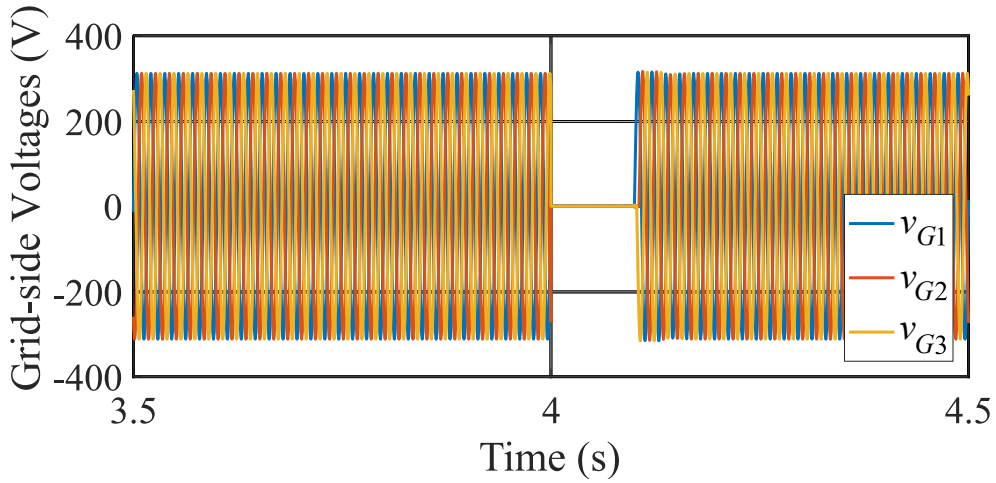

Figure 5.65: Voltage at the coupling point with the electrical grid.

The Figure 5.66 presents the response of the voltage level in the capacitor. It is possible to see that there is a change starting at 4s, but this variation is not significant and corresponds to approximately 4% of the nominal value.

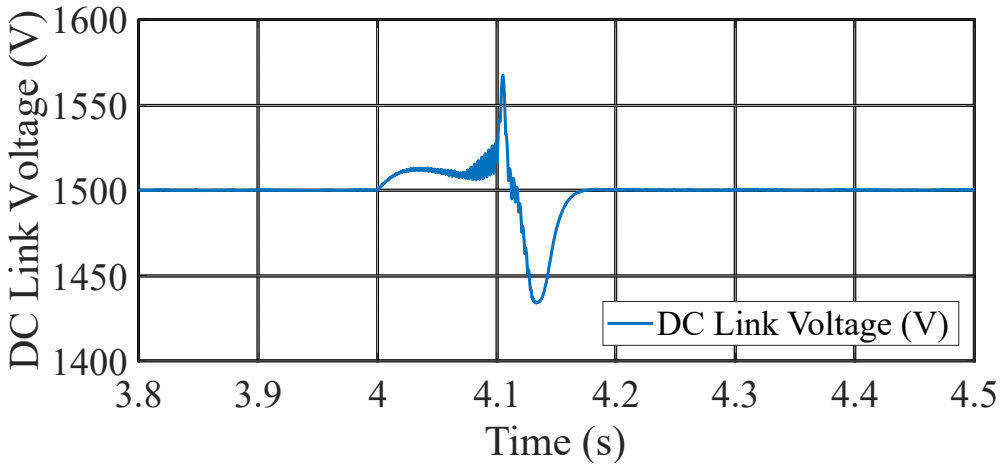

Figure 5.66: Voltage at the back-to-back capacitor.

The Figure 5.67 shows the response of the d-axis component of the stator flux from the machine-side control. It can be seen that the variation caused by the three-phase short-circuit at the voltage level of the capacitor does not produce any significant alteration in the d component of the d-axis stator flux control.

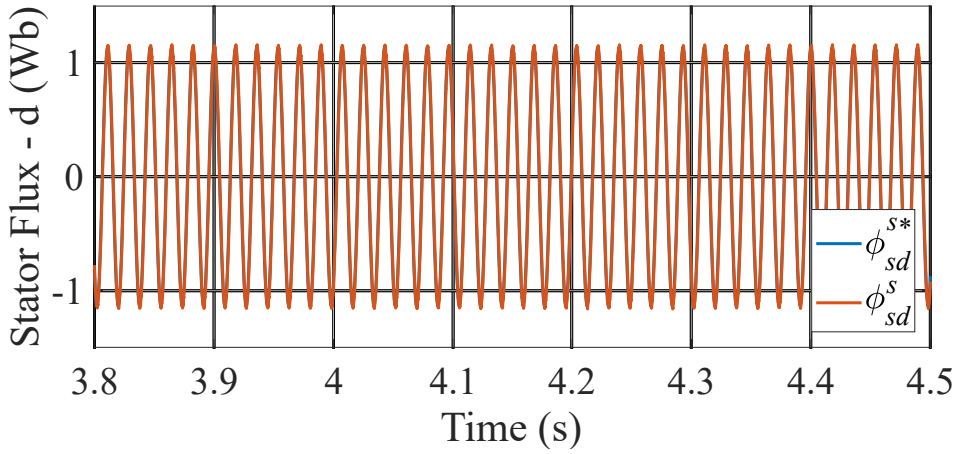

Figure 5.67: Component in the d-axis of the stator flux control.

The Figure 5.68 shows the response of the q-axis component of the stator flux of the machine-side control. It is also possible to verify, as in the previous case, that the variation caused by the three-phase short circuit in the voltage level capacitor does not produce any significant alteration in the control of the q component of the stator flux.

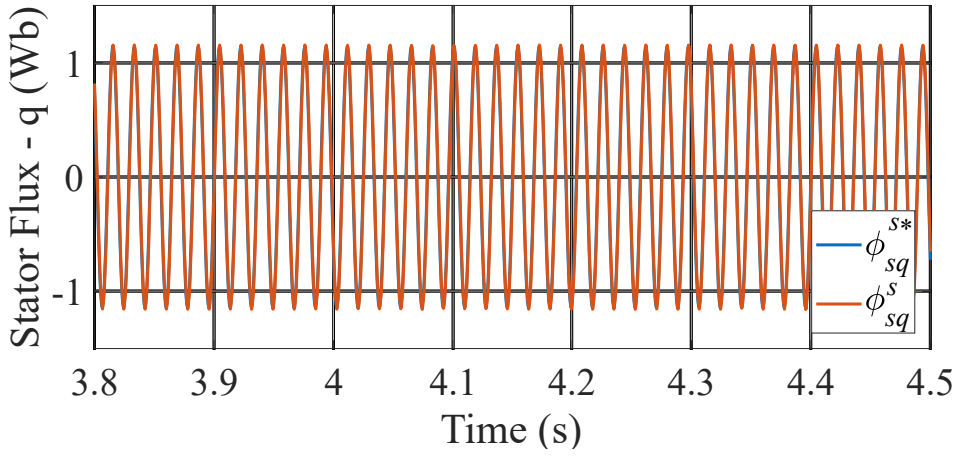

Figure 5.68: Component in the q-axis of the stator flux control.

The Figure 5.69 shows the response of the rotor speed of the machine-side control. It is also possible to verify, as in the previous case, that the variation caused by the three-phase short-circuit in the voltage level does not produce any significant alteration in the machine speed control.

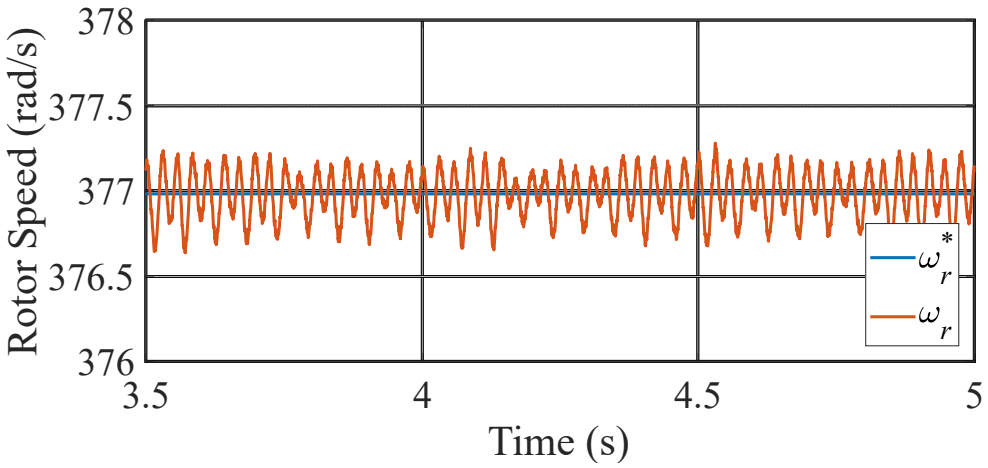

Figure 5.69: Rotor speed control.

5.7 Three-phase fault with 0.5mF capacitor

A test with a smaller capacitance of 0.5mF, instead of 2mF, was performed in order to verify the machine-side control response. Due to the smaller capacitance, the PI for voltage in the capacitor was readjusted to 0.4 for the P parameter and 80 for the I parameter.

The Figure 5.70 presents the response of the voltage level in the capacitor. During 4.1s to 4.2s a significant change can be seen from 674V to 2256V, but capacitor voltage control managed to stabilize it. It shows how harder is for the capacitor voltage control to manage a smaller capacitance for this circumstance.

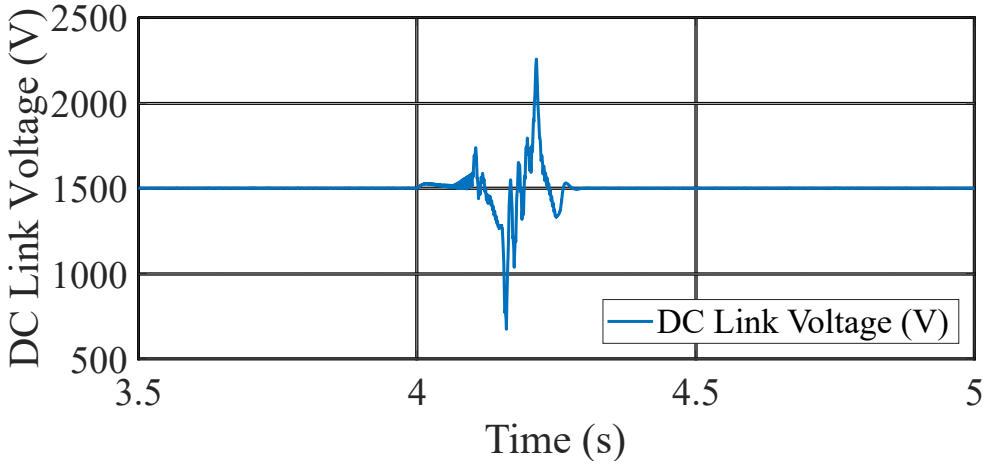

Figure 5.70: Voltage at the back-to-back capacitor.

The Figure 5.67 shows the response of the d-axis component of the stator flux from the machine-side control. It can be seen that the variation caused by the three-phase short-circuit at the voltage level of the capacitor does not produce any significant alteration in

the d component of the d-axis stator flux control, since the variation was fast enough and presented a mean value close to 1500V at the capacitor.

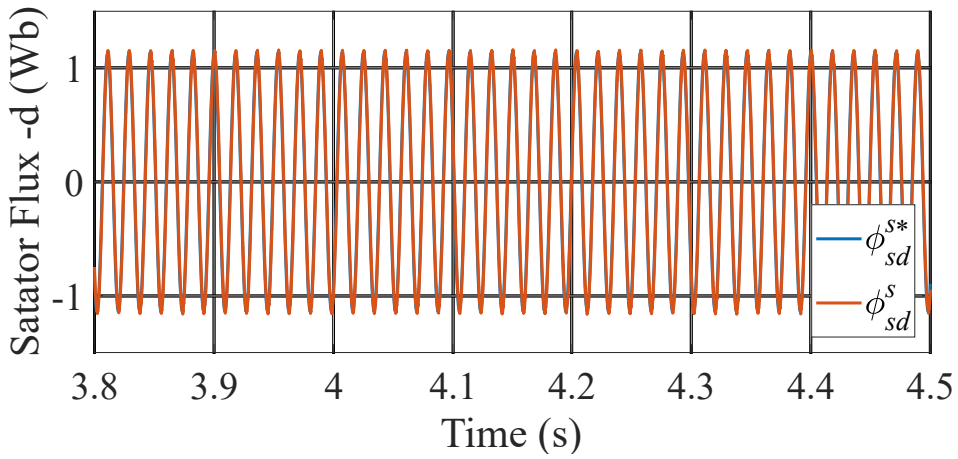

Figure 5.71: Component in the d-axis of the stator flux control.

The Figure 5.68 shows the response of the q-axis component of the stator flux of the machine-side control. It is also possible to verify, as in the previous case, that the variation caused by the three-phase short circuit in the voltage level capacitor does not produce any significant alteration in the control of the q component of the stator flux, since the variation was fast enough and presented a mean value close to 1500V at the capacitor.

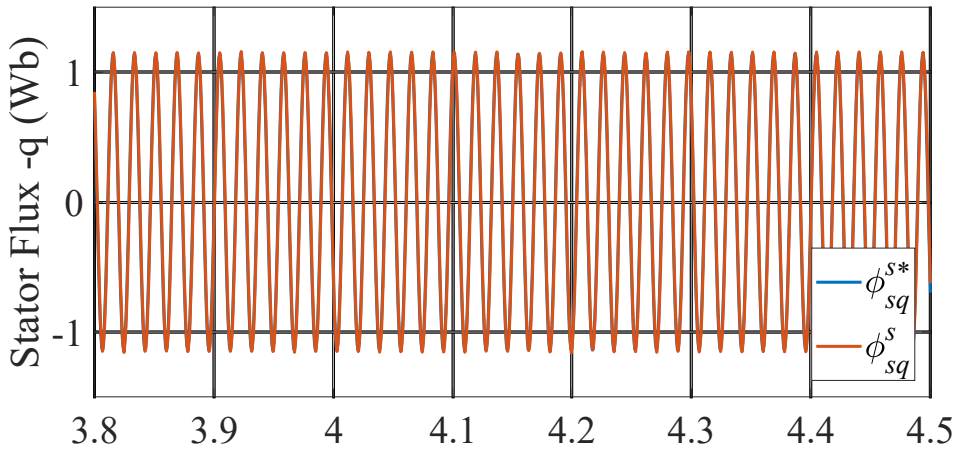

Figure 5.72: Component in the q-axis of the stator flux control.

The Figure 5.69 shows the response of the rotor speed of the machine-side control. It is possible to see that that the variation caused by the three-phase short-circuit in the voltage level produce a small variation of 0.25 rad/s in the machine speed control, but this was not enough to degrade the speed control which managed to stabilize the rotor speed.

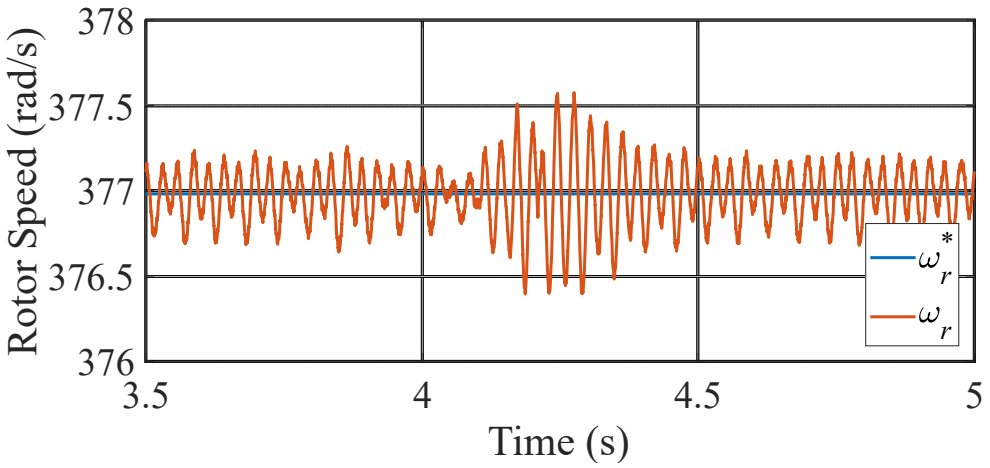

Figure 5.73: Rotor speed control.

The three-phase short-circuit tests at the coupling point were performed and the results obtained suggest that there is no performance loss for machine-side control for the three-phase short-circuit at the coupling point.

5.8 Load rejection

The Figure 5.74 shows the voltage level at the coupling point with the power grid. In it, a voltage rise of twice the nominal voltage (220Vrms) was applied for 100ms at 4s.

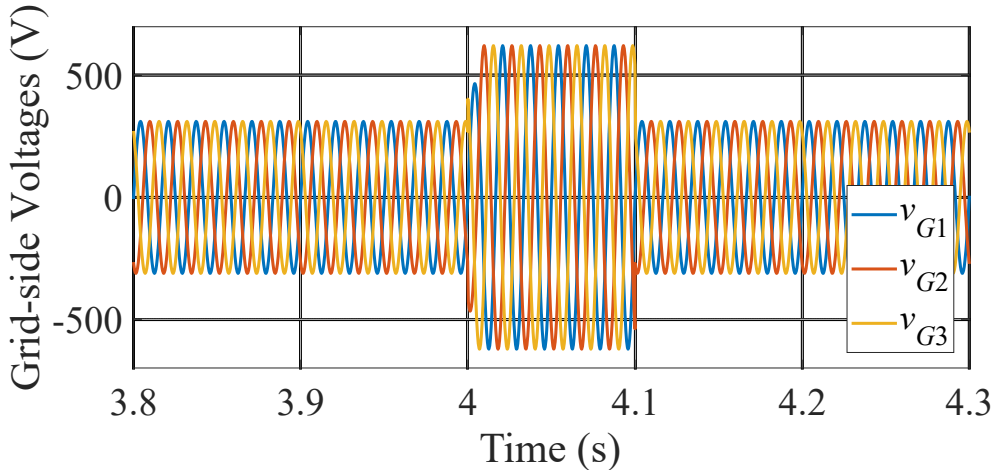

Figure 5.74: Voltage at the coupling point with the electrical grid.

The Figure 5.75 presents the response of the voltage level in the capacitor. It is possible to see that there is a change starting at 4s, but this variation is not significant and corresponds to approximately 0.1% of the nominal value.

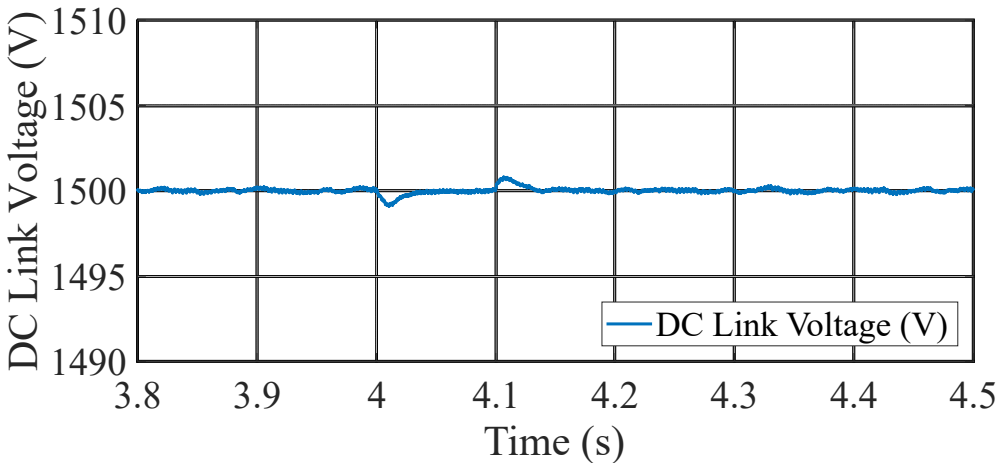

Figure 5.75: Voltage at the back-to-back capacitor.

The Figure 5.76 shows the response of the d-axis component of the stator flux from the machine-side control. It can be seen that the variation caused in the capacitor voltage does not produce any significant change in the d component of the stator flux control.

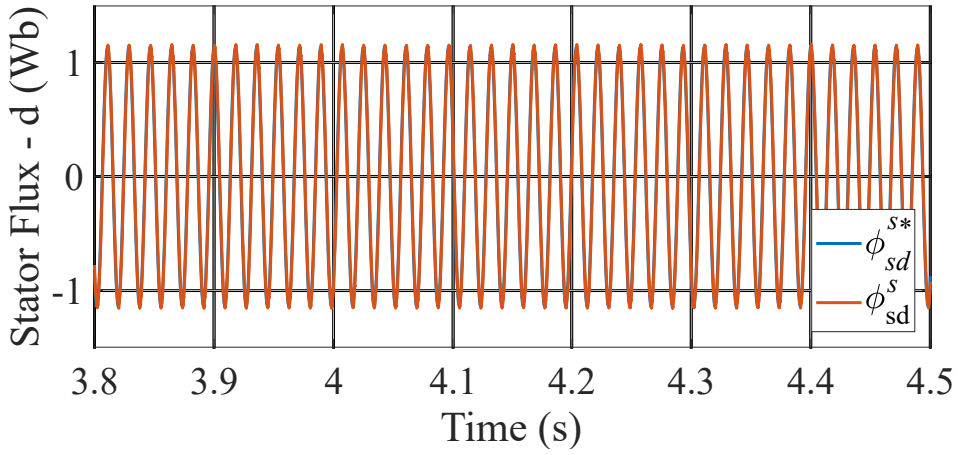

Figure 5.76: Component in the d-axis of the stator flux control.

The Figure 5.77 shows the response of the q-axis component of the stator flux from the machine-side control. It is also possible to verify, as in the previous case, that the variation caused in the capacitor voltage does not produce any significant change in the q component of the stator flux control.

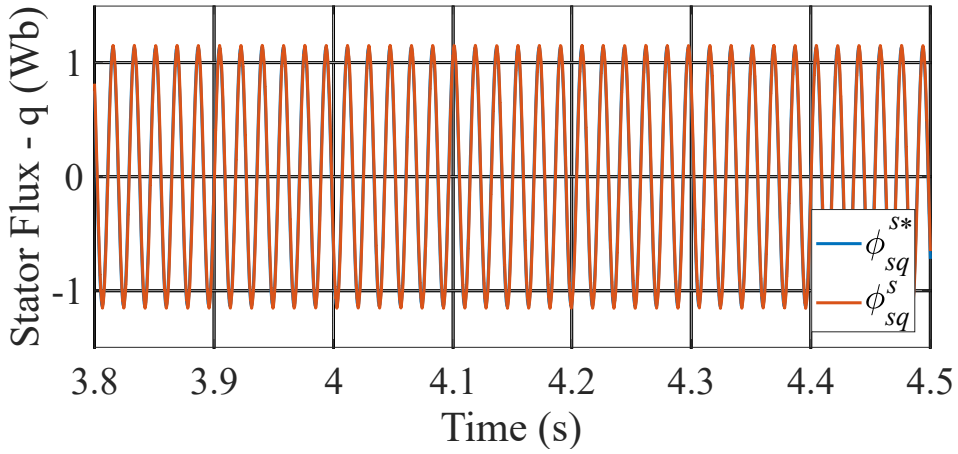

Figure 5.77: Component in the q-axis of the stator flux control.

The Figure 5.78 shows the response of the rotor speed of the machine-side control. It is also possible to verify, as in the previous case, that the variation caused in the capacitor voltage does not produce any significant change in the machine speed control.

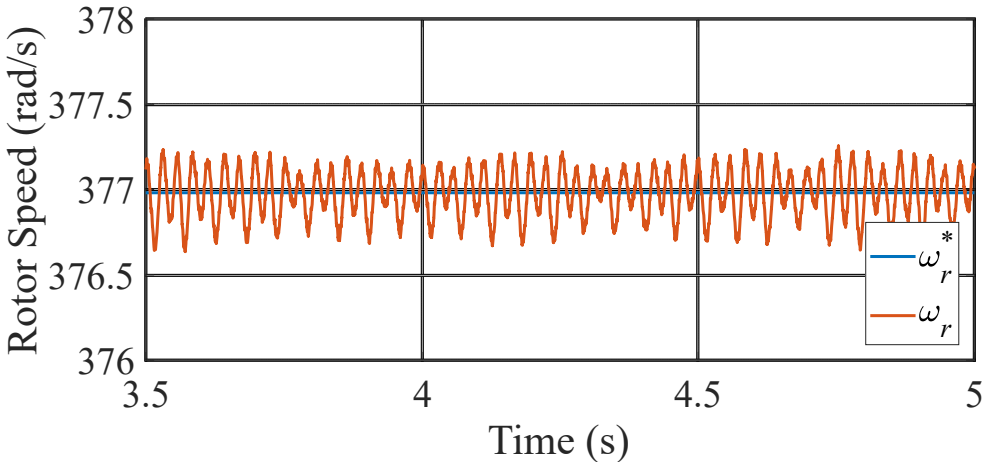

Figure 5.78: Rotor speed control.

The load rejection test at the coupling point was performed and the results obtained suggest that there is no performance loss for machine-side control for voltage rise cases at the coupling point.

The following chapter presents the conclusion of the five evaluated machine-side control strategies applied in SCIG-based WECS.

Chapter 6

Conclusion

In this work a squirrel cage induction generator is used in a wind energy conversion systems with Type IV configuration, combining the advantages of this generator with the full speed control. A comparison of five main machine-side control is carried out: stator-flux slip control, direct torque control, rotor-flux slip control, direct stator-field-oriented control and direct rotor-field-oriented control, taking into consideration the trade off for the main following performance indexes: maximum power point tracking, total harmonic distortion, inrush current and dynamic response.

Based on the implementation and the results, stator-flux slip control presents the most simple control scheme, with just two projects of controllers, since the flux controllers have the same transfer function. But, it does not present current controller, resulting in one of the highest inrush current, with more oscillated current magnitude and an oscillated rotor speed.

With similar control design, but with an increment of a torque control, direct torque control presented a better dynamic performance and a lower error at maximum power point tracking in comparison to stator-flux slip control, but it costed a higher total harmonic distortion and the highest inrush current.

Rotor-flux slip control has the highest difficulty of control design due to the high number of controllers and the high difficulty of fine tuning them. Therefore, it presented the poorest indexes performance, with the slowest dynamic response, the highest percent overshoot, the highest inrush current, the highest error at maximum power point tracking and one the highest total harmonic distortion.

Direct stator-field-oriented control has a more complex scheme in comparison to stator-flux slip control and direct torque control, since it has current control, but with the smallest inrush current among all control strategies and a more smooth magnitude current variation during maximum power point tracking. It presented the highest total harmonic distortion, a smooth rotor speed variation at the start-up, a fast dynamic response and a low error at the maximum power point tracking. It has similar rotor dynamic speed in comparison to direct rotor-field-oriented control.

Direct rotor-field-oriented control also has current control, but presented a higher magnitude current variation in comparison to direct stator-field-oriented control. It presented the one of the smallest total harmonic distortion and a smoother rotor speed dynamic at the start-up and at the maximum power point tracking among all control strategies.

For all of this, the direct rotor-field-oriented control is considered the best control

strategy, since it presented one of the best total harmonic distortion, the best dynamic performance at start-up and and the best error at maximum power point tracking, despite it presents a higher inrush-current in comparison to direct stator-field-oriented control. The second best control strategy is the direct stator-field-oriented control with a fast dynamic response, good maximum power point tracking error and low inrush current. The third best control strategy is the stator-flux slip control with its lowest total harmonic distortion, followed by the direct torque control with its fast dynamic response and lower maximum power point tracking error in comparison to stator-flux slip control. The least control strategy is the rotor-flux slip control due to its high difficulty of control design and poor indexes performance.

For the three-phase fault and the rejection of load, the results suggest that if the capacitor voltage is not affected, then the machine-side control is also not affected and no significant alteration is observed in the control variables.

6.1 Future Works

For future works, it is expected the following steps:

- Equipment set up.
- Experimental validation of a emulator of the system.
- Comparison to the simulated control strategies.
- Evaluate the best control strategy.

Chapter 7

Appendix

The appendix presents the models used in MATLAB/Simulink.

7.1 Turbine model

The model of the turbine is presented in Figure 7.1. It was made by the equations (4.1) to (4.11).

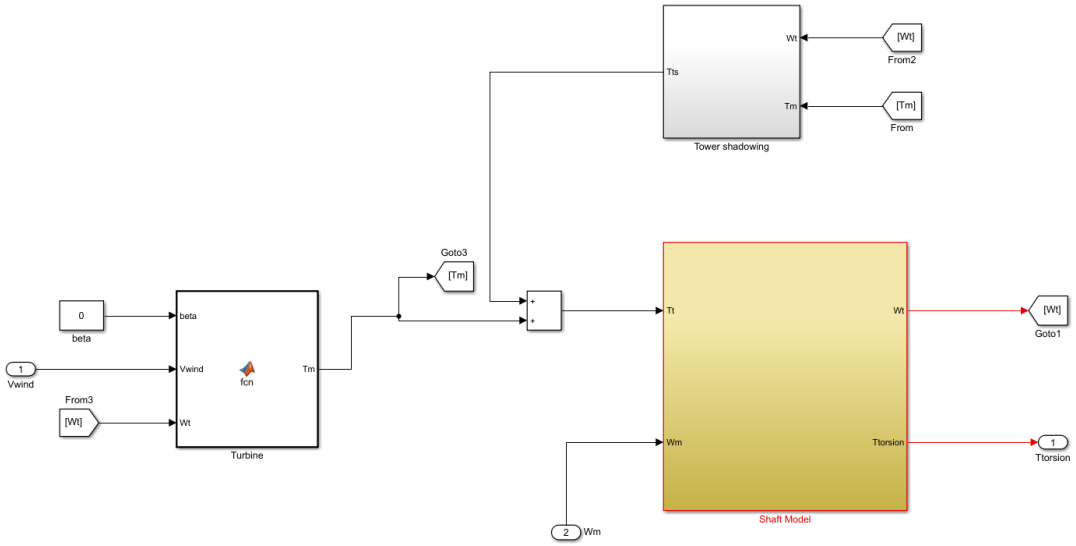

Figure 7.1: Turbine model

The mechanical torque which is given by the equation (4.1) is presented in Figure 7.2:

```
function Tm = fcn(beta,Vwind,Wt)
R=2.1;
ro=1.21;
lamb=(Wt/Vwind) * R;
lambi=1/((1/(lamb+0.008*beta)) - (0.035/((beta^3)+1)));
Cp=0.5*( (116/lambi) - 0.4*beta -5 )*exp(-21/lambi);
Tm=0.5*ro*pi*(R^3)*(Cp/lamb)*(Vwind^2);
```

Figure 7.2: Mechanical torque

The tower shadowing model, from equation (4.5), is presented in Figure 7.3:

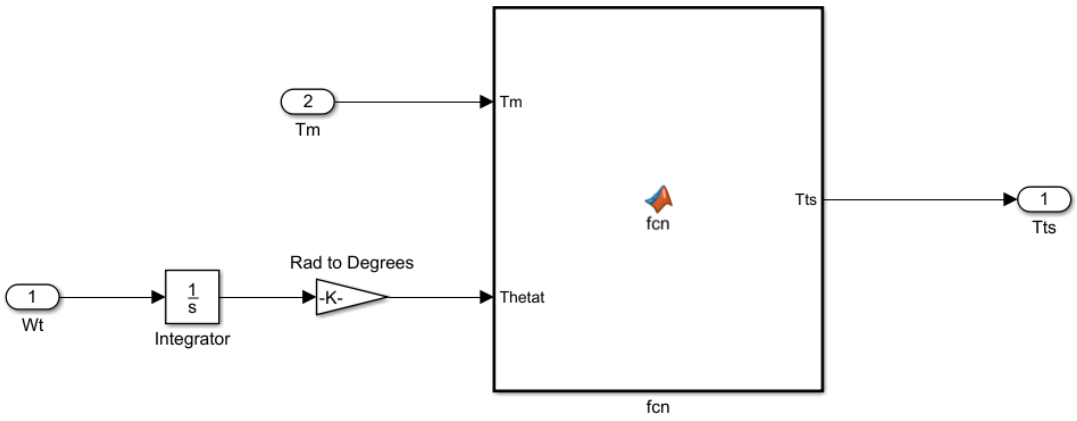

Figure 7.3: Tower shadowing

The *FPOS* equation, from equation (4.5), is presented in Figure 7.4:

```
function Tts = fcn(Tm,Thetat)
Kts=0.2;
alpha=30;
alpha2=alpha/2;
%%%%%FPOS
while Thetat>360
    Thetat=Thetat-360;
end
if (Thetat> 120) & (Thetat<=240)
       Thetat=Thetat-120;
elseif (Thetat> 240) & (Thetat<=360)
       Thetat=Thetat-240;
end
if (Thetat<= alpha2)
       FPOS=((-180*Thetat)/( (alpha2) )) + 180;
elseif (Thetat > 120-alpha2)

       FPOS=(180*Thetat/alpha2)-(120*180/alpha2)+180;
else
       FPOS=0;
end
Tts=Kts*( 0.5*cosd(FPOS) - 0.5)*Tm;
```

Figure 7.4: *FPOS* function

The coupling of the turbine with the SCIG, from equation (4.9)-(4.11), is presented in Figure 7.5:

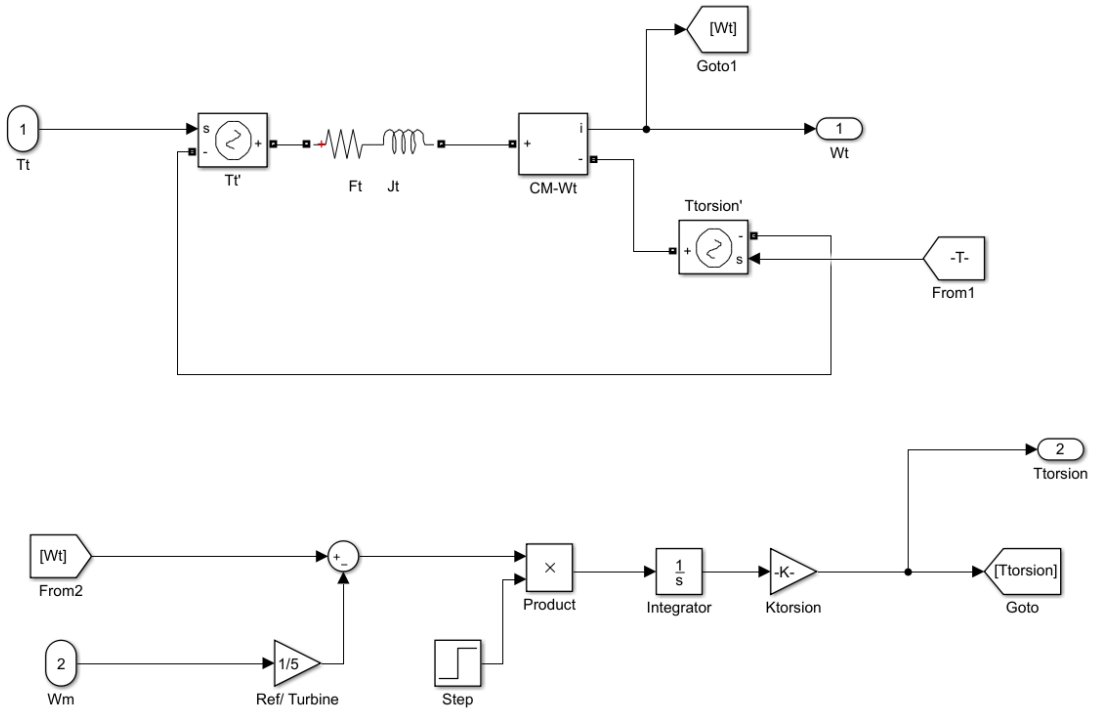

Figure 7.5: Shaft model

7.2 SCIG model

The fluxes and the electromagnetic torque, from equations (4.12), (4.13) and (4.16), are presented in Figure 7.6:

```
function [lambs1,lambs2,lambs3,lambr1,lambr2,lambr3,te] = fcn(is1,is2,is3,ir1,ir2,ir3,thtr)
P=2;
Ls=0.214067;
Lr=Ls;
Ms=-Ls*0.5;
Mr=Ms;
Msr=0.1989;
is123 = [is1; is2; is3];
ir123 = [ir1; ir2; ir3];
lambs1=Ls*is1 + Ms*is2 + Ms*is3 + Msr*ir1*cos(thtr) + Msr*ir2*cos(thtr + (2*pi)/3) + Msr*ir3*cos(thtr + (4*pi)/3);
lambs2=Ls*is2 + Ms*is1 + Ms*is3 + Msr*ir2*cos(thtr) + Msr*ir1*cos(thtr + (4*pi)/3) + Msr*ir3*cos(thtr + (2*pi)/3);
lambs3=Ls*is3 + Ms*is1 + Ms*is2 + Msr*ir3*cos(thtr) + Msr*ir1*cos(thtr + (2*pi)/3) + Msr*ir2*cos(thtr + (4*pi)/3);
lambr1=Lr*ir1 + Mr*ir2 + Mr*ir3 + Msr*is1*cos(thtr) + Msr*is3*cos(thtr + (2*pi)/3) + Msr*is2*cos(thtr + (4*pi)/3);
lambr2=Lr*ir2 + Mr*ir1 + Mr*ir3 + Msr*is2*cos(thtr) + Msr*is1*cos(thtr + (2*pi)/3) + Msr*is3*cos(thtr + (4*pi)/3);
lambr3=Lr*ir3 + Mr*ir1 + Mr*ir2 + Msr*is3*cos(thtr) + Msr*is2*cos(thtr + (2*pi)/3) + Msr*is1*cos(thtr + (4*pi)/3);
dervLsr = [ -Msr*sin(thtr)            -Msr*sin(thtr + (2*pi)/3)     Msr*sin(thtr + pi/3)
             Msr*sin(thtr + pi/3)     -Msr*sin(thtr)               -Msr*sin(thtr + (2*pi)/3)
            -Msr*sin(thtr + (2*pi)/3)  Msr*sin(thtr + pi/3)     -Msr*sin(thtr)];
te=(P)*is123'*dervLsr*ir123;
```

Figure 7.6: Fluxes and torque equations

The stator and the rotor, from equations (4.14) and (4.15) are presented in Figure 7.7:

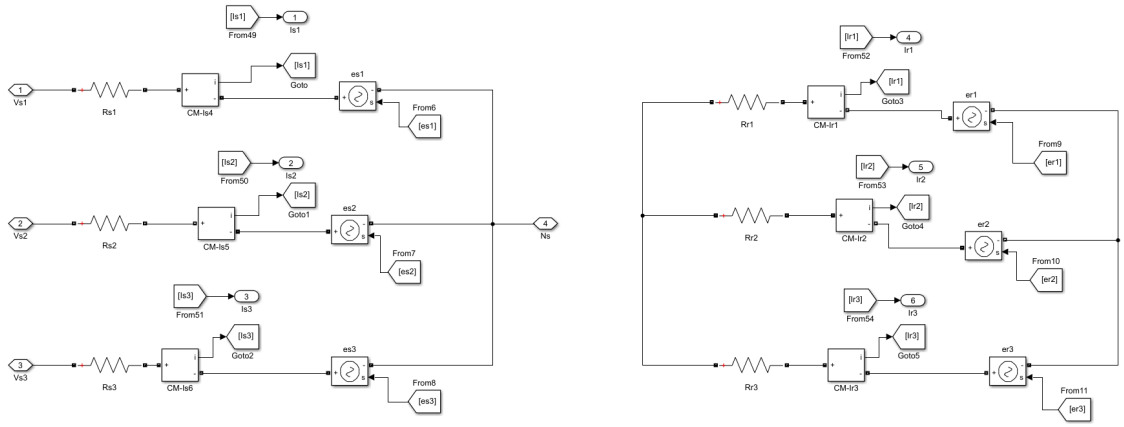

Figure 7.7: Stator and rotor of the SCIG

The currents and the mechanical model, from equations (4.10), (4.14) and (4.15) are presented in Figure 7.8:

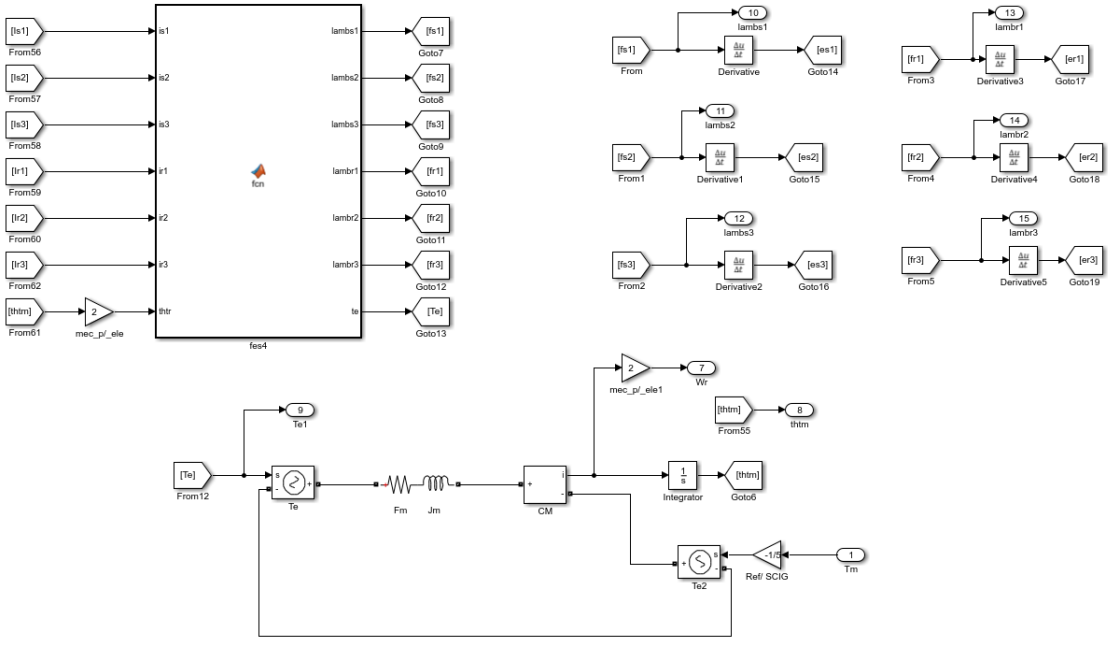

Figure 7.8: Currents and mechanical model

7.3 Grid-side model

The Grid-side control is presented in Figure 7.9:

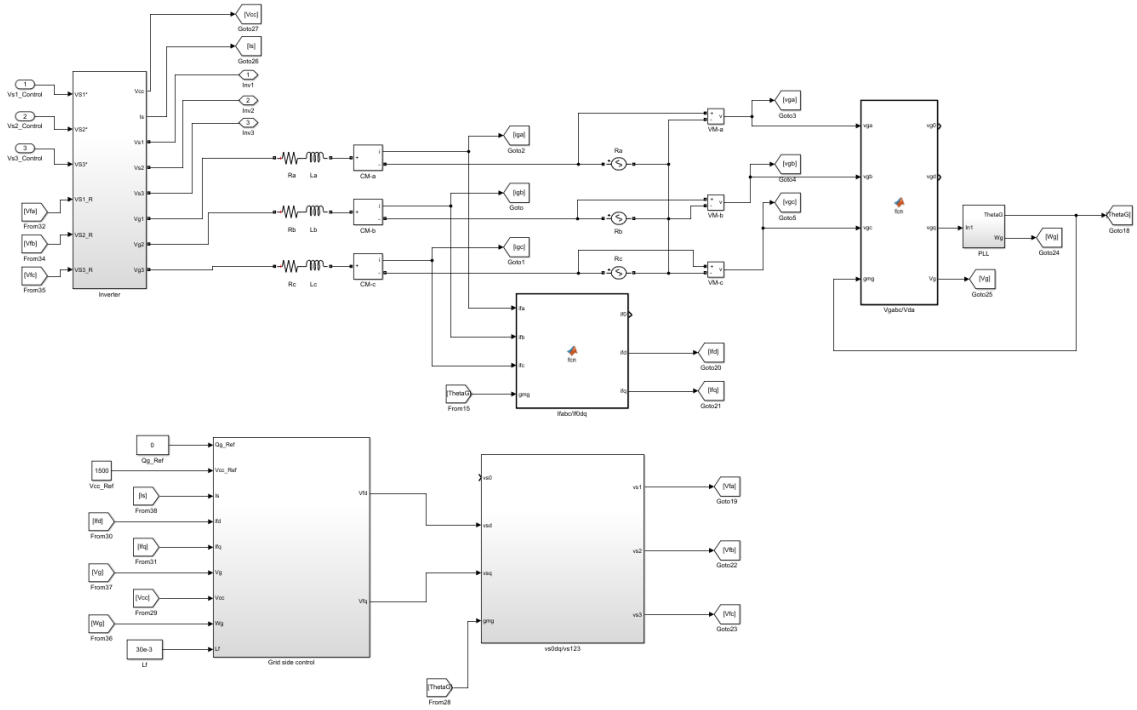

Figure 7.9: Grid-side model

The back-to-back converter in Figure 7.10:

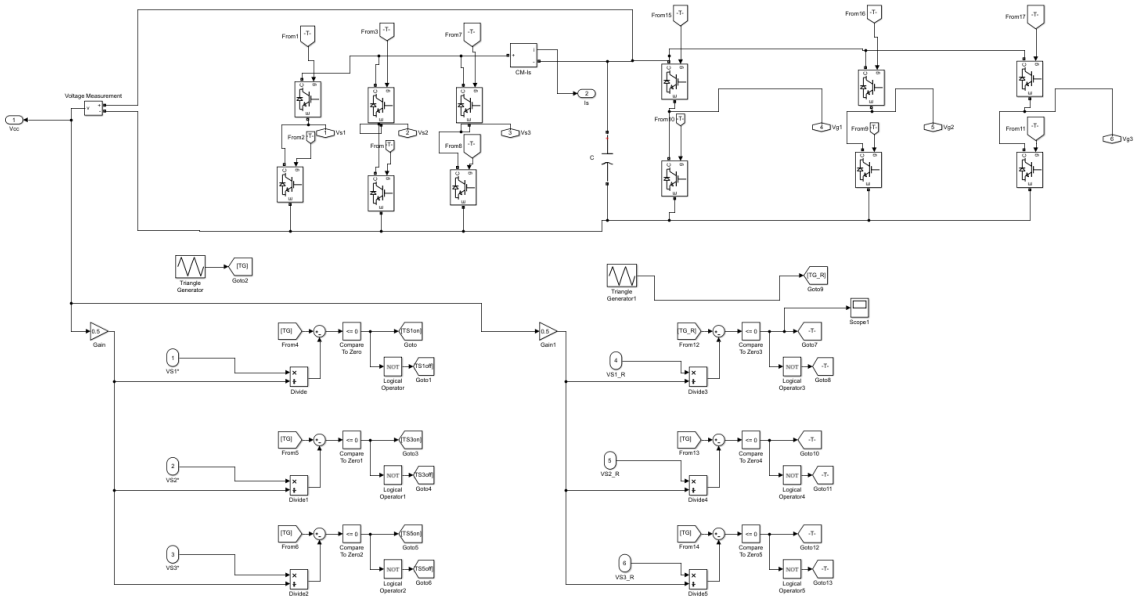

Figure 7.10: Back-to-back converter

The grid-side control diagram is presented in Figure 7.11:

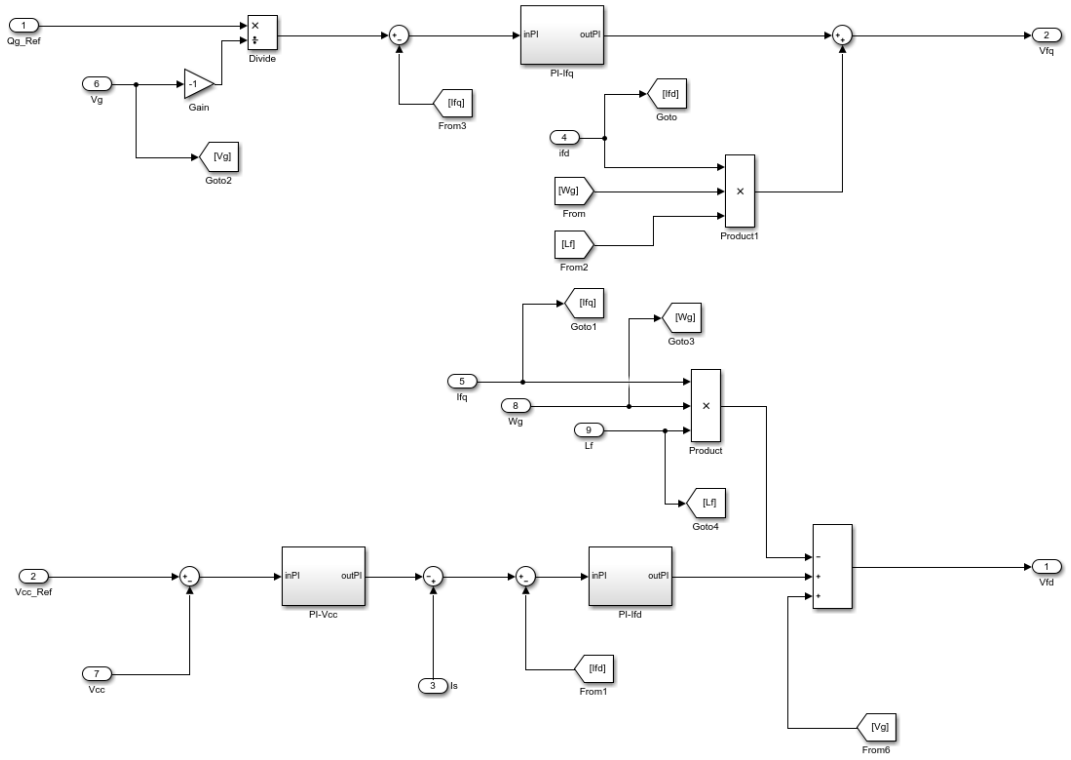

Figure 7.11: Grid-side control

The PLL model is presented in Figure 7.12:

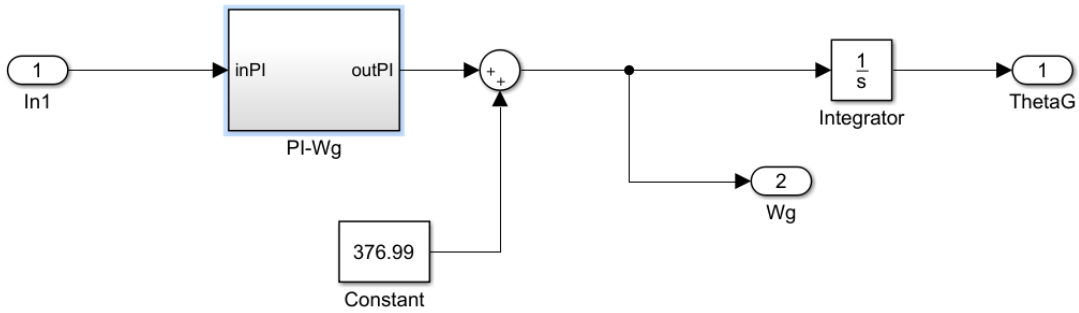

Figure 7.12: PLL model

7.4 SFSC

SFSC is presented in Figure 7.13:

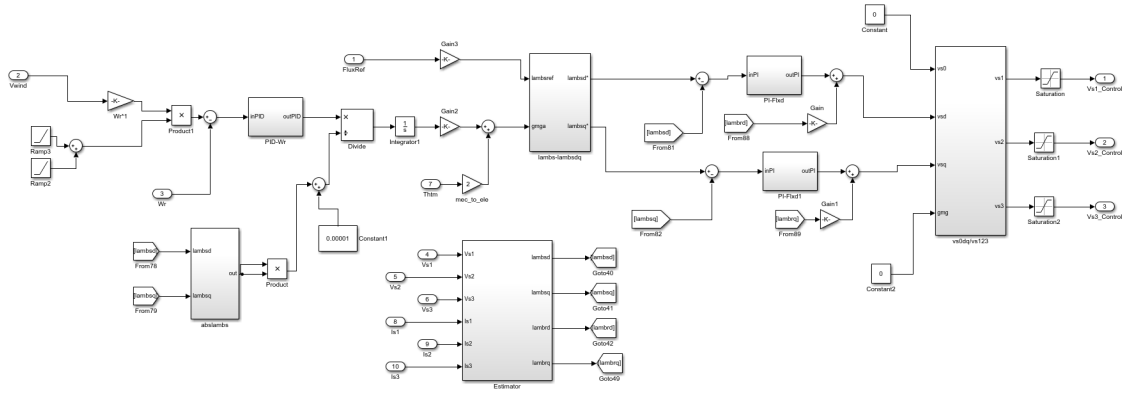

Figure 7.13: SFSC control scheme

7.5 DTC

DTC is presented in Figure 7.14:

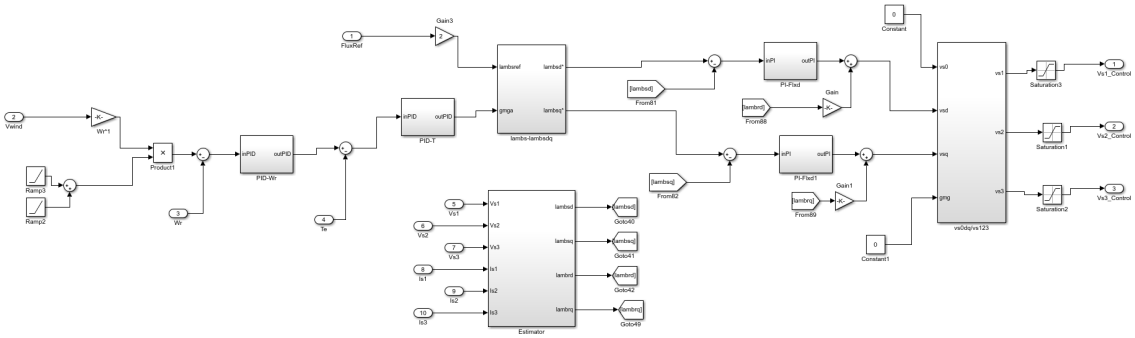

Figure 7.14: DTC control scheme

7.6 RFSC

RFSC is presented in Figure 7.15:

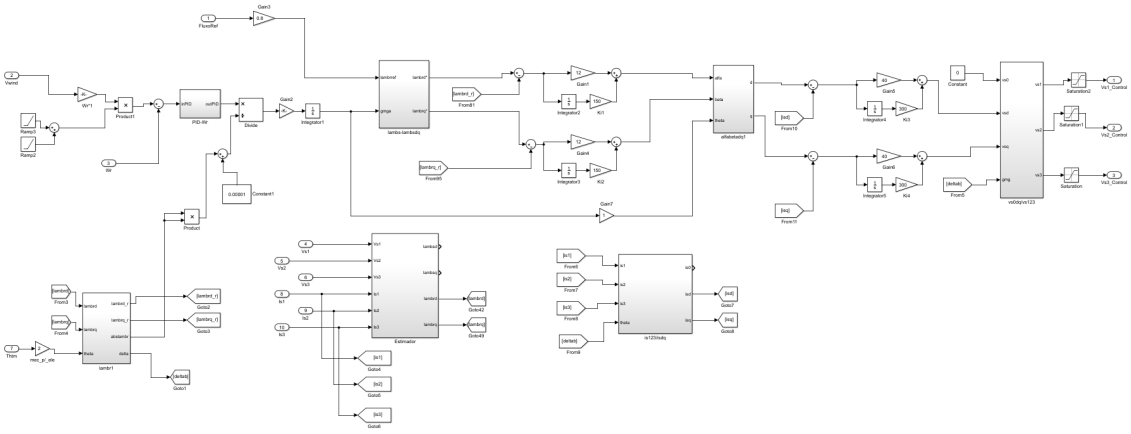

Figure 7.15: RFSC control scheme

7.7 DSFOC

DSFOC is presented in Figure 7.16:

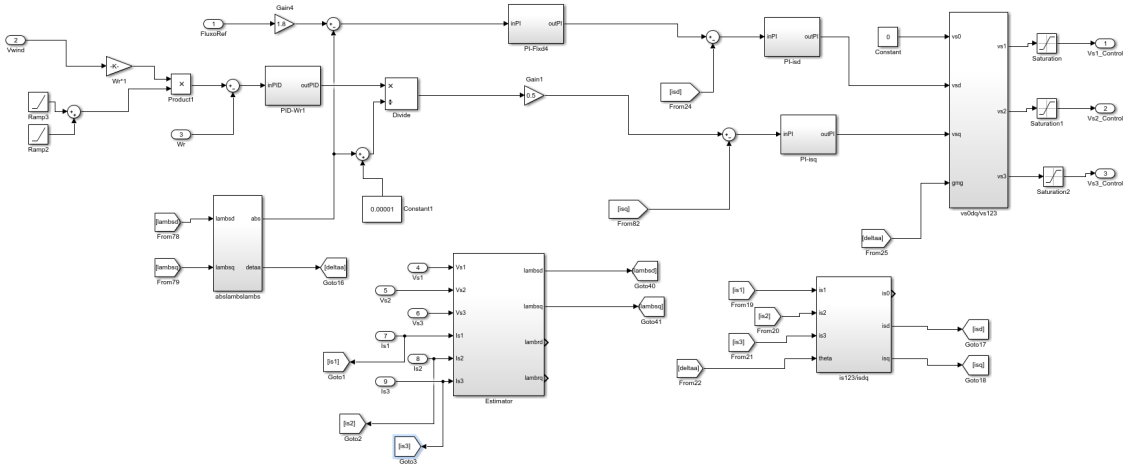

Figure 7.16: DSFOC control scheme

7.8 DRFOC

DRFOC is presented in Figure 7.17:

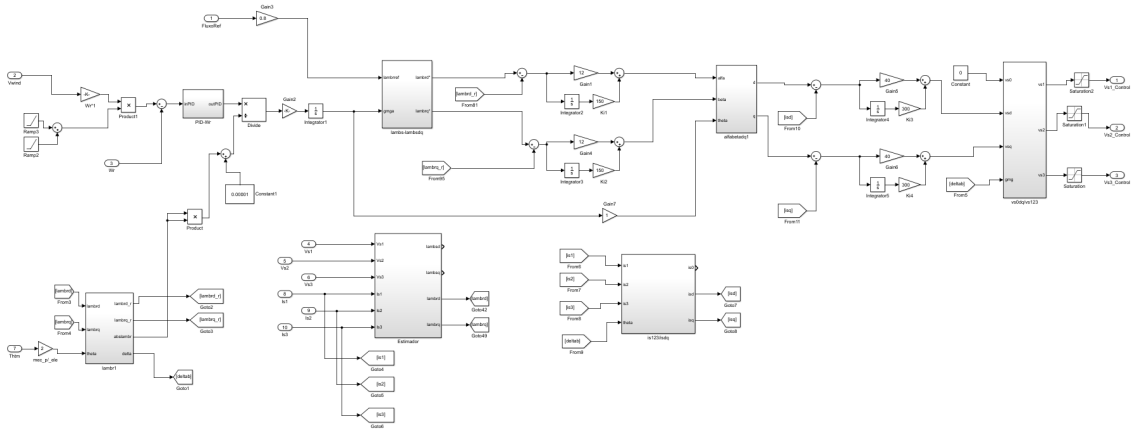

Figure 7.17: DRFOC control scheme

7.9 Three-phase fault

Three-phase fault scheme is presented is presented in Figure 7.18:

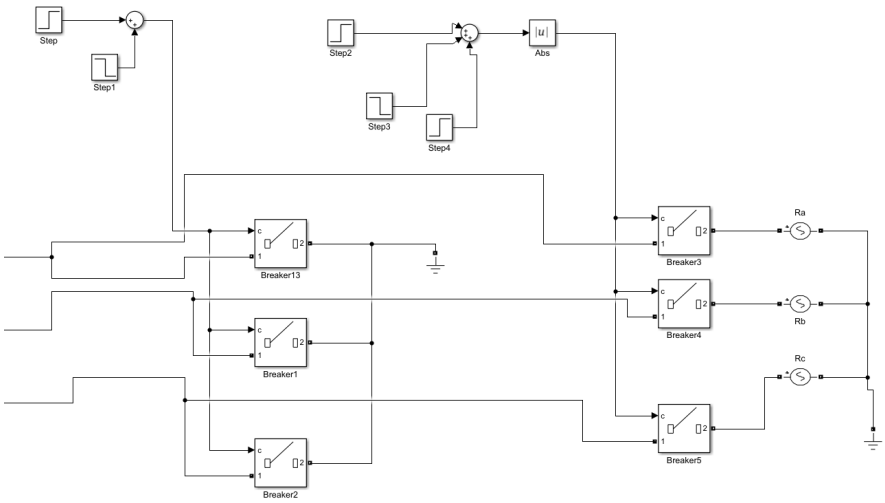

Figure 7.18: Three-phase fault scheme

7.10 Load rejection

Load rejection scheme is presented is presented in Figure 7.19:

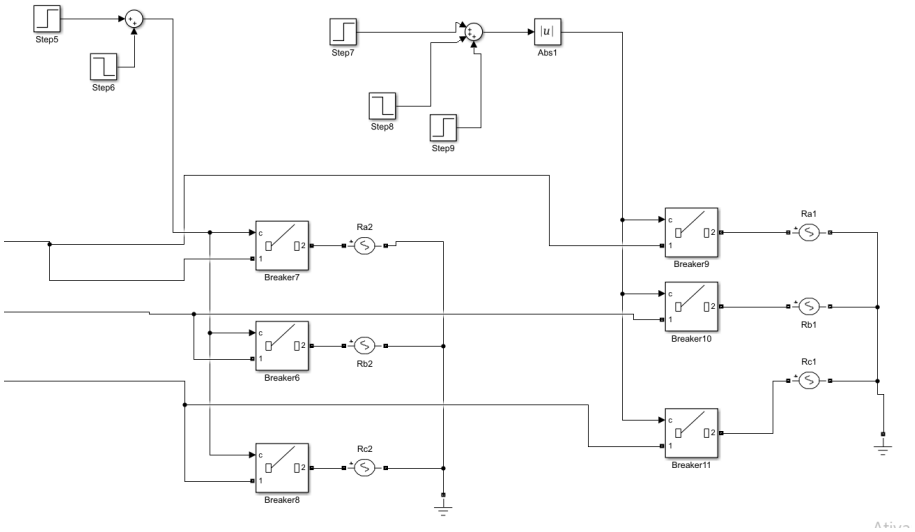

Figure 7.19: Load rejection scheme

Bibliography

Abdel-Rahim, Naser MB & Adel Shaltout (2009), 'An unsymmetrical two-phase induction motor drive with slip-frequency control', *IEEE Transactions on energy conversion* **24**(3), 608–616.

Abdelli, Radia, Djamila Rekioua, Toufik Rekioua & Abdelmounaïm Tounzi (2013), 'Improved direct torque control of an induction generator used in a wind conversion system connected to the grid', *ISA transactions* **52**(4), 525–538.

Alves, A. R. C. (2017), 'Mppt de turbinas eólicas baseadas em scig através do controle por escorregamento com fluxo estatórico'.

Baader, Uwe, Manfred Depenbrock & Georg Gierse (1992), 'Direct self control (dsc) of inverter-fed induction machine: A basis for speed control without speed measurement', *IEEE transactions on industry applications* **28**(3), 581–588.

Barros, L.S. & CMV Barros (2017), 'Modificação no controle do lado da rede de geradores eólicos baseados em pmsg para ampliar a suportabilidade a afundamentos de tensão', *Eletrônica de Potência* **22**(2), 167–178.

Begh, Mirza Abdul Waris & Hans-Georg Herzog (2018), 'Comparison of field oriented control and direct torque control', *Technical University of Munich, Germany* .

Beltran, Brice, Tarek Ahmed-Ali & Mohamed El Hachemi Benbouzid (2008), 'Sliding mode power control of variable-speed wind energy conversion systems', *IEEE Transactions on energy conversion* **23**(2), 551–558.

Bhutto, Darya Khan, Jamshed Ahmed Ansari, Syed Sabir Hussain Bukhari & Faheem Akhtar Chachar (2019), Wind energy conversion systems (wecs) generators: A review, *em* '2019 2nd International Conference on Computing, Mathematics and Engineering Technologies (iCoMET)', IEEE, pp. 1–6.

Blaabjerg, Frede & Ke Ma (2017), 'Wind energy systems', *Proceedings of the IEEE* **105**(11), 2116–2131.

Boulouiha, H. Merabet, A. Allali, M Laouer, A. Tahri, Mouloud Denai & A. Draou (2015), 'Direct torque control of multilevel svpwm inverter in variable speed scig-based wind energy conversion system', *Renewable Energy* **80**, 140–152.

Burton, Tony, David Sharpe, Nick Jenkins & Ervin Bossanyi (2001), *Wind energy handbook*, Vol. 2, Wiley Online Library.

Cheng, Ming & Ying Zhu (2014), 'The state of the art of wind energy conversion systems and technologies: A review', *Energy Conversion and Management* **88**, 332–347.

Dahbi, Abdeldjalil, Mabrouk Hachemi, Nasreddine Nait-Said & Mohamed-Said Nait-Said (2014), 'Realization and control of a wind turbine connected to the grid by using pmsg', *Energy Conversion and Management* **84**, 346–353.

de Rossiter Corrêa, Maurício Beltrão, Cursino Brandão Jacobina, Edison Roberto Cabral Da Silva & Antonio Marcus Nogueira Lima (2004), 'Vector control strategies for single-phase induction motor drive systems', *IEEE Transactions on Industrial Electronics* **51**(5), 1073–1080.

Deloitte (2020).
URL: *https://www2.deloitte.com/br/en.html*

Fernandes, Darlan Alexandria, Fabiano Fragoso Costa & Euzeli Cipriano dos Santos (2013), 'Digital-scalar pwm approaches applied to four-leg voltage-source inverters', *IEEE Transactions on Industrial Electronics* **60**(5), 2022–2030.

Firestone, Jeremy (2019), 'Wind energy: A human challenge', *Science* **366**(6470), 1206–1206.

GWEC (2019).
URL: *https://gwec.net/global-wind-report-2019/*

Haque, Md E., Michael Negnevitsky & Kashem M. Muttaqi (2008), A novel control strategy for a variable speed wind turbine with a permanent magnet synchronous generator, *em* 'Industry Applications Society Annual Meeting, 2008. IAS'08. IEEE', IEEE, pp. 1–8.

IEEE (2014), 'Ieee recommended practices and requirements for harmonic control in electric power systems', *Institue of Electrical and Electronics Engineers* .

Investopedia (2020).
URL: *https://www.investopedia.com/terms/f/feed-in-tariff.asp*

Jacobina, Cursino B & Antônio MN Lima (1996), 'Estratégias de controle para sistemas de acionamento com máquina assíncrona', *Controle & Automação* **7**(1), 15–28.

Kosmodamianskii, AS, VI Vorob'ev & AA Pugachev (2016), 'Scalar control systems for a traction induction motor', *Russian Electrical Engineering* **87**(9), 518–524.

Kulat, Hemant Sahebrao & Anupama Pushkar Huddar (2018), 'Hybrid technique based slip frequency control for the dynamic analysis of im.', *Journal on Electrical Engineering* **11**(4).

Kumar, Rakesh, Kaamran Raahemifar & Alan S Fung (2018), 'A critical review of vertical axis wind turbines for urban applications', *Renewable and Sustainable Energy Reviews* **89**, 281–291.

Kumar, Vinay & Srinivasa Rao (2011), 'Modified direct torque control of three phase induction motor drives with low ripple in flux and torque', *Leonardo Journal of Sciences* **10**(18), 27–44.

Liu, Jing, Htet Lin & Jun Zhang (2019), 'Review on the technical perspectives and commercial viability of vertical axis wind turbines', *Ocean Engineering* **182**, 608–626.

Lunardi, A Santos, JS Solís Chaves & A Joaozinho Sguarezi Filho (2016), 'Predictive direct torque control for a squirrel cage induction generator grid connected for wind energy applications', *IEEE Latin America Transactions* **14**(11), 4454–4461.

Manias, Stefanos N. (2017), 12 - introduction to motor drive systems, *em* S. N.Manias, ed., 'Power Electronics and Motor Drive Systems', Academic Press, pp. 843 – 967.

Matevosyan, Julija, Thomas Ackermann & Sigrid M. Bolik (2005), *Technical Regulations for the Interconnection of Wind Farms to the Power System*, John Wiley Sons, Ltd, capítulo 7, pp. 115–142.
URL: *https://onlinelibrary.wiley.com/doi/abs/10.1002/0470012684.ch7*

Merabet B., H., A. Allali, A. Tahri, A. Draou & Mouloud Denai (2012), 'A simple maximum power point tracking based control strategy applied to a variable speed squirrel cage induction generator', *Journal of Renewable and Sustainable Energy* **4**(5), 053124.

MME (2001).
URL: *http://www.cresesb.cepel.br/index.php?section=atlas$_e$olico*

MME (2019).
URL: *www.mme.gov.br/web/guest/secretarias/planejamento-e-desenvolvimento-energetico/publicacoes/resenha-energetica-brasileira*

Rafaat, Safanah M, Rajaa Hussein et al. (2018), 'Power maximization and control of variable-speed wind turbine system using extremum seeking', *Journal of Power and Energy Engineering* **6**(01), 51.

Rasul, Mohammad G., Abul kalam Azad & Subhash C. Sharma (2017), Clean energy for sustainable development.

Ricardo Cruz, Rui Ventura (2009), 'Integração da energia eólica na rede: Projeto de produção e planejamento de eletricidade'.

Ro, Kyoungsoo & Han-ho Choi (2005), 'Application of neural network controller for maximum power extraction of a grid-connected wind turbine system', *Electrical Engineering* **88**(1), 45–53.

Santos, Cicero (2011), 'Analysis and design of a npc converter for interconnection of energy conversion systems to the grid', *Master's degree dissertation, Federal University of Ceara* .

Shepherd, William & Li Zhang (2017), *Electricity generation using wind power*, World scientific.

Siegfried, Heier (2014), 'Grid integration of wind energy: onshore and offshore conversion systems'.

Simoes, M Godoy, Bimal K Bose & Ronald J Spiegel (1997), 'Fuzzy logic based intelligent control of a variable speed cage machine wind generation system', *IEEE transactions on power electronics* **12**(1), 87–95.

Tawfiq, Kotb B, Arafa S Mansour, Haitham S Ramadan, Mohamed Becherif & EE El-Kholy (2019), 'Wind energy conversion system topologies and converters: Comparative review', *Energy Procedia* **162**, 38–47.

Wang, Quincy & Liuchen Chang (2004), 'An intelligent maximum power extraction algorithm for inverter-based variable speed wind turbine systems', *IEEE Transactions on power electronics* **19**(5), 1242–1249.

Wang, Zhenyu, Wei Tian & Hui Hu (2018), 'A comparative study on the aeromechanic performances of upwind and downwind horizontal-axis wind turbines', *Energy Conversion and Management* **163**, 100–110.

Wu, Bin, Yongqiang Lang, Navid Zargari & Samir Kouro (2011), *Power conversion and control of wind energy systems*, Vol. 76, John Wiley & Sons.

Zebraoui, Otmane & Mostafa Bouzi (2018), Comparative study of different mppt methods for wind energy conversion system, *em* 'IOP Conference Series: Earth and Environmental Science', Vol. 161, IOP Publishing, p. 012023.